Interactions and Geometry in Topological Systems

Ashk Farjami

Department of Physics and Astronomy

University of Leeds

A thesis submitted for the degree of

Doctor of Philosophy

3rd November 2020

Declarations

The work submitted was carried out by the author along with collaborators on jointly-authored publications. The author confirms that appropriate credit has been given within the thesis where reference has been made to the work of others. Chapter 3 is based off work from the publication Meichanetzidis *et al.* (2018), carried out in collaboration with Konstantinos Meichanetzidis, Chris J. Turner, Zlatko Papić and Jiannis K. Pachos. Chapter 4 is based off work from the publication Farjami (2020) carried out alone with guidance from Jiannis K. Pachos. Chapter 6 is based off work from the publication Farjami *et al.* (2020) carried out in collaboration with Matthew D. Horner, Chris N. Self, Zlatko Papić and Jiannis K. Pachos.

To Alice.

Acknowledgements

I would like to start by thanking my PhD supervisor Jiannis Pachos for all his guidance and encouragement. I am lucky to have worked so closely with a man so full of energy and enthusiasm for everything he does. Jiannis has built an amazing research group that I am proud to have been a part of. I am thankful for all of Zlatko's professional advice and challenging questions. I also thank Alex for showing me what's what and what's not with knots and whatnot. He was patient with all my questions and ensured the whiteboards in the office always looked impressive. My thanks to Konstantinos for guiding me through my first project, teaching me some important Greek and for always keeping it real (less of a mouthful Kon). I appreciate Chris Self sharing his expertise on the Kitaev model, being one of the most chill guys I've ever met and always trying his best at Mario kart. I thank Matthew for discussing squares, circles, triangles and every other shape with me and for such being a pleasure to work with. I also have to thank Matthew and Jake for all the thought provoking debates on Westerosi politics. I thank Chris Turner for introducing me to a small fortified city in the south of France and putting up with some dodgy business in Fangorn. I am eternally grateful to him for taking the time to share his knowledge on just about everything. Most importantly though, I am glad to have met someone with such passion for what they do, he inspired me to work harder. I then need to thank KP and Furtak for being there when I had worked a little too hard.

I could not have completed this PhD without the support of my friends and family. To name a few, thank you mum for always supporting me and questioning my every decision. Thank you dad for pushing

me and offering to double check my maths. Thank you Sinéad for the company, the games and a place to sleep. Thank you Freddy and Amelia for making me smile. Finally, thank you Alice for being my best friend through every moment. You have always been there for me and I will always be there for you.

I love you all.

Abstract

Topological materials are one of the lead candidates for developing viable noise resilient quantum computers. The properties that make these materials so suited to the task include their degenerate ground states and anyonic excitation statistics. However, it is often the case that the more exotic the statistics are the more complex the underlying Hamiltonian is. This can make them challenging to work with. Alternate representations of these Hamiltonians can prove useful in solving the systems and investigating the behaviour of their physical observables.

This thesis explores the construction and advantages of alternate representations of certain topological quantum systems. Initially, unitary transformations are presented, which map the $\mathbb{Z}_2$ surface code and toric code to free fermions and fermions coupled to global symmetry operators, respectively. The methods presented in this thesis could be employed to find possible free fermion solvable descriptions of other more complex interacting topological systems. It also is found that the Kitaev honeycomb model has an effective geometric description in terms of massless Majorana spinors obeying the Dirac equation embedded in a Riemann-Cartan spacetime. This description is shown numerically to be faithful for the low energy limit of the model, predicting the response of two-point correlations to variations of the coupling parameters of the model. These results suggest that geometric descriptions of topological materials could provide useful insights into the behaviour of their physical observables that make them so useful for quantum computation.

Contents

List of Figures

Chapter 1

Introduction

What do quantum computers and kids these days have in common? They are both too sensitive. The quantum computers of today have been dubbed *Noisy Intermediate Scale Quantum (NISQ)* computers Preskill (2018). This is due to their size and susceptibility to external noise, which can destroy the delicate superpositions essential for quantum computation. This noise could be due to imperfect interactions with the system, such as when performing operations or reading data. Alternatively, it could be an inability to protect the qubits from temperature fluctuations or other forms of radiation. Despite these issues Google recently unveiled Sycamore, a 54-qubit quantum processor. This has since proved to be sufficient to realise quantum supremacy Arute *et al.* (2019), a significant achievement in the development of useful quantum devices. However, many of the accomplishments of the last decade have been down to advancements in engineering. We are now able to control qubits and isolate them from external noise more effectively. They are still the same inherently sensitive qubits though.

Topologically ordered materials are being studied as possible candidates for a fundamentally different approach to quantum computing. These materials could be used as quantum memories, providing topological protection to information encoded in logical qubits Dennis *et al.* (2002). The exotic anyonic statistics of their excitations can be used to encode the quantum logic gates necessary for quantum computation. In fact some non-Abelian anyons, such as Fibonacci anyons, have been found to be universal for quantum computation Mong *et al.* (2014). The

exchange statistics of such anyons are sufficient to encode any possible unitary operation on the logical qubits of the system Nielsen & Chuang (2011).

Due to the complexity of topologically ordered materials it is often unclear from the defining Hamiltonian what their properties are and whether their dynamics is even solvable. Finding alternative representations of these systems can provide useful insight into the solvability and allow one to make predictions about the physical observables of the model. This thesis explores construction and advantages of alternate representations of topologically ordered systems. The first half (Chapters 2, 3 and 4) examines models with possible free fermion representations. This could help produce exact solutions of the models. The second half (Chapters 5 and 6) considers effective descriptions of the continuum limit of topologically ordered systems. These descriptions are useful for predicting the behaviour of physical observables of the models in the low energy limit.

Chapters 2, 3 and 4

A striking feature of topological many-body systems is their ability to exhibit collective phenomena without analogue in their constituent particles. Many investigations into exotic statistical behaviours focus on topologically ordered systems Wen (1990) that support anyons Leinaas & Myrheim (1977); Wilczek (1982). Although some properties associated to topological phases of matter can occur in systems of free fermions, their emergence is generally associated with interactions between particles. One of the difficulties of working with such systems however is that interactions between particles can make them extremely complex and hard to solve. Systems, such as the spin liquids Anderson (1987) and the fractional quantum Hall states Tsui *et al.* (1982), exemplify the effects of interactions in many-electron systems. On the other hand, there are systems which can be modelled by free fermions, making them exactly solvable, that exhibit many of the unique properties of topological phases of matter that make them so interesting. For example, Kitaev's honeycomb model Kitaev (2006) supports ground state degeneracies and exotic topological excitations in the form of Majorana zero modes Ivanov (2001); Read & Green (2000).

Identifying models with free fermion representations will allow us to better understand the emergence of properties such as anyonic excitations and degenerate ground states in these complex topological systems. Chapter 3 uses the measure of interaction distance $D_{\mathcal{F}}$ Turner *et al.* (2017) to study the role of interactions in topological states of matter in $(2+1)-$dimensional string-nets Levin & Wen (2005) and $3+1-$dimensional Walker-Wang models Walker & Wang (2012). This work was published as part of Meichanetzidis *et al.* (2018). Interestingly, all of the states studied supporting non-Abelian anyons are found to be interacting, suggesting interactions are necessary for the emergence of non-Abelian excitation statistics in these fixed point stabilizer Hamiltonians. This contrasts with the Kitaev honeycomb model, which supports Ising anyons and has a representation in terms of free fermions coupled to a $\mathbb{Z}_2$ gauge field. States with free fermion representations are also identified, including the states of the toric code Browne (2014); Kitaev (2003); Resende (2017) and its open boundary version, the $\mathbb{Z}_2$ surface code Bombin & Martin-Delgado (2007); Bravyi *et al.* (2017). These models have been the test-bed for numerous investigations of condensed matter phenomena as well as quantum information applications Brown *et al.* (2016); Fowler *et al.* (2012); Kitaev & Laumann (2009). The main reason for the popularity of the toric code is that it is an exactly solvable model that has eigenstates with non-trivial topological entanglement entropy Hamma *et al.* (2013), able to support Abelian anyons, exotic quasiparticles that can fault-tolerantly encode and manipulate quantum information. An important feature of this topological model is that it is relatively simple, with the anyonic statistics and fusion rules emerging directly from the algebraic properties of Pauli matrices. At the same time the toric code enjoys many applications. It can be used as a fault tolerant quantum memory protecting against spurious local perturbations Wootton & Pachos (2011), it can perform topological quantum computation resilient against control errors Kitaev (2003), or it can encode more complex anyonic models such as Majorana fermions at lattice defects Brown *et al.* (2017); Wootton (2017).

The toric code has been experimentally simulated with highly entangled four-photon GHZ states Pachos *et al.* (2009) and the four-body interaction has been physically realised with Josephson junctions Gladchenko *et al.* (2009); Terhal *et al.* (2012). However, it has been argued that the Hilbert space of the toric

code, in the presence of an external magnetic field contains a low energy subspace that can be described effectively by hopping fermionic excitations coupled to a $\mathbb{Z}_2$ gauge field Levin & Wen (2003). This gauge field does not introduce interactions, but encodes the exotic statistics of the excitations.

Chapter 4 presents local unitary transformations from the $\mathbb{Z}_2$ surface and toric code to a free fermion system and a system of free fermions coupled to an interacting parity operator, respectively. It also explores how the anyonic statistics of the models are encoded in the free fermion modes. This work was published in Farjami (2020). Previous works studying transformations of the toric code include the paper Brown *et al.* (2011), where the authors provide a duality mapping from a cluster state on an $N \times N$ lattice to the toric code on an $N \times (N-1)$ lattice. The cluster state can be mapped to individual spin Hamiltonians, which are equivalent to free fermions. The mapping to the toric code takes some of the cluster state's boundary terms to stabilizers of non-contractible loops in the toric code, thus removing the degeneracy of the ground state. In addition, the paper Nussinov & Ortiz (2009) maps the toric code onto decoupled Ising chains, and the papers Jamadagni *et al.* (2018); Tagliacozzo & Vidal (2011) give duality mappings, built from CNOT gates, from the toric and surface code in the presence of external magnetic fields to Ising models.

Chapter 2 provides background on general anyon models, lattice models, and interactions in quantum many-body systems used in the study of interaction distance and alternative representations of the surface and toric code in Chapters 3 and 4.

Chapters 5 and 6

The Kitaev model is an important model of topological superconductors. It has been the focus of much research since its introduction by Kitaev in Kitaev (2006). It is a model of spin-1/2 particles on a two dimensional honeycomb lattice. The Kitaev honeycomb model is both topologically ordered in the sense that it can support anyonic excitations and it is a topological phase with a non-trivial Chern number Kitaev (2006). Kitaev demonstrated that the model is exactly solvable

as it has a representation in terms of free fermions, which provides the opportunity to analytically probe its anyonic properties Lahtinen *et al.* (2008), its topological edge currents Self *et al.* (2017), and to investigate its finite temperature behaviour Lahtinen & Pachos (2010); Lahtinen *et al.* (2012); Nasu & Motome (2015); Nasu *et al.* (2014, 2015); Self *et al.* (2019). Moreover, many features of the Kitaev honeycomb model are recognised in experimentally realisable materials, such as complex iridium oxides Chaloupka *et al.* (2010); Choi *et al.* (2012); Jackeli & Khaliullin (2009) or ruthenium chloride Banerjee *et al.* (2016). This makes the KHLM of interest to numerous theoretical and experimental investigations.

The first part of Chapter 5 focuses on the Kitaev honeycomb model discussing many of its interesting properties such as its free fermion representation, the anyonic excitations Ivanov (2001); Read & Green (2000) and phase diagram Kitaev (2006). It also studies the continuum limit, or low energy limit, of the isotropic, homogeneous version of the model, which is equivalent to a Dirac equation embedded in a flat $(2+1)-$dimensional Minkowski spacetime.

It is known that topological superconductors can have an effective interpretation in terms of curved geometry. For example, it has been shown in Golan & Stern (2018) that the continuum limit of a spinless p-wave superconductor on a square lattice minimally coupled to an electromagnetic field, takes the form of a Dirac Hamiltonian defined on a Riemann-Cartan spacetime Carroll (2003); Hehl & Datta (1971); Nakahara (2003). Riemann-Cartan geometry also arises in the theory of defects in lattices, where disclinations and dislocations in the continuum limit are described by curvature and torsion, respectively de Juan *et al.* (2010); Katanaev & Volovich (1992). This has been investigated in strained graphene de Juan *et al.* (2010, 2013); Wagner *et al.* (2019). On the other hand, the fractional quantum Hall (FQH) states have been shown to exhibit a universal response to variations of lattice geometry, leading to many fruitful investigations of an interplay between the topology and ambient geometry of these strongly-correlated systems Abanov & Gromov (2014); Avron *et al.* (1995); Bradlyn & Read (2015); Can *et al.* (2014); Gromov & Abanov (2014); Gromov & Son (2017); Gromov *et al.* (2015); Haldane (2009, 2011); Hughes *et al.* (2011); Klevtsov & Wiegmann (2015); Read (2009); Wen & Zee (1992); Wiegmann (2018).

Nevertheless, it is not known how accurately Riemann-Cartan geometry can describe the behaviour of actual microscopic, solvable lattice models. Chapter 6 studies the continuum limit of the Kitaev honeycomb model in a variety of coupling regimes deriving a geometric description of the model in terms of Majorana spinors obeying the Dirac equation embedded in a non-trivial Riemann-Cartan spacetime with curvature and torsion. It is important to note that this geometry emerges purely from distortions in the couplings of the system and *not* from the geometry of the lattice itself, as with many of the FQH studies above. This Riemann-Cartan picture has an associated metric describing a distortion of space proportional to the coupling parameters of the model. The Kitaev model is exactly solvable, which provides the opportunity to numerically verify this metric by studying the behaviour of two-point Majorana quantum correlations in different coupling regimes. This work was published in Farjami *et al.* (2020).

The second part of Chapter 5 provides necessary background for Chapter 6, detailing the components of $(2+1)-$dimensional Riemann-Cartan geometry Carroll (2003); Nakahara (2003) including the dreibein and spin connection defining non-trivial metric, curvature and torsion.

Chapter 7

Chapter 7 reviews the results presented in Chapters 3, 4 and 6. Potential avenues of future investigations are discussed.

Chapter 2

Background 1: Anyons, Lattices and Interactions

This chapter provides background on lattice models with anyonic excitations and interactions in many-body systems. It starts by introducing the theory of anyons in Section 2.1. Fusion and braiding operations are defined, which encode the exotic statistics of these particles that make them useful for quantum computation. The $\mathbb{Z}_2$ surface code and toric code are presented in Section 2.2 as specific examples of lattice models supporting anyonic excitations. The statistics of these excitations are explored along with an interpretation of the surface code and toric code as stabilizer codes or quantum memories. It is discussed how quantum information can be encoded and protected in these codes. This provides the background for Chapter 4, which explores free fermion representations of these codes. Section 2.3 then gives a overview of the general formulation of string-nets and Walker-Wang models. These models are built from the fusion and braiding operations introduced in Section 2.1. The form of the reduced density matrix of string-net and Walker-Wang states is also presented. Finally, Section 2.4 discusses interactions in quantum many-body systems. The properties of the energy and entanglement spectrum of free fermion systems are described and used in order to define the interaction distance Turner *et al.* (2017). This provides the necessary background for Chapter 3, which uses the interaction distance to identify string-nets and Walker-Wang models with effective descriptions in terms of free fermions.

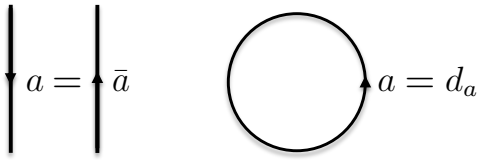

Figure 2.1: (Left) A diagrammatic representation of anyons in terms of oriented strings of given charge. (Right) The quantum dimension d_a is represented by a loop of charge a, which is equivalent to the creation of a pair a and $\bar{a}$ from the vacuum and fusion back to the vacuum.

2.1 Anyon models

Anyons are emergent quasiparticles of $(2+1)-$dimensional topological systems. They have a variety of interesting properties such as spins that can take on any value Bonderson (2007). These properties lead to exotic braiding and fusion statistics, discussed in this section, which make anyonic systems an excellent candidate for quantum computing. Anyons created in a particular fusion state are manipulated through fusion and braiding operations, which act as quantum gates Fan & de Garis (2010). Braiding of anyonic charges in non-Abelian models can lead to non-trivial evolutions of fusion states. For certain non-Abelian anyon models these operations are sufficient for universal quantum computation Mong *et al.* (2014). Quantum computation based on anyon models also have a degree of topological protection. Braiding operations do not depend on the specific path taken, so small deformations to the path have no effect on the encoded quantum information.

This section is broken down as follows. Section 2.1.1 presents the fusion rules of anyon models in terms of F-moves and defines the fusion and splitting states of sets of anyons. Section 2.1.2 discusses the braiding of anyons in terms of R-moves.

A useful diagrammatic representation of anyons in terms of oriented strings of given charge is introduced and employed throughout this section.

2.1.1 Fusion

An anyon model has a finite set of anyons or anyonic charges $\mathcal{C} = \{0, a, b, c, ...\}$ given by the irreducible representations of a group G Bonderson (2007); Pachos (2012). It is useful to employ a diagrammatic representation of these anyon models. Each anyonic charge in $\mathcal{C}$ corresponds to a string with a given orientation, shown in Fig. 2.1 (Left). These can be considered as worldlines in 2+1 dimensions with time pointing downwards. Fusion of a pair of anyons equates to bringing two anyons together and observing their collective behaviour. The anyons in $\mathcal{C}$ obey a commutative, associative fusion algebra defined by the group operation of G,

$$a \times b = \sum_c N_{ab}^c c, \tag{2.1}$$

where N_{ab}^c is the fusion multiplicity, denoting how many distinct ways a and b fuse to give c. Thus, fusion multiplicities are non-negative integers. Abelian anyons have unique fusion outcomes, implying $\sum_c N_{ab}^c = 1$ if a or b is Abelian. If there exists some $a, b, c \in \mathcal{C}$ such that

$$\sum_c N_{ab}^c > 1 \tag{2.2}$$

then the set $\mathcal{C}$ and the fusion algebra (2.1) describe a non-Abelian anyon model. In each anyon model there exists a single vacuum charge $0 \in \mathcal{C}$ which fuses trivially with all other anyons, $N_{a0}^b = \delta_{ab}$. The vacuum charge is often represented by an empty string. Each anyon $a \in \mathcal{C}$ also has a unique antiparticle pair $\bar{a} \in \mathcal{C}$ with which it fuses to the vacuum, $N_{ab}^0 = \delta_{b\bar{a}}$. The a and $\bar{a}$ anyonic strings are related by a flipping of orientation, as shown in Fig. 2.1 (Left).

Products of anyons have fusion and splitting Hilbert spaces. States in the Hilbert space correspond to specific fusion and splitting processes. For example, take the product $a \times b = \sum_c N_{ab}^c c$. Each possible fusion channel corresponds to a state

$$|a, b; c, \mu\rangle \in \mathcal{H}_{ab}^c, \quad \langle a, b; c, \mu| \in \mathcal{H}_c^{ab} \tag{2.3}$$

where $\mu = 1, ..., N_{ab}^c$ labels the way in which a fusion or splitting outcome is achieved, while $\mathcal{H}_{ab}^c$ and $\mathcal{H}_c^{ab}$ are the fusion and splitting Hilbert spaces, respectively. The fusion or splitting states are represented by the trivalent vertices

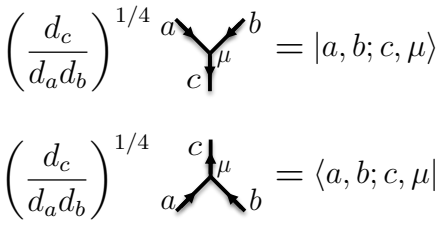

Figure 2.2: A diagramatic representation of the fusion (Top) and spliting (Bottom) states (2.3). Included are normalisation factors in terms of the quantum dimension d_a, defined in (2.9).

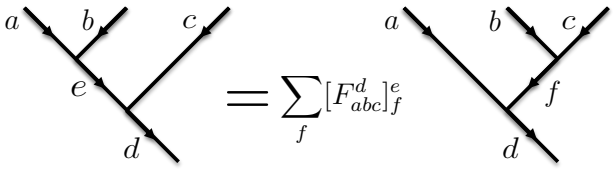

Figure 2.3: A diagramatic representation of the F-moves (2.6).

of anyon strings shown in Fig. 2.2, where the quantum dimension d_a are taken to be normalisation factors and are discussed later in this section. The states (2.3) form an orthonormal basis for the fusion and splitting spaces. Additionally, states corresponding to different fusion outcomes are orthogonal to one another, $\langle a, b; c, \mu | a, b; d, \nu \rangle = \delta_{cd}\delta_{\mu\nu}$. This ensures that a pair of anyons a and b created from c via the mechanism μ must also fuse to c via μ, unless some non-trivial operation is applied, such as a braiding, discussed in 2.1.2. These spaces have $\dim(\mathcal{H}^c_{ab}) = \dim(\mathcal{H}^{ab}_c) = N^c_{ab}$. [1]

Consider now the fusion space $\mathcal{H}^{abc}_d$ of three anyons a, b and c fusing to d. This can be broken down into the fusion of a and b to e and the subsequent fusion of e and c to d. The space $\mathcal{H}^{abc}_d$ is isomorphic to the following composition of fusion spaces

$$\mathcal{H}^d_{abc} \cong \bigoplus_e \mathcal{H}^e_{ab} \otimes \mathcal{H}^d_{ec}, \tag{2.4}$$

[1] All Abelian and non-Abelian anyon models considered in this thesis have $N^c_{ab} \leq 1$ for all combinations of a, b and c so the multiplicity label μ is dropped from here on.

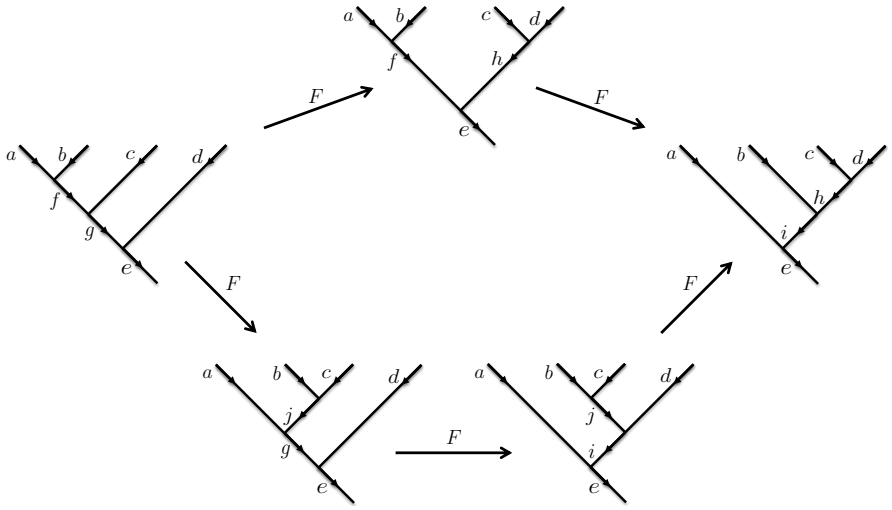

Figure 2.4: A diagramatic representation of the Pentagon equation (2.8).

where the direct sum runs over all possible anyons e from the fusion of a and b. This space has $\dim(\mathcal{H}_d^{abc}) = \sum_e N_{ab}^e N_{ec}^d$ and an orthonormal basis of states defined by

$$|a, b; e\rangle \, |e, c; d\rangle \, , \tag{2.5}$$

where the tensor product symbol is missed out. However, the order in which anyons are fused could be rearranged. Each ordering corresponds to a different basis of states. One may map between these basis with isomorphisms called F-moves defined as

$$|a, b; e\rangle \, |e, c; d\rangle = \sum_f [F_{abc}^d]_f^e \, |b, c; f\rangle \, |a, f; d\rangle \, . \tag{2.6}$$

These are unitary matrices. A diagrammatic representation of these moves is given in Fig. 2.3.

This process of breaking down fusion and splitting spaces generalises to larger products of anyons. The fusion space $\mathcal{H}_{a_1 \ldots a_n}^{b_{n-1}}$ has

$$\dim(\mathcal{H}_{a_1 \ldots a_n}^{b_{n-1}}) = \sum_{b_1 \ldots b_{n-2}} N_{a_1 a_2}^{b_1} \ldots N_{b_{n-2} a_n}^{b_{n-1}}, \tag{2.7}$$

where the sum runs over all in between fusion outcomes possible given the fusion ordering. It is possible to map from any set of basis states in this space to any

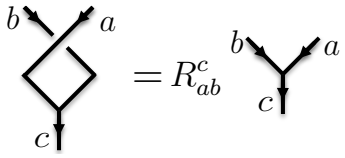

Figure 2.5: A diagramatic representation of the R-moves (2.11).

other with some composition of F-moves. Any two sequences of F-moves which both map between the same specific fusion orderings must be equivalent. As a result the F-moves must satisfy the consistency equation called the Pentagon equation

$$[F^e_{fcd}]^g_h [F^e_{abh}]^f_i = \sum_j [F^g_{abc}]^f_j [F^e_{ajd}]^g_i [F^i_{bcd}]^j_h. \tag{2.8}$$

This equivalence is demonstrated in Fig. 2.4.

An important quantity in anyon models is the quantum dimension d_a of each anyon a. It is a measure of how fast the dimension of the fusion or splitting Hilbert space grows as anyons are added to the system. For a large number, n, of a anyons the dimension of the Hilbert space is $\dim(\sum_b \mathcal{H}^{b_{n-1}}_{a\ldots a}) \sim d_a^n$. These quantum dimensions satisfy relations defined by the fusion rules, i.e. if (2.1) holds then

$$d_a d_b = \sum_c N^c_{ab} d_c. \tag{2.9}$$

The quantum dimension d_a has a diagrammatic representation equivalent to the creation of a pair a and $\bar{a}$ from the vacuum and fusion back to the vacuum as shown in Fig. 2.1 (Right). This agrees with the normalisation factors in Fig. 2.2.

The total quantum dimension of the system is defined as

$$\mathcal{D} = \sqrt{\sum_a d_a^2}. \tag{2.10}$$

2.1.2 Exchange and Braiding

A pair of anyons a and b are exchanged by the unitary braid operation R_{ab}. These operators are called R-moves. They act on the fusion states as

$$R_{ab} |a, b; c\rangle = R^c_{ab} |b, a; c\rangle \tag{2.11}$$

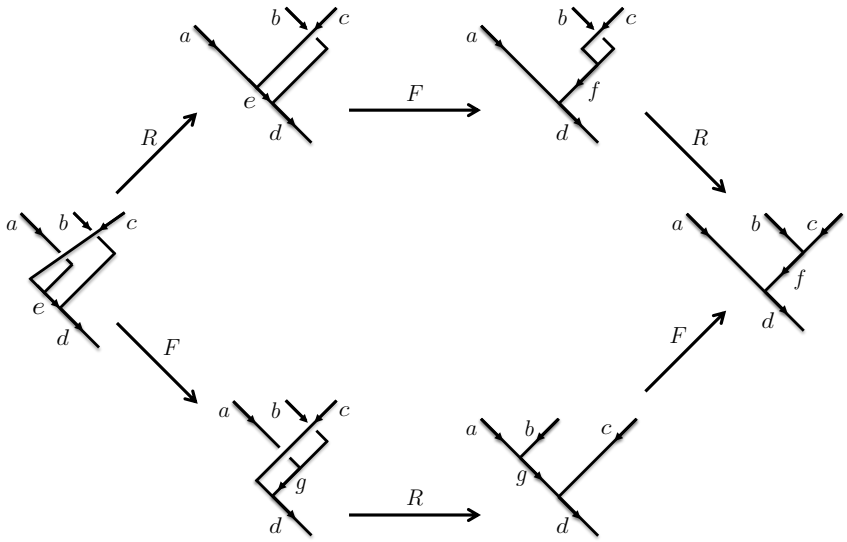

Figure 2.6: A diagramatic representation of the Hexagon equation (2.13).

where R^c_{ab} defines the action of R_{ab} on a particular fusion state. A diagrammatic representation of (2.11) is given in Fig. 2.5.

The exchange R^c_{ab} is equivalent to rotating a and b anticlockwise and c clockwise by π Pachos (2012). The clockwise rotation of a spin s particle by ϕ produces the phase $e^{-i\phi s}$. Therefore,

$$R^c_{ab} = e^{i\pi s_a} e^{i\pi s_b} e^{-i\pi s_c}, \tag{2.12}$$

where s_a, s_b and s_c are the spin of a, b and c, respectively. Thus, the exchange of a particle with its antiparticle pair is equivalent to one full anticlockwise rotation, $R^0_{a\bar{a}} = e^{i2\pi s_a}$, and exchange with the vacuum charge is trivial, $R^a_{a0} = 1$.

Similar to the pentagon equation for F-moves alone, the F-moves and $R-$moves together must satisfy the Hexagon consistency equation

$$R^e_{ac}[F^d_{acb}]^e_f R^f_{bc} = \sum_g [F^d_{cab}]^e_g R^d_{gc} [F^d_{abc}]^g_f. \tag{2.13}$$

This ensures that any two sequences of F-moves and R-moves which both map between the same specific string configurations are equivalent. This equivalence is demonstrated in Fig. 2.6.

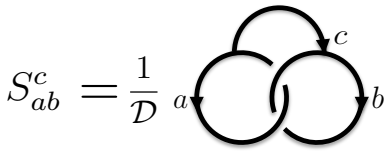

Figure 2.7: A diagramatic representation of the S-tensor (2.14).

Another important quantity is the S-tensor. The elements of which are defined in Bullivant & Pachos (2016) as

$$S^c_{ab} = \frac{1}{\mathcal{D}} \sum_e N^e_{ab} [F^b_{aab}]^c_e R^e_{ab} R^e_{ba} \sqrt{d_a d_b d_e} \tag{2.14}$$

A diagrammatic representation of this tensor is shown in Fig. 2.7. A non-zero element S^c_{ab} implies that braiding two charges a and b can map non-trivially between fusion states $|a, \bar{a}; 0\rangle |0, b; \bar{b}\rangle$ and $|a, \bar{a}; c\rangle |c, b; \bar{b}\rangle$.

Anyons can be used to perform quantum computation. Quantum information is encoded in the fusion states of the anyons and braiding operations act as quantum gates mapping between fusion states. As all Abelian anyons have unique fusion outcomes braiding cannot change their fusion states. Therefore, $S^{c\neq 0}_{ab} = 0$ for any Abelian anyons a, b and c. This implies Abelian anyons are not sufficient for universal quantum computation, as braiding Abelian anyons produces only phases. Non-Abelian anyon models such as Fibonacci anyons are able to achieve universal quantum computation Mong *et al.* (2014).

2.2 The Surface and Toric Code

This section presents a brief review of the $\mathbb{Z}_2$ surface Bombin & Martin-Delgado (2007); Bravyi *et al.* (2017) and toric code Browne (2014); Kitaev (2003); Resende (2017). These are equivalent models in the bulk with distinct boundary conditions. This provides necessary background for work presented in Chapters 3 and 4. Section 2.2.1 presents the Hamiltonian of the model, introducing the vertex and plaquette operators. Section 2.2.2 shows that the excitations of the model are Abelian anyons by studying their fusion and exchange statistics. Finally, Section 2.2.3 discusses the interpretation of the toric code as a quantum error correcting

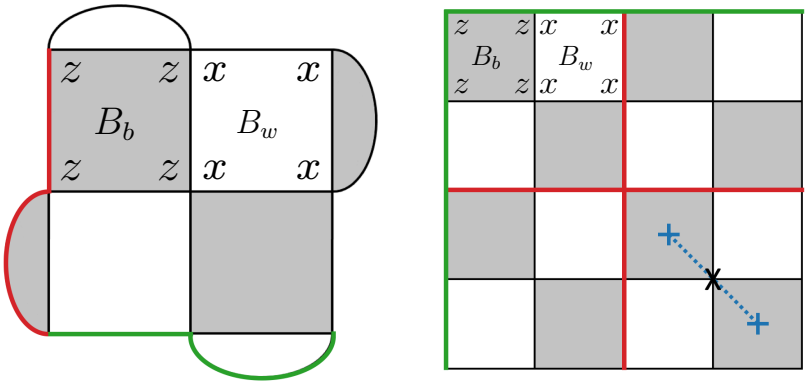

Figure 2.8: (Left) The 3×3 surface code, with physical qubits located at the vertices of the lattice. Plaquette stabilizers B_b and B_w are on black b and white w plaquettes respectively. B_b (B_w) applies a σ^z (σ^x) operator to each qubit surrounding b (w) and detects the parity of σ^x (σ^z) operators on these qubits. Logical Pauli operators S_x and S_z are shown as the red and green lines, respectively, encoding one logical qubit. (Right) The 4×4 toric code, with physical qubits at the vertices of the lattice. Plaquette stabilizers, B_b and B_w, are of the same form as those in the surface code. The choices of X and Z logical operators are shown in red and green, respectively, with S_{x_1} and S_{z_2} depicted as the horizontal lines and S_{z_1} and S_{x_2} as the vertical lines. These encode the two logical qubits of the toric code. A σ^x operator acting on a single qubit producing a string with an m anyon on the plaquettes at each end is shown in blue.

stabilizer code suitable for use as a quantum memory. This model has been the focus of much research and there are a variety of comprehensive reviews available such as Kitaev (2003) and Browne (2014).

2.2.1 The Hamiltonian

The surface and toric codes are models of qubits or spin-1/2 particles on the vertices of an $L \times L$ square lattice. The surface code has open boundary conditions and the toric code has periodic boundary conditions, i.e. defined on the surface of a torus. The lattice length L is always odd for the surface code and even for

the toric code. The Hamiltonians of both models are given by

$$H = -\sum_b B_b - \sum_w B_w, \tag{2.15}$$

defined in terms of black B_b and white B_w plaquette operators arranged in an alternating checker pattern, as shown in Fig. 2.8. These are given by

$$B_b = \prod_{i \in b} \sigma_i^z \tag{2.16}$$

and

$$B_w = \prod_{i \in w} \sigma_i^x, \tag{2.17}$$

where σ^x and σ^z are Pauli operators. The products run over all spins i surrounding the black plaquette b and white plaquette w, respectively. The surface code has some semi circular plaquettes on the boundary of the model, as shown in Fig. 2.8 (Left). Operators corresponding to the semicircle plaquettes on the boundary and square plaquettes in the bulk have support on two and four qubits, respectively.

It is easy to see that black (2.16) and white (2.17) operators commute with each other and the Hamiltonian (2.15). Any black operator trivially commutes with all other black operators as they are built of σ^z operators, which commute. The same is true of white operators, built from σ^x operators. Although σ^x and σ^z operators acting on the same spin anti-commute with each other, any black operator shares an even number of spins with any white operator, two if they are neighbouring and zero if they are not. Therefore, they will always commute as $[\sigma_i^x \sigma_j^x, \sigma_i^z \sigma_j^z] = 0$.

The operators B_b and B_w square to the identity, so they have eigenvalues ± 1. Hence, for each ground state $|\psi_g\rangle$ of the model $B_b |\psi_g\rangle = B_w |\psi_g\rangle = |\psi_g\rangle$ for all b and w. One such state is

$$|\psi_{g_1}\rangle = \prod_b (\mathbb{I} + B_w) |000...0\rangle . \tag{2.18}$$

Indeed $B_{\tilde{w}} |\psi_{g_1}\rangle = |\psi_{g_1}\rangle$, as $B_{\tilde{w}} \prod_b (\mathbb{I} + B_w) = \prod_b (\mathbb{I} + B_w)$ for all black plaquettes $\tilde{w}$. Also $B_b |\psi_{g_1}\rangle = |\psi_{g_1}\rangle$, as $\sigma^x |0\rangle = |0\rangle$ and B_b commutes with B_w.

The state (2.18) is the only ground state of the Hamiltonian (2.15) on the infinite plane. However, the toric code with periodic boundary conditions actually has four degenerate ground states, while the surface code has two. This will be discussed in more detail in Section 2.2.3.

2.2.2 Anyonic Excitations

The surface and toric codes support anyonic excitations at black and white plaquettes when the corresponding operators (2.16) and (2.17) have the eigenvalue -1. Hence, the ground states correspond to the anyonic vacuum. A Pauli rotation of σ_i^x or σ_i^z applied to site i anti-commutes with the two adjacent black or white operators, respectively, exciting a pair of anyons. A σ_i^x creates a pair of m anyons on black plaquettes, shown in Fig. 2.8 (Right), while a σ_i^z creates a pair of e anyons on white plaquettes. An ϵ anyon is the combination of an m and an e anyon on neighbouring plaquettes. Therefore, a rotation of $\sigma_i^x \sigma_i^z = i\sigma_i^y$ creates a pair of ϵ anyons.

Fusion

The operators B_b and B_w essentially detect the parity of the number of σ^x and σ^z rotations, respectively, on that vertex or plaquette. If two of the same type of Pauli rotations are applied to spins of the same plaquette, then the eigenvalue of the corresponding operator will be $+1$. In other words, if two m or two e anyons are created on the same plaquette they annihilate or fuse to the vacuum. The same is true of ϵ anyons as these are just composite particles made of m and e anyons.

The anyonic fusion rules of the excitations are

$$\begin{aligned} e \times e = m \times m = \epsilon \times \epsilon = 0, \\ e \times m = \epsilon,\ \epsilon \times m = e,\ \epsilon \times e = m, \end{aligned} \tag{2.19}$$

where 0 is the vacuum. These are Abelian anyons as each pair has a unique fusion outcome.

Anyons are moved about the lattice by their corresponding Pauli operators. Each site i is shared by two white plaquettes and two black plaquettes. If there

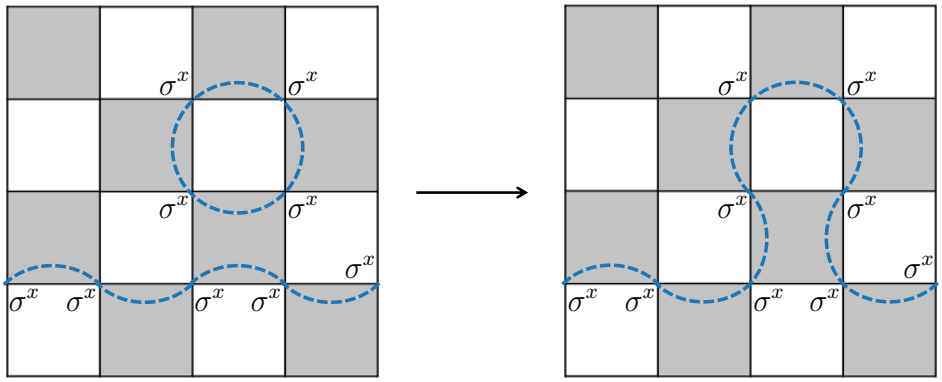

Figure 2.9: The composition of an open and closed string operator consisting of σ^x's deforms the open string about the path of the closed string.

is already an anyon on one of the plaquettes, then applying the corresponding Pauli rotation to site i annihilates the existing anyon and creates one at the other plaquette of the same type. This effectively moves the anyon across the site. Sequences of rotations on neighbouring spins can be thought of as strings of operators with anyons at their end points. The m anyons exist at the ends of strings between black plaquettes, while e anyons are at the ends of strings between white plaquettes.

A closed loop of Pauli rotations produces no anyonic excitations, as the anyons at the ends of the string annihilate with each other. A closed loop of σ^x rotations around a white plaquette w is equivalent to a B_w operator, while a loop of σ^z around a black plaquette b is equivalent to a B_b operator. Closed loops of σ^x's around multiple white plaquettes correspond to the product of the associated white plaquette operators. These closed loops measure the parity of the number of strings of the opposite type passing through them. Equivalently, they measure the parity of the number of anyonic excitations on the enclosed white plaquettes. The same is true of strings of σ^z's around black plaquettes. The product of a closed loop with a bordering open or closed string of the same type deforms the string around the plaquettes or vertices bounded by the loop without shifting any end points. This is shown in Fig. 2.9 for strings of σ^x operators.

Consider the Hamiltonian (2.15) on the infinite plane. The ground state $|\psi_{g_1}\rangle$

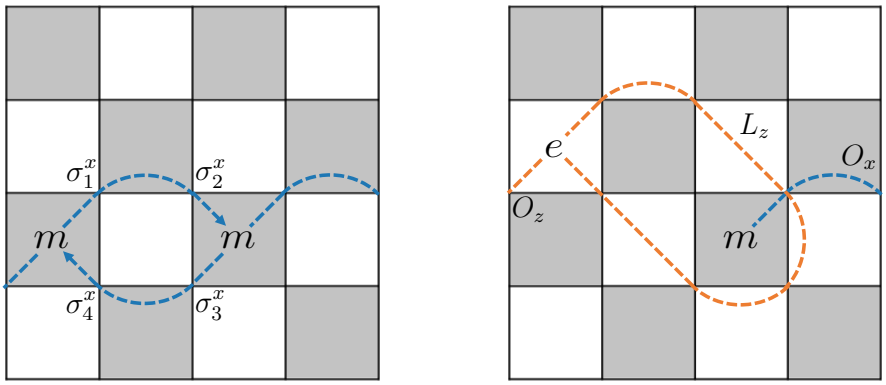

Figure 2.10: (Left) The exchange of two m anyons is equivalent to acting on an empty white plaquette with the operator $B_w = \sigma_4^x \sigma_2^x \sigma_3^x \sigma_1^x$. This has an eigenvalue of $+1$. (Right) An e anyon is braided around an m anyon with the operator L_z. This has an eigenvalue of -1.

in (2.18) is the equal weight superposition of all possible string configurations of closed σ^x loops. Therefore, acting with any closed loop operator maps between different configurations in the superposition and returns the same state. This extends to excited states, which are superpositions of all possible configurations of open strings with the same end points. From this it is easy to see that the specific string configuration of operators producing a pattern of anyonic excitations is not physically significant. Any two configurations with the same end points can be deformed into each other through the application of closed loop operators and hence, describe physically equivalent states. Note that on a finite lattice with open or periodic boundary conditions not all configurations with the same end points can be deformed into each other in such a way. In this situation string configurations which can be deformed into one another form equivalence classes corresponding to different degenerate states. This will be discussed in Section 2.2.3.

Braiding and Exchange Statistics

Take two m anyons, as shown in Fig. 2.10 (Left). Applying the sequence of rotations $B_w = \sigma_4^x \sigma_2^x \sigma_3^x \sigma_1^x$ exchanges the two particles, by acting with a white

plaquette operator on a plaquette with no e anyon. This operator has an eigenvalue of $+1$ for such states, so acts trivially and returns the initial state. A similar argument holds for the e anyons. Therefore, both m and e anyons have bosonic mutual exchange statistics.

Although m and e anyons live on different features of the lattice so can not be exactly exchanged, the exchange statistics can be inferred from fully braiding one around the other. Take a state $|\psi_1\rangle = O_z O_x |\psi_{g_1}\rangle$, where a O_α string operator is built from a line of σ^α rotations. The state $|\psi_1\rangle$ has an m and an e anyon at the ends of the operators O_x and O_z, respectively, as shown in Fig. 2.10 (Right). The e anyon can be braided around the m anyon and back to its original position with a loop operator L_z composed of σ^z rotations. This results in a final state $|\psi_2\rangle = L_z |\psi_1\rangle$. The operator L_z shares a single spin with O_x, so $\{L_z, O_x\} = 0$. It also trivially commutes with O_z, $[L_z, O_z] = 0$. From these commutation relations and the knowledge that L_x acts trivially on the ground state $|\psi_{g_1}\rangle$, it follows that,

$$\begin{aligned} |\psi_2\rangle &= L_z O_z O_x |\psi_{g_1}\rangle \\ &= -O_z O_x L_z |\psi_{g_1}\rangle \\ &= -|\psi_1\rangle . \end{aligned} \tag{2.20}$$

Therefore, the braiding of an m and an e anyon results in a non-trivial topological phase of -1. From this the exchange of an m and an e is taken to produce a phase of $\sqrt{-1} = i$. These exchange statistics are neither fermionic nor bosonic, they are anyonic.

From the exchange statistics of m and e particles with themselves and each other the exchange statistics of any anyon with an ϵ can be deduced. Braiding an m or e around an ϵ is equivalent to braiding it around both an m and e anyon. This has a non-trivial topological phase of -1. Hence, m and e anyons also have anyonic exchange statistics with ϵ anyons, producing a phase of i. Similarly, the exchange of two ϵ anyons is equivalent to exchanging an m and e with an ϵ, which results in a phase of -1. Thus, ϵ anyons have fermionic mutual exchange statistics.

Finally the spin of each anyon can be calculated. The m and e anyons have trivial bosonic spin, as they cannot be rotated. On the other hand, ϵ anyons are rotated by transporting the constituent e anyon around the m anyon through the

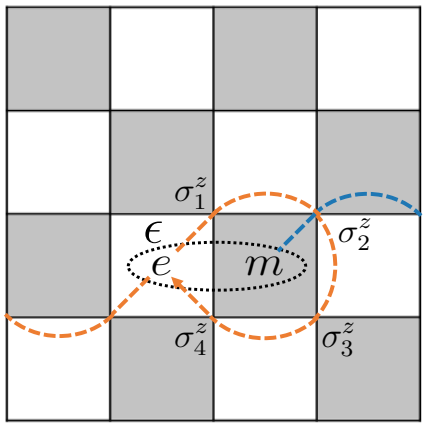

Figure 2.11: An e and an m anyon on neighbouring plaquettes form an ϵ anyon. This can be rotated with the plaquette operator $B_b = \sigma_1^z\sigma_2^z\sigma_3^z\sigma_4^z$ applied to the plaquette supporting the m anyon. This has an eigenvalue of -1.

application of a plaquette operator $B_b = \sigma_1^z\sigma_2^z\sigma_3^z\sigma_4^z$, as shown in Fig. 2.11. This operator acts on a plaquette supporting an m anyon and produces a phase of -1. Transporting the m around the e gives the same result. Rotating a spin s particle by an angle 2π produces a phase factor of $e^{-i2\pi s}$ Bradlyn & Read (1992). Hence, ϵ anyons are spin $1/2$ fermionic particles.

To summaries, m and e particles have bosonic mutual exchange and spin statistics, but have non-trivial anyonic exchange statistics with each other and with ϵ anyons. The ϵ particles have fermionic mutual exchange and spin statistics.

2.2.3 The Surface and Toric Code as Stabilizer Codes

The surface and toric codes are stabilizer codes Brown *et al.* (2016); Browne (2014). A stabilizer code is a quantum error correcting code consisting of n physical qubits, k encoded logical qubits and $n-k$ independent stabilizer generators. The stabilizer generators are the generators of the stabilizer group, the set of n-qubit Pauli operators which leave the encoded logical states invariant. The state space spanned by the encoded logical states is called the code space.

Initially, consider the toric code with periodic boundary conditions on an $L\times L$ lattice. This has $L^2 = n$ physical qubits. The stabilizer generators are the black

and white plaquette operators. There are $L^2/2$ black operators and the same number of white operators. However, the products of all B_b or B_w are

$$\prod_b = B_b = \mathbb{I}, \quad \prod_w B_w = \mathbb{I}. \tag{2.21}$$

Note, this is not true on a lattice with open boundary conditions where all B_b and B_w are independent of one another. In order to make the operators independent on the periodic lattice, one black and one white plaquette operator must be removed from the set of generators. Therefore, there are $L^2 - 2 = n - k$ independent stabilizer generators. This implies there are $2 = k$ encoded logical qubits with 4 logical operators S_{z_1}, S_{x_1}, S_{z_2} and S_{x_2}. The encoded states of the model must be invariant under the application of any element of the stabilizer group. In other words they are ground states of the model. Anyonic excitations correspond to errors in the quantum error correcting code.

The logical operators must commute with all elements of the stabilizer group, while not being elements of the group themselves. This ensures that acting with a logical operator on a state in the code space returns another distinct state in the code space. They must also obey the usual anti-commutation relations, $\{S_{z_1}, S_{x_1}\} = 0$ and $\{S_{z_2}, S_{x_2}\} = 0$. The S_{x_1} operator is a string of σ^x rotations around one of the non-contractible loops of the torus. This is equivalent to creating a pair of m anyons and transporting them around the loop and annihilating them. The S_{x_2} operator is a string of σ^x rotations around the other non-contractible loop. These operators are shown in Fig. 2.8 (Right). The four degenerate ground states of the toric code are given by

$$|\psi_{g_1}\rangle, \quad S_{x_1}|\psi_{g_1}\rangle = |\psi_{g_2}\rangle, \quad S_{x_2}|\psi_{g_1}\rangle = |\psi_{g_3}\rangle, \quad S_{x_1}S_{x_2}|\psi_{g_1}\rangle = |\psi_{g_4}\rangle, \tag{2.22}$$

where $|\psi_{g_1}\rangle$ is given in (2.18). Each of these states are distinct states in the code space as they cannot be mapped to one another through applications of the stabilizer operators. The S_{z_1} operator is a string of σ^z rotations around the opposite non-contractible loop of the torus to S_{x_1}. It intersects with S_{x_1} at one qubit so they satisfy the appropriate anti-commutation relation. The S_{z_2} operator is a string of σ^z rotations around the other loop. These operators are also shown in Fig. 2.8 (Right). The four logical operators produce a four dimensional Hilbert

space. The degenerate ground states (2.22) can be written in terms of the encoded logical qubits as

$$\begin{aligned} |\psi_{g_1}\rangle &= |0\rangle_{L_1} \otimes |0\rangle_{L_2}\,, \quad |\psi_{g_2}\rangle = |1\rangle_{L_1} \otimes |0\rangle_{L_2}\,, \\ |\psi_{g_3}\rangle &= |0\rangle_{L_1} \otimes |1\rangle_{L_2}\,, \quad |\psi_{g_4}\rangle = |1\rangle_{L_1} \otimes |1\rangle_{L_2}\,, \end{aligned} \tag{2.23}$$

where the logical operators act as $S_{x_i}|0\rangle_{L_i} = |1\rangle_{L_i}$, $S_{x_i}|1\rangle_{L_i} = |0\rangle_{L_i}$, $S_{z_i}|0\rangle_{L_i} = |0\rangle_{L_i}$ and $S_{z_i}|1\rangle_{L_i} = -|1\rangle_{L_i}$. An equivalence class of logical operators which act in the same way on states in the code space can be produced by multiplying the logical operators with stabilizer operators. For example, multiplying the operator S_{z_1} by a closed contractible loop of σ^z rotations is equivalent to deforming the path of S_{z_1} around the enclosed loops. However, as we saw in Section 2.2.2 the specific path of an operator is not physically significant and does not change its effect on the state. This equivalence can also be simply derived from the commutation relations of the logical operators with the stabilizers

$$L_\alpha S_{\alpha_i}|\psi_{g_j}\rangle = S_{\alpha_i}|\psi_{g_j}\rangle\,, \tag{2.24}$$

where $\alpha \in (x, z)$, $i \in (1, 2)$ and $j \in (1, 2, 3, 4)$.

Consider now the surface code with open boundary conditions on an $L \times L$ lattice. This has $L^2 = n$ physical qubits. The stabilizer generators are the black and white plaquette operators. There are $(L^2 - 1)/2$ black operators and the same number of white operators. Unlike the toric code all B_b and B_w are independent of one another. Therefore, there are $L^2 - 1 = n - k$ independent stabilizer generators. This implies there is $1 = k$ encoded logical qubits with 2 logical operators S_z and S_x. Similar to the toric code, the encoded states of the model are ground states and anyonic excitations correspond to errors in the quantum error correcting code.

The logical operator S_x is a string of σ^x rotations connecting the top and bottom edges of the lattice. The logical operator S_z is a string of σ^z rotations connecting the left and right edges of the lattice. These operators are shown in Fig. 2.8 (Left). The operator S_x is equivalent to creating an m anyon at the top or bottom edge of the lattice and annihilating it at the opposite edge. Note, m anyons can be created and annihilated at the top and bottom edges of the lattice, while e anyons can be created and annihilated at left and right edges. This is

clear from examination of the checked pattern of the surface code and the specific boundary conditions imposed by the configuration of semicircular plaquettes at the edges.

The logical operators of the surface code share much of the same analysis as those of the toric code. They obey the same anti-commutation relations, $\{S_z, S_x\} = 0$. They produce only two degenerate ground states $|\psi_{g_1}\rangle$ and $S_x |\psi_{g_1}\rangle = |\psi_{g_2}\rangle$, where $|\psi_{g_1}\rangle$ is given in (2.18). These again can be written in terms of the encoded logical qubits as $|\psi_{g_1}\rangle = |0\rangle_L$ and $|\psi_{g_2}\rangle = |1\rangle_L$, such that $S_x |0\rangle_L = |1\rangle_L$, $S_x |1\rangle_L = |0\rangle_L$, $S_z |0\rangle_L = |0\rangle_L$ and $S_z |1\rangle_L = -|1\rangle_L$. Similarly to the toric code, an equivalence class of logical operators which act in the same way on states in the code space can be produced through multiplication with stabilizer operators.

The surface and toric codes provide models for possible quantum memories, as the encoded logical states (2.23) are topologically protected. In order to move from one state to another anyonic excitations must be created and transported around a non-trivial loop of the torus. For sufficiently low error probability this provides increasing protection for states with larger system size Browne (2014). However, it is not able to accomplish universal quantum computation as this an Abelian model and the logical operators produce only phases. Non-Abelian anyons are necessary in order to achieve universal quantum computation, as discussed in Section 2.1.2.

2.3 String-nets and Walker-Wang models

String-nets Levin & Wen (2005) and Walker-Wang models Walker & Wang (2012) are trivalent lattice models in $2+1$ and $3+1$ dimensions, respectively. The links of the lattice take charges corresponding to irreducible representations of a particular group G. The corresponding operators in the Hamiltonian are built from combinations of F (2.6) and R-moves (2.11). String-nets give rise to anyonic emergent quasiparticles. In fact any anyon model in $(2+1)$ can be produced by a string-net with the appropriate group algebra applied to the links. For example, the $\mathbb{Z}_2$ surface code and toric code correspond to $\mathbb{Z}_2$ string-nets with

distinct boundary conditions. The point-like excitations of Walker-Wang models are fermionic or bosonic.

This section is broken down as follows. Section 2.3.1 provides a brief overview of the general form of the Hamiltonians, introducing the vertex and plaquette operators. It also discusses the form of the ground states and excited states. Section 2.3.2 defines the reduced density matrices of models with topologically trivial and non-trivial bipartitions. These formulae are used in Chapter 3 to calculate the interaction distance (2.34) of various anyon models.

2.3.1 Hamiltonians

String-nets and Walker-Wang models are trivalent lattice models in $2+1$ and $3+1$ dimensions, respectively. They describe the behaviour of anyons through the use of F and R-moves. Each link of the lattice has an orientation and a spin located on it which can be in N different states labelled by $i = 0, 1, ..., N-1$. Each spin state corresponds to an anyonic charge in $\mathcal{C}$, given in Section 2.1.1 as the irreducible representation of a group G. A spin in state i corresponds to a string of type i occupying the link orientated in the same direction as the link. The string of type 0 corresponds to the vacuum charge.

The string-net/Walker-Wang Hamiltonian is given by

$$H = -\sum_{v} Q_v - \sum_{p} W_p, \tag{2.25}$$

where the sums run over all vertices v and plaquettes p of the lattice. The vertex operator Q_v acts on the three links a, b and c adjacent to the vertex v and has eigenvalues

$$\delta_{abc} = \begin{cases} 1, & \text{if } N_{ab}^{c} \neq 0 \\ 0, & \text{if } N_{ab}^{c} = 0 \end{cases}, \tag{2.26}$$

where N_{ab}^{c} defines the fusion algebra of anyonic charges given in (2.1) as the group operation of G. Hence, Q_v ensures the ground state string configurations of the model obey the fusion algebra (2.1). The Q_v operator is also called the charge operator as it detects whether there is an open string with anyonic charge at the vertex v.

The plaquette operator is given by

$$W_p = \sum_{i=0}^{N-1} \frac{d_i}{\mathcal{D}^2} W_p^i, \tag{2.27}$$

where W_p^i acts by fusing a string of type i around the plaquette p through a series of F and R-moves. The specific form of this operator depends on the lattice geometry and dimensionality of the model. This will not be discussed here as it is not relevant to the work presented in Chapter 3. For a more in depth look at these Hamiltonians the reader should consult Levin & Wen (2005); Walker & Wang (2012). The plaquette operator is also called the flux operator as it measures the magnetic flux through a plaquette. The ground state corresponds to the state with no magnetic flux.

From equations (2.26) and (2.27) the ground states of these models are the superposition of all possible closed string configurations allowed by the fusion algebra of the model. This is comparable to the ground states of the toric code presented in Section 2.2.

Excited states are produced by acting on a ground state with an open string operator, i.e. by fusing a string of a certain type along a path s picking up phases based on the states of links adjacent to s. Each distinct type of string operator corresponds to a possible quasiparticle excitation of the model and produces a particle antiparticle pair of excitations at the end points of the path s. Thus, they encode the anyonic fusion and braiding statistics of the excitations through a series of F and R-moves. Again the specific form of these operators depends on the lattice geometry and dimensionality and will not be discussed here. Excited states are the superposition of all open string configurations with the same quasiparticle excitation pattern.

The anyon model described by the excitations of string-nets and Walker-Wang models depends on the group G. For example, a $G = \mathbb{Z}_2$ string-net with $\mathcal{C} = \{0, 1\}$ and fusion defined by addition modulo 2 describes the same anyon model as the toric code. The $\mathbb{Z}_2$ string-net supports e anyons on the vertices, m anyons on the plaquettes and ϵ fermions across neighbouring vertices and plaquettes. Although the lattice geometries are different, the anyonic fusion and exchange statistics they describe are identical.

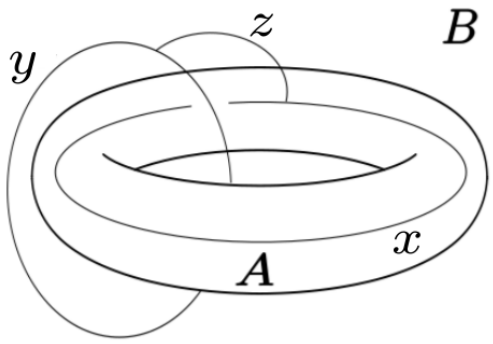

Figure 2.12: A topologically non-trivial toroidal cut of a Walker-Wang model Bullivant & Pachos (2016).

2.3.2 Reduced Density Matrix

Chapter 3 calculates the interaction distance, presented in Section 2.4.3, of string-nets and Walker-Wang models for a variety of groups G. An important quantity for these calculations is the reduced density matrix ρ.

Take the ground state $|\Psi\rangle$ of a string-net or Walker-Wang model partitioned into two regions A and B. The Schmidt decomposition is given by $|\Psi\rangle = \sum_a \lambda_a |\Psi_A^a\rangle |\Psi_b^a\rangle$ Bullivant & Pachos (2016); Li & Haldane (2008), where a indexes all possible string configurations on the boundary ∂A. It is clear that the eigenvalues of the reduced density matrix $\rho = \mathrm{tr}_B(|\Psi\rangle \langle\Psi|)$ Peschel & Chung (2011); Peschel & Eisler (2009) are determined by the probability $|\lambda_a|^2$ of having a certain boundary configuration a of strings. As shown in Section 2.3.1 the ground state is the superposition of all configurations of closed loops. Therefore, for a topologically trivial boundary, such as all boundaries in $2+1$ dimensions or a sphere in $3+1$ dimensions, all strings in a fuse to the vacuum. The associated probabilities $|\lambda_a|^2$ are calculated in Bullivant & Pachos (2016) and the eigenvalues of the reduced density matrix are given by

$$\rho_a = \frac{\prod_{j\in a} d_{x_j}}{\mathcal{D}^{2(|\partial A|-b_0)}}, \tag{2.28}$$

where the 0-th Betti number b_0 is the number of disjoint components of the boundary and $|\partial A|$ is the number of strings crossing the boundary of A.

For Walker-Wang models in $3+1$ dimensions it is possible to take partitions with non-trivial boundary topology. For example, take the boundary of A to be topologically equivalent to a torus. Among the allowed string configurations in the ground state is a braiding of loops with charges x and y supported in A and B respectively. A non zero S^z_{xy} defined in (2.14) allows for the existence of a charge z connecting x and y, piercing ∂A, as shown in Fig. 2.12. The associated probabilities are calculated in Bullivant & Pachos (2016) and the eigenvalues of the reduced density matrix are now given by

$$\rho_{a_z} = \frac{\prod_{j\in a_z} d_{x_j}}{\mathcal{D}^{2|\partial A|}}, \tag{2.29}$$

where a_z labels a boundary configuration fusing to the charge z. Note, only non-Abelian groups G can support configurations with $z \neq 0$ as products of anyonic charges in Abelian groups have single fusion outcomes.

2.4 Interactions in Quantum Many-Body Systems

This section initially provides an overview of free fermion systems. It focuses on properties of the energy and entanglement spectrum that all free fermion systems have in common. These properties are used to define the interaction distance $D_{\mathcal{F}}$ Meichanetzidis *et al.* (2018); Turner *et al.* (2017), a measure of how interacting a many-body state is. An interaction distance of $D_{\mathcal{F}} = 0$ suggests the state has an effective description in terms of free fermions. This could hint at new ways to simulate or solve originally interacting systems with simple free representations. Chapter 3 uses $D_{\mathcal{F}}$ to study a variety of anyon models.

This section is broken down as follows. Section 2.4.1 defines the general form of the Hamiltonian for free fermion systems and discusses interesting properties of the energy spectrum. Section 2.4.2 details the form of the entanglement spectrum and reduced density matrix of free fermion systems. Finally, Section 2.4.3 defines the interaction distance of a many-body state in terms of the corresponding reduced density matrix.

2.4.1 Free Fermion systems

Consider a system of free fermions on a lattice with N sites. Each site, indexed by i, is either occupied by a fermion, $|1\rangle_i$, or unoccupied, $|0\rangle_i$, These states are encoded by fermion creation $\psi_i^\dagger$ and annihilation ψ_i operators, such that $|1\rangle_i = \psi_i^\dagger |0\rangle_i$, $|0\rangle_i = \psi_i |1\rangle_i$ and $\psi_i^\dagger |1\rangle_i = \psi_i |0\rangle_i = 0$. The entire lattice encodes a 2^N dimensional Hilbert space.

Hamiltonians of free fermion systems contain terms which are quadratic in fermion operators, i.e. terms which are products of two fermionic operators. They have the general form

$$H = \sum_{i,j=1}^{N} \left(\alpha_{ij} \psi_i^\dagger \psi_j + \beta_{ij} \psi_i \psi_j + \gamma_i \psi_i^\dagger \psi_i + h.c. \right), \tag{2.30}$$

where $\psi_i^\dagger \psi_j + \psi_i \psi_j^\dagger$ are fermionic hopping terms representing the potential for fermions to hop between sites i and j. The system could be coupled to an external bath producing superconducting terms $\psi_i \psi_j + \psi_i^\dagger \psi_j^\dagger$ characterising the possibility for the exchange of pairs of fermions with the bath. The local chemical potential terms $\psi_i^\dagger \psi_i$ define an energy cost associated to occupying a site i.

This Hamiltonian can be diagonalised by an N dimensional unitary transformation detailed in Lieb *et al.* (1961) to give

$$H = \sum_{i=1}^{N} \epsilon_i \tilde{\psi}_i^\dagger \tilde{\psi}_i, \tag{2.31}$$

where $\tilde{\psi}_i^\dagger$ and $\tilde{\psi}_i$ are linear transformations of the initial fermion operators.

From (2.31) the energy spectrum of a free fermion system has a specific form

$$E_k^f(\epsilon) = \epsilon_0 + \sum_{i=1}^{N} \epsilon_i n_i(k), \tag{2.32}$$

where $n_i(k) \in \{0, 1\}$ is the eigenvalue of $\tilde{\psi}_i^\dagger \tilde{\psi}_i$ and gives the free fermion mode occupation pattern for each many-body state k. The ϵ_i are the single-particle energies corresponding to each mode and ϵ_0 is the energy of the vacuum state.

2.4.2 Entanglement spectrum

Take a free fermion system in the ground state partitioned into two parts A and B. The reduced density matrix is given by $\rho = e^{-H^{\text{ent}}}$ where H^{ent} is the entanglement Hamiltonian Li & Haldane (2008); Peschel & Chung (2011). The spectrum of the entanglement Hamiltonian, also known as the entanglement spectrum E_a^{ent}, has the same form as the spectrum of the full Hamiltonian (2.32) Meichanetzidis *et al.* (2018); Pachos & Papić (2018); Peschel & Eisler (2009); Turner *et al.* (2017). Therefore, the eigenvalues of the reduced density matrix $\rho_a = e^{-E_a^{ent}}$ take the form

$$\rho_a = \exp\left(-\epsilon_0 - \sum_{i=1}^{N} \epsilon_i n_i(a)\right), \tag{2.33}$$

where $n_i(a) \in \{0, 1\}$ gives the mode occupation pattern for each level a of the entanglement spectrum. The ϵ_i are the single-particle energies corresponding to each mode and ϵ_0 is the energy of the vacuum state.

2.4.3 Interaction distance

Interaction distance, $D_{\mathcal{F}}$, is a measure of how far a given state is from any free state Meichanetzidis *et al.* (2018); Turner *et al.* (2017). It is defined as $D_{\mathcal{F}} = \min_{\sigma\in\mathcal{F}} D(\rho, \sigma)$, the minimal trace distance $D(\rho, \sigma)$ between the reduced density matrix ρ of a bipartitioned system and the manifold $\mathcal{F}$ of all possible free-fermion reduced density matrices, σ. Interaction distance can be written as Turner *et al.* (2017)

$$D_{\mathcal{F}}(\rho) = \frac{1}{2} \min_{\{\epsilon\}} \sum_a |\rho_a - \sigma_a(\epsilon)|, \tag{2.34}$$

where ρ_a and σ_a are the eigenvalues of ρ and σ, respectively, arranged in decreasing order. As the state corresponding to σ is free, the eigenvalues σ_a take the form (2.33). The minimisation in (2.34) is over all possible sets of single-particle energies $\{\epsilon_i\}$. Clearly, $D_{\mathcal{F}}$ is dominated by the lowest energies of the entanglement spectrum as σ_a decays exponentially with increasing energy E_a^{ent}.

The next chapter studies the interaction distance of various anyon models by considering the entanglement spectra of sting-nets and Walker-Wang models presented in Section 2.3.2. In particular the $\mathbb{Z}_2$ string-net corresponding to the $\mathbb{Z}_2$

surface code or toric code is identified as having $D_{\mathcal{F}} = 0$. This suggests that they have a free fermion representation. Such representations are explored in Chapter 4.

2.5 Summary

This chapter provided a brief introduction to a wide range of topics concerning anyon models and interaction distance. This started with a summary of anyon models, focusing on their fusion and braiding statistics. The toric code was then reviewed, a specific example of a lattice model supporting anyonic excitations. This was followed by a short review of string-nets and Walker-Wang models along with the properties of their reduced density matrices. Finally, the interaction distance was defined as the minimal trace distance between the reduced density matrix of a state and the manifold of all free-fermion reduced density matrices.

All of these areas will be relevant in Chapter 3 when the interaction distance of string-nets and Walker-Wang models is used to quantify the role of interactions in anyon models.

Chapter 3

Interactions in string-nets and Walker-Wang models

This chapter addresses the problem of quantifying the role of interactions in general classes of topological states of matter in $2+1$ and $3+1$ dimensions by using the interaction distance $D_{\mathcal{F}}$ Turner *et al.* (2017) as a measure of the distinguishability of these states from free-fermion states. Specifically, string-nets Levin & Wen (2005) and Walker-Wang models Walker & Wang (2012) defined with a selection of Abelian and non-Abelian groups are considered here. Even though these models have excitations that exhibit anyonic statistics all topological states of certain models can be exactly described by free fermions. The distribution of $D_{\mathcal{F}}$ values for the states of these models shows that some models saturate the maximum possible $D_{\mathcal{F}}$, while others have states that are Gaussian states with $D_{\mathcal{F}} = 0$.

While the interaction distance $D_{\mathcal{F}}$ is defined in (2.34) for a quantum state, it can be redefined as the thermal interaction distance $D_{\mathcal{F}}^{\text{th}}$ Pachos & Papić (2018) allowing one to probe the full energy spectrum of a system, as seen in Section 4.1.1. The study of interaction distance presented in this Chapter suggests there is a wide range of models with possible free fermion representations. This is used in Chapter 4 along with an investigation of the thermal interaction distance to motivate the search for local unitary mappings of the $\mathbb{Z}_2$ surface and toric code to free fermions and free fermions coupled to fermionic symmetry operators, respectively.

This chapter is organised as follows. Section 3.1 calculates the interaction distance of string-nets with a variety of finite groups parametrising the edges of the lattice. Section 3.1.1 shows that Abelian $\mathbb{Z}_N$ string-nets have flat entanglement spectra with degeneracy N. The distribution of the interaction distance of $\mathbb{Z}_2$ string-nets shows that they all either admit a free-fermion description for any partition if $N = 2^n$, $n \in \mathbb{N}$, or maximise $D_{\mathcal{F}}$ for a large fraction of the partitions if $N \neq 2^n$. The set of string-nets with $D_{\mathcal{F}} = 0$ includes the $\mathbb{Z}_2$ string-net, which is equivalent to the $\mathbb{Z}_2$ surface or toric code. This is used in Section 4.1 when discussing the free fermion signatures of these models. Section 3.1.2 numerically calculates the interaction distance of the non-Abelian $SU(2)_k$ string-nets for all levels $2 \leq k \leq 20$. The interaction distance of all such models is found to be $D_{\mathcal{F}} \neq 0$. This implies it is not possible to find a free fermion description of these non-Abelian string-net models. Section 3.2 then studies the interaction distance of Walker-Wang models, comparing the interaction distance of different partitions. It is shown that the interaction distance of non-Abelian Walker-Wang models depends not only on the size of the cut but also on the topology of the partition.

3.1 String-nets

This section calculates the interaction distance for a wide range of string-nets. The eigenvalues of the reduced density matrix for any string-net are given by (2.28). Thus allowing one to determine analytically the entanglement spectra of all string-net models, Abelian or non-Abelian, and for any partition.

3.1.1 Abelian

Initially consider a string-net with the irreducible representations of an Abelian group $\mathbb{Z}_N$ parametrising the edges of the lattice bipartitioned into A and B. Fig. 3.1 (Left) shows an example of such a bipartition. These models have $d_x = 1$ Bonderson (2007) for all $x \in \mathcal{C}$ and thus $\mathcal{D} = \sqrt{N}$ from (2.10). According to (2.28) the corresponding reduced density matrix $\bar{\rho}(\chi)$ for any bipartition of the ground state has a flat spectrum with degeneracy $\chi = N^k$ and eigenvalues

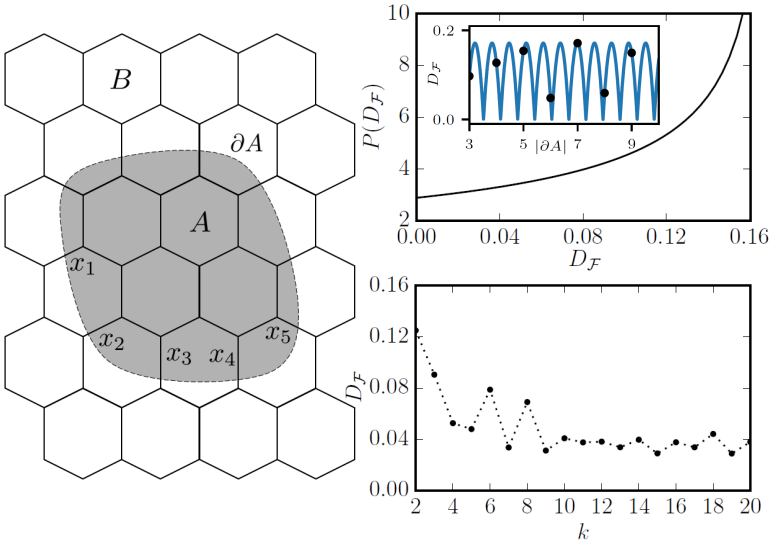

Figure 3.1: (Left) The string-net model on a honeycomb lattice with a bipartition into A and B. For this bipartition $|\partial A| = 10$ and $b_0 = 1$. A configuration of charges x_j is depicted at the links of the boundary ∂A. (Right, Top) Distribution $P(D_\mathcal{F})$ of the interaction distance for varying $|\partial A|$. (Inset) The dots represent the numerically obtained interaction distance as a function of $|\partial A|$. (Right, Bottom). Plot of $D_\mathcal{F}$ for $\mathrm{SU}(2)_k$ against k for a partition with $|\partial A| = 3$.

$\bar{\rho}_a = 1/\chi = 1/N^k$ for all a, where $k = |\partial A| - b_0$, the 0-th Betti number b_0 is the number of disjoint components of the boundary ∂A and $|\partial A|$ is the number of strings crossing ∂A. In fact equation (2.28) can be generalised to give the eigenvalues of the reduced density matrix for a bipartition of any eigenstate of the model as

$$\rho_{a_c} = \frac{\prod_{j \in a_c} d_{x_j}}{\mathcal{D}^{2|\partial A| - b_0}}, \tag{3.1}$$

where a_c labels boundary configurations which fuse to the charge c. From (3.1) it is clear that the reduced density matrix of a bipartition of any excited state of a $\mathbb{Z}_n$ string-net is the same as that of the ground state.

In order to find the optimal free model corresponding to the minimal $D_\mathcal{F}$ for a flat probability spectrum, with $\bar{\rho}_a = 1/\chi$ for all a, let n be the greatest integer such that $2^n \leq \chi$. Assume that the optimal free fermion spectrum is of the form

$$\sigma_{\text{ansatz}} \simeq \mathrm{diag}\big(\chi^{-1}, \ldots, \chi^{-1}, p, \ldots, p\big), \tag{3.2}$$

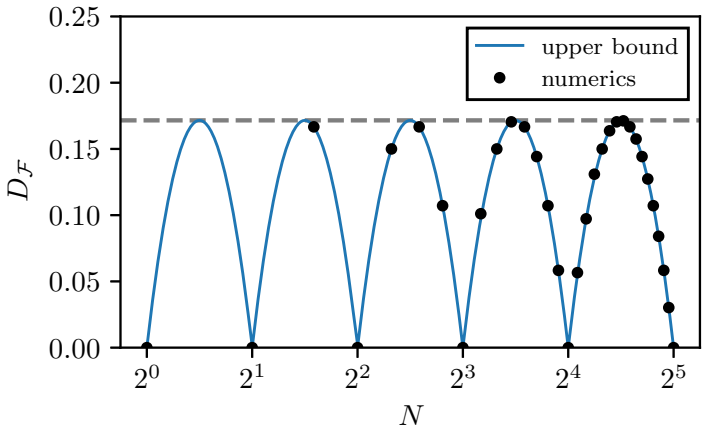

Figure 3.2: Interaction distance $D_{\mathcal{F}}(\bar{\rho})$ for flat spectra of rank N. The solid blue line is the analytical upper bound given in (3.3). The dashed line is the maximal value $D_{\mathcal{F}}^{\max}$. The dots are results of numerical optimisation and coincide with the analytic upper bound.

where there are 2^n entries for each value χ^{-1} and p. The normalisation $\mathrm{tr}(\sigma_{\mathrm{ansatz}}) = 1$ implies $p = 2^{-n} - \chi^{-1}$. The trace distance $D(\bar{\rho}(\chi), \sigma_{\mathrm{ansatz}})$ forms an upper bound for $D_{\mathcal{F}}(\bar{\rho}(\chi))$ given in Meichanetzidis *et al.* (2018) as

$$D_{\mathcal{F}}(\bar{\rho}(\chi)) \leq 3 - \frac{\chi}{2^n} - \frac{2^{n+1}}{\chi}. \tag{3.3}$$

To evaluate $D(\bar{\rho}(\chi), \sigma_{\mathrm{ansatz}})$ the spectrum of $\bar{\rho}(\chi)$ is padded with zeros until $\bar{\rho}$ and σ_{ansatz} have the same number of entries. This procedure is always viable as it leaves the entropy invariant Turner *et al.* (2017).

In Meichanetzidis *et al.* (2018) the upper bound (3.3) is found to be in agreement with the numerically computed $D_{\mathcal{F}}(\bar{\rho}(\chi))$, as shown in Fig. 3.2. Numerical minimisation for values up to $\chi = 2^8$ never finds results below the analytic upper bound making a convincing case that the upper bound is the exact result. The upper bound is also shown analytically to be equal to $D_{\mathcal{F}}(\bar{\rho}(\chi))$ for $\chi \leq 6$. Hence, the upper bound of (3.3) is assumed to be exactly $D_{\mathcal{F}}(\bar{\rho}(\chi))$ from here on.

From (3.3) the maximum of the interaction distance is $D_{\mathcal{F}}^{\max} = 3 - 2\sqrt{2}$. This maximum is approached by rational approximations $\chi/2^n$ of $\sqrt{2}$ for increasing n, as shown in Fig. 3.2.

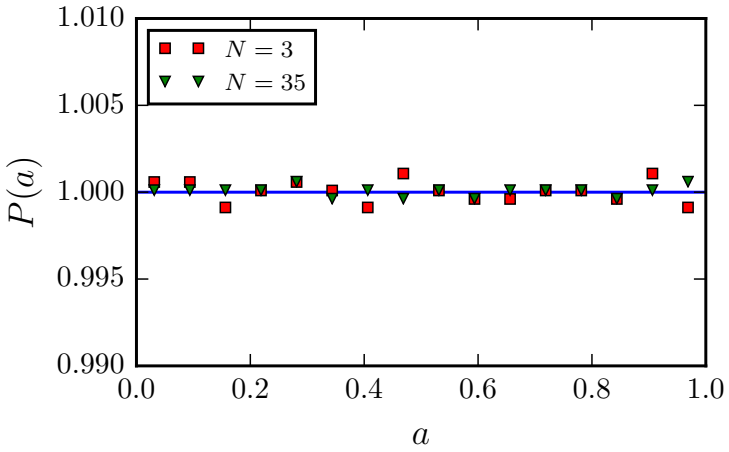

Figure 3.3: Distribution $P(a)$ for varying k in the cases of $N = 3$ and $N = 35$. The line is the analytic result $P(a) = 1$. The markers are numerical results for a sample up to $k = 2^{15} - 1$.

Returning to $\mathbb{Z}_N$ string-nets, the case when $N = 2^n$ can be exactly described by fermionic zero modes. For any boundary size $|\partial A|$ the interaction distance is exactly $D_{\mathcal{F}} = 0$. Hence, the eigenstates of these models are Gaussian states. This is a surprising result as anyonic quasiparticles are expected to emerge in interacting systems. Nevertheless, the optimal free models are not necessarily local and their energy spectrum is not necessarily given by filling of single fermion modes. The case $N = 2$ corresponds to the toric code Kitaev (2003), presented in Section 2.2. A free fermionic representation of the toric model is the $\mathcal{A}$ phase of Kitaev's honeycomb model Kitaev (2006) reviewed in Section 5.1.5. Chapter 4 demonstrates that it is possible to find a local unitary transformation mapping the $\mathbb{Z}_2$ surface code Bombin & Martin-Delgado (2007); Bravyi *et al.* (2017) (the open boundary version of the toric code) to free fermions and presents its explicit form. It also presents the explicit form of a local unitary transformation mapping the toric code to free fermions with an interacting fermionic parity operator.

On the other hand, when $N \neq 2^n$, $D_{\mathcal{F}}$ is always non-zero. In particular, its value depends on the size $|\partial A|$ and the number of disjoint components b_0 of the partition boundary. Its behaviour can be investigated by studying the distribution $P(D_{\mathcal{F}})$ of $D_{\mathcal{F}}$ by varying $k \in \mathbb{N}$ for a certain model $\mathbb{Z}_N$. An intermediate step in

the calculation of $P(D_{\mathcal{F}})$ is finding the density function for $P(a)$, where $a = \log_2 \chi \pmod 1 = \log_2 N^k \pmod 1$ is a variable describing the position of χ between powers of 2.

If $N \neq 2^n$ then $\log_2 N$ is irrational. This implies $a = k \log_2 N \pmod 1$ for each k, which uniformly samples the interval $[0, 1]$ and hence $P(a) = 1$ over that interval. Fig. 3.3 compares this prediction for fixed N against a sample of k up to $2^{15} - 1$. Assuming (3.3) is an equality, the interaction distance can be written as $D_{\mathcal{F}}(\bar{\rho}(\chi)) \leq 3 - 2^a - 2^{1-a}$.

From the distribution $P(a)$ and the relation $P(D_{\mathcal{F}}) = P(a)(\frac{dD_{\mathcal{F}}}{da})^{-1}$ the distribution $P(D_{\mathcal{F}})$, for fixed N, is given by,

$$P(D_{\mathcal{F}}) = \frac{2/\ln 2}{\sqrt{1 + D_{\mathcal{F}}(D_{\mathcal{F}} - 6)}}. \tag{3.4}$$

Surprisingly, this is independent of N. Hence, there exist partitions that asymptotically maximise $D_{\mathcal{F}}$ for all $N \neq 2^n$, as shown in Fig. 3.1 (Right, Top). Therefore, all $\mathbb{Z}_N$ Abelian string-nets either admit a free-fermion description for any partition or they maximise $D_{\mathcal{F}}$ for a large fraction of the partitions.

3.1.2 Non-Abelian

Next consider non-Abelian string-net models. For concreteness, take the finite group to be $SU(2)_k$ for various levels $k \geq 2$. This group gives rise to string-net models that support a large class of non-Abelian anyons, such as the Ising anyons for $k = 2$, with statistics similar to Majorana fermions, or the Fibonacci anyons for $k = 3$, that are universal for quantum computation Pachos (2012); Trebst *et al.* (2008). The interaction distance for a boundary around a single vertex that has $|\partial A| = 3$ is considered here for simplicity. The interaction distance for all $k \leq 20$ is found numerically to be $D_{\mathcal{F}} \neq 0$, as shown in Fig. 3.1 (Right, Bottom). Hence, it is not possible to find a free fermion description of these non-Abelian string-net models. This suggests interactions are necessary for non-Abelian anyons in these stabilizer fixed point Hamiltonians. Interestingly non-Abelian Ising anyons occur in the Kitaev honeycomb model, reviewed in Section 5.1, which has a representation in terms of free fermions coupled to a $\mathbb{Z}_2$ gauge field.

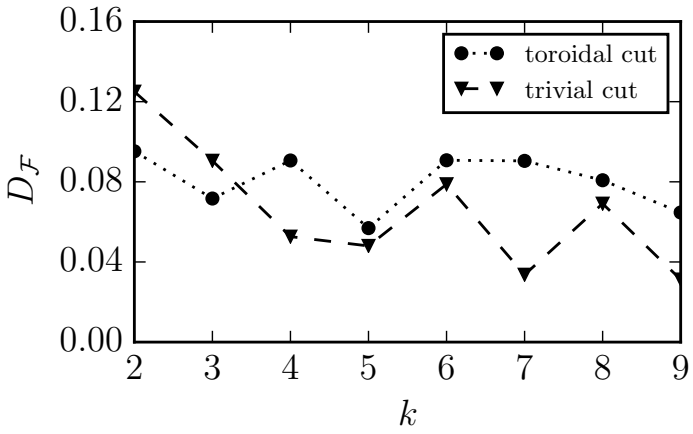

Figure 3.4: A plot of $D_{\mathcal{F}}$ against k-level for a toroidal and a topologically trivial partition, both with $|\partial A| = 3$.

3.2 Walker-Wang Models

While the string-net models can be directly generalised to three spatial dimensions, a more powerful generalisation is in terms of the Walker-Wang models Walker & Wang (2012). These models allow non-trivial braiding of the charges giving a rich behaviour in their bulk and at their boundary von Keyserlingk & Burnell (2015); von Keyserlingk *et al.* (2013).

The entanglement spectrum for topologically trivial cuts of a Walker-Wang model can be found in the same way as for string-nets given by (2.28). Partitions with trivial boundary topology have the same entanglement spectrum, and hence interaction distance as string-nets with the same group structure. Nevertheless, partitions with non-trivial boundary topology reveal novel correlation properties Bullivant & Pachos (2016). To identify their effect on the interaction distance take the region A with a boundary topologically equivalent to a torus, as shown in Fig. 2.12. Among the allowed configurations in the ground state is a braiding of loops with charges x and y supported in A and B respectively, connected by a string of charge z piercing ∂A Bullivant & Pachos (2016). Thus, the probability spectrum should now encode information about the non-trivial braiding of the charges. The eigenvalues of the reduced density matrix are now given by (2.29). Fig. 3.4 shows $D_{\mathcal{F}}$ for a toroidal cut compared to a trivial cut of

non-Abelian SU(2)$_k$ Walker-Wang models as a function of the level $k \geq 2$, where $|\partial A| = 3$. It is clear that the interaction distance depends not only on the size of the cut but also on the topology of ∂A. Its non-zero value indicates the necessity of interactions for the existence of non-Abelian topological order also in these three dimensional stabilizer fixed point Hamiltonians.

3.3 Conclusions

This chapter has quantified the effect of interactions in states of topological phases of matter $2+1$ and $3+1$ dimensions. It was found that in string-nets, the size of the partition boundary plays a role in determining the value of $D_{\mathcal{F}}$, but not its geometry. For Walker-Wang models the topology of the boundary also becomes relevant.

Surprisingly, all states of both the $\mathbb{Z}_{2^n}$ string-nets and Walker-Wang models have $D_{\mathcal{F}} = 0$ for any bipartition. It was also demonstrated by studying the distribution $P(D_{\mathcal{F}})$ of $D_{\mathcal{F}}$ that all $\mathbb{Z}_N$ string-nets and Walker-Wang models, with $N \neq 2^n$, maximise $D_{\mathcal{F}}$ for a large fraction of the partitions. The interaction distance was found to be $D_{\mathcal{F}} \neq 0$ for the non-Abelian $SU(2)_k$ string-nets and Walker-Wang models for $2 \leq k \leq 20$. This seems to suggest that interactions are necessary for the emergence of excitations with non-Abelian anyonic statistics in these string-nets and Walker-Wang models.

More generally, this work makes use of the interaction distance to find models with possible fermionic representations, which could be employed to solve these quantum Hamiltonians. This is possible if a system has $D_{\mathcal{F}} = 0$ for all possible bipartitions and in all eigenstates, while at the same time the energy spectrum is also free. Note that $D_{\mathcal{F}} = 0$ in all eigenstates can be compatible with anyon statistics because the latter only emerges when one interpolates adiabatically between different sectors of the conserved charges of the model Lahtinen & Pachos (2009a).

This work is will prove to be significant for the study of fermionic representations of the $\mathbb{Z}_2$ surface and toric codes in Chapter 4. Interestingly, even though the individual states and energy spectra are free, one must introduce highly non-local

interacting excitation operators in order to encode the exotic anyonic statistics of the models.

Chapter 4

Free fermion representation of the topological surface code

Investigation of the toric code's eigenstates in terms of the interaction distance Turner *et al.* (2017), presented in Chapter 3, showed that they are equivalent to free fermion states Meichanetzidis *et al.* (2018). This chapter will show there is a more general equivalence. Not only are all eigenstates of the toric code Gaussian states having entanglement spectra given in terms of free fermions, but the energy spectrum has a similar decomposition in terms of single particle energies. Hence, it is expected that a unitary transformation exists that maps the toric code to a free fermion Hamiltonian. Nevertheless, a free fermion system can support neither anyonic statistics nor eigenstates with non-trivial topological entanglement entropy. Hence, these properties have to be encoded non-trivially in the unitary transformation that maps between these two physically different models.

This chapter demonstrates that indeed it is possible to find a unitary transformation $\mathcal{U}_S$ that maps the surface code to free fermions and presents its explicit form. It also presents the explicit form of a unitary transformation $\mathcal{U}_T$ mapping the toric code to free fermions with an interacting fermionic parity operator, which ensures the excitations of the model are created in pairs, as in the toric code. These transformations comprise of products of C_4 Clifford rotations You *et al.* (2016) that act on each plaquette, and are directly generalisable to arbitrary size systems. The resulting system of the surface code transformation consists of

free fermion modes with local chemical potentials, that encode the single particle excitations of the plaquettes, and of a single zero energy fermion mode that does not appear in the Hamiltonian, encoding the logical state of the model. The quasiparticle excitations of the toric code on the other hand always come in pairs. Therefore, as the unitary transformation is isospectral, it cannot map the toric code to a system of this form. The fermionic description of the toric code needs to be highly non-local in order to give rise to non-trivial topological order Yao & Qi (2010), articulated here by a non-local fermionic parity operator ($\mathbb{Z}_2$ symmetrisation) coupled to the fermionic modes of the system. This ensures any excitations are created in pairs, thus fixing the isospectral nature of the transformation. The fermionic system also has an extra zero mode encoding the second logical qubit of the toric code. The possibility to transform the surface code to free fermions could have a variety of applications, e.g. in condensed matter, by dissecting the way anyonic statistics emerge, or in quantum information, as free fermion systems and their manipulation have a very efficient descriptions Bravyi (2004); Bravyi *et al.* (2017).

The chapter is organised as follows. Section 4.1 shows the $\mathbb{Z}_2$ surface and toric code are representable in terms of free fermions. It also provides the specific form of these representations by studying the stabilizer group structure of the models. Section 4.2 explicitly presents the local unitary transformations $\mathcal{U}_S$ and $\mathcal{U}_T$ that map between the surface and toric code, respectively, and their fermionic counterparts for arbitrary size systems. Section 4.3 studies the resulting models showing how the states of the models split into "dynamic" and "zero" (or "logical") modes. Section 4.4 looks at how string operators transform between the systems. It is demonstrated how the mapping keeps endpoints of anyonic string operators fixed, while extending their support into the dynamic and logical modes of the fermionic systems. Finally, it is shown that highly non-local interacting operators are required to encode the anyonic excitation statistics of the surface and toric code in excitations of the fermion models.

4.1 Free Fermion Signature

This section details the properties of the $\mathbb{Z}_2$ surface and toric code which suggest they are representable in terms of free fermions. The interaction distance $D_{\mathcal{F}}$ Meichanetzidis *et al.* (2018); Turner *et al.* (2017) is used to study the entanglement and energy spectra and show that they both exactly correspond to those of free fermions. The stabilizer groups of both the surface and toric code are then shown to be isomorphic to groups generated by commuting Pauli operators, thus giving a description of the form of the unitarily equivalent fermion models.

4.1.1 Entanglement and Energy Spectra

This section considers the entanglement and energy spectra of the $\mathbb{Z}_2$ surface and toric code. The entanglement spectrum can be studied with the interaction distance $D_{\mathcal{F}} = \min_{\sigma\in\mathcal{F}} D(\rho,\sigma)$ Meichanetzidis *et al.* (2018); Turner *et al.* (2017), defined in Section 2.4.3 as the minimal trace distance $D(\rho,\sigma)$ of a given reduced density matrix ρ to the manifold $\mathcal{F}$ of all Gaussian density matrices (2.34). Section 3.1 calculates the interaction distance all eigenstates of the $\mathbb{Z}_2$ surface and toric code to be $D_{\mathcal{F}} = 0$ for any possible bipartition.

The energy spectrum $\{E_k\}$ of a system can be probed with the thermal interaction distance $D^{\text{th}}_{\mathcal{F}} = \min_{\sigma\in\mathcal{F}} D(\rho^{\text{th}}(\beta),\sigma)$ Pachos & Papić (2018), defined as the minimal trace distance $D(\rho^{\text{th}}(\beta),\sigma)$ of a given thermal density matrix $\rho^{\text{th}}(\beta) = \frac{1}{Z}e^{-\beta H}$ to the manifold $\mathcal{F}$ of all Gaussian density matrices, where $Z = \text{tr}(e^{-\beta H})$ is the partition function, H is the Hamiltonian and $T = \frac{1}{\beta}$ is the temperature. The eigenvalues of ρ^{th} have the form $\rho^{\text{th}}_k = \frac{1}{Z}e^{-\beta E_k}$. The energy spectrum of free states takes the form (2.32). For the surface and toric code, the energy spectrum is given by the syndrome pattern of anyonic excitations at plaquettes. These excitations all have the same energy contribution, as seen from (2.15). Thus, the spectrum of the surface code can be reproduced with a set of L^2-1 single particle energies $\{\epsilon_j\}$, corresponding to the L^2-1 plaquettes of the $L\times L$ surface code, arranged in all possible occupation patterns. Similarly, the spectrum of the toric code can be reproduced with a set of L^2 single particle energies, corresponding to the L^2 plaquettes of the $L\times L$ toric code, arranged in all possible occupation patterns with *even* total occupation number.

The total occupation must be equal as all excitations in toric code are created in pairs. Therefore, the thermal interaction distance of these codes is $D_{\mathcal{F}}^{\text{th}} = 0$. This implies the codes are isospectral to free fermion systems, suggesting there should exist unitary transformations, $\mathcal{U}$, mapping the codes to such isospectral free fermion models.

4.1.2 Group Structure

This section studies the stabilizer group structure of the $\mathbb{Z}_2$ surface and toric code, presented in Section 2.2.3, to find the form of the fermionic models they map to. Section 2.2.3 gives the generators of the surface code stabilizer group as the set of all black B_b (2.16) and white B_w (2.17) plaquette operators. These plaquette operators all square to one and commute with each other. This group is isomorphic to a group generated by a set of commuting Pauli operators,

$$\left\langle B_p | B_p^2 = B_\lambda B_\eta B_\lambda B_\eta = \mathbb{I} \right\rangle \cong \left\langle \sigma^z_{i \forall i=1,\ldots,|\mathcal{P}|} \right\rangle, \tag{4.1}$$

where $\mathcal{P}$ is the set of all plaquettes on the lattice. This suggests it should be possible to map each plaquette operator of the surface code to a single free fermion mode.

The toric code has the added restriction that the product of all plaquette operators supported on a black, B_b, or white, B_w, plaquette, respectively, must be equal to the identity. Therefore, the set of stabilizer generators is two smaller than the set of all plaquettes $\mathcal{P}$. The group generated by these operators is isomorphic to a group generated by a set of commuting Pauli operators two smaller than $|\mathcal{P}|$,

$$\left\langle B_p | B_p^2 = B_\lambda B_\eta B_\lambda B_\eta = \prod_{p \in \mathcal{P}_b} B_p = \prod_{p \in \mathcal{P}_w} B_p = \mathbb{I} \right\rangle \cong \left\langle \sigma^z_{i \forall i=1,\ldots,|\mathcal{P}|-2} \right\rangle, \tag{4.2}$$

where $\mathcal{P}_b$ and $\mathcal{P}_w$ are the set of all black and white plaquettes, respectively. The resulting group generated by the Pauli operators in (4.2) will be one quarter the size of that in (4.1), for a fixed $|\mathcal{P}|$. All plaquette operators in the toric code will be mapped to free fermion modes, except one black and one white operator which will each be mapped to fermionic parity operators over the set of all black

and white modes, respectively. These symmetry terms are a result of the periodic boundary conditions of the toric code and the fact that excitations in the code are created in pairs. Hence, even though the toric code is isospectral to a free fermion model, as seen in Section 4.1.1, by studying the group structure of the code these interacting fermionic parity operators are found to be necessary to ensure excitations are created in pairs in the transformed model, as they are in the toric code. This is discussed in more detail in Section 4.4.

4.2 The Transformation

This section presents the transformation of the $\mathbb{Z}_2$ surface Bombin & Martin-Delgado (2007); Bravyi *et al.* (2017) and toric code Kitaev (2003) to free fermions and fermions with fermionic parity operators, respectively. The representations of the codes used here are the ones presented in Section 2.2. However, in order to see the effect of such transformations on the codes and their operators a specific form must be chosen for the logical operators of each code. The logical operators of the $L \times L$ surface code S_x and S_z, defined in Section 2.2.3, are chosen to have support on the L physical qubits along the left and bottom of the lattice, respectively. This choice is shown for the 3×3 surface code in Fig. 2.8 (Left).

The toric code logical operators can be chosen arbitrarily as long as S_{x_1} and S_{z_2} loop around the same non-contractible loop of the torus, S_{z_1} and S_{x_2} loop around the other, and the appropriate commutation and anti-commutation relations are obeyed, detailed in Section 2.2.3. For any $L \times L$ toric code choose all logical operators to be of length L and parallel loops S_{x_i} and S_{z_j}, where $i \neq j$ to be a distance $L/2$ from each other. This choice is shown for the 4×4 toric code in Fig. 2.8 (Right). The logical operators of both codes still form equivalence classes of logical operators when multiplied with stabilizer operators, as described in Section 2.2.3.

The surface code Hamiltonian H_{SC} is transformed by the unitary transformation $\mathcal{U}_S$, while the toric code Hamiltonian H_{TC} is transformed by $\mathcal{U}_T$ as

$$\begin{aligned} \mathcal{U}_S H_{\mathrm{SC}} \mathcal{U}_S^\dagger &= H_{\mathrm{FS}} \\ \mathcal{U}_T H_{\mathrm{TC}} \mathcal{U}_T^\dagger &= H_{\mathrm{FT}}, \end{aligned} \tag{4.3}$$

where H_{FS} is a free fermion Hamiltonian and H_{FT} is a fermionic Hamiltonian, consisting of free fermion terms coupled two interacting fermionic parity operators.

The explicit forms of the unitaries $\mathcal{U}_S$ and $\mathcal{U}_T$ are presented here. These unitaries take a general form suitable for any system size. To achieve this C_4 Clifford rotations You *et al.* (2016) are employed, taking the form,

$$R_{C_4}(\sigma^{[\mu]}) = \exp(\frac{i\pi}{4}\sigma^{[\mu]}) = \frac{1}{\sqrt{2}}(1 + i\sigma^{[\mu]}), \tag{4.4}$$

where σ^{μ_i} is the Pauli matrix acting on the ith qubit and $\sigma^{[\mu]} \equiv \sigma^{\mu_1\mu_2\mu_3\cdots} \equiv \sigma^{\mu_1} \otimes \sigma^{\mu_2} \otimes \sigma^{\mu_3} \otimes ...$ is the direct product of some set of Pauli matrices. The action of R_{C_4} on a matrix $\sigma^{[\nu]}$ is given by,

$$\begin{aligned} \sigma^{[\nu]} &\to R^{\dagger}_{C_4}(\sigma^{[\mu]})\sigma^{[\nu]}R_{C_4}(\sigma^{[\mu]}) \\ &= \begin{cases} \sigma^{[\nu]}, & \text{if } [\sigma^{[\nu]}, \sigma^{[\mu]}] = 0, \\ i\sigma^{[\nu]}\sigma^{[\mu]}, & \text{if } \{\sigma^{[\nu]}, \sigma^{[\mu]}\} = 0. \end{cases} \end{aligned} \tag{4.5}$$

These rotations can be used to map a collection of spin operators to a spin operator on a single qubit and the identity everywhere else. For example,

$$\begin{aligned} \sigma^{[\mu]x[\nu]} &\xrightarrow{R_{C_4}(-\sigma^{[\mu]y[\nu]})} -i\sigma^{[\mu]x[\nu]}\sigma^{[\mu]y[\nu]} = \sigma^{[0\ldots]z[0\ldots]} \\ \sigma^{[\mu]z[\nu]} &\xrightarrow{R_{C_4}(\sigma^{[\mu]y[\nu]})} i\sigma^{[\mu]z[\nu]}\sigma^{[\mu]y[\nu]} = \sigma^{[0\ldots]x[0\ldots]}, \end{aligned} \tag{4.6}$$

where $\sigma^0 = \mathbb{I}$.

Initially consider the surface code mapping $\mathcal{U}_S$. The purpose of $\mathcal{U}_S$ is to transform each plaquette stabilizer, B_p, in H_{SC} to an operator, $\tilde{B}_p = \sigma^z = 1 - 2a^{\dagger}a$ Nielsen (2005) on a single free fermion mode or spin, while mapping the logical operators S_x and S_z to operators $\tilde{S}_x = \sigma^x = a^{\dagger} + a$ and $\tilde{S}_z = \sigma^z = 1 - 2a^{\dagger}a$ with support on a shared zero mode, not in H_{FS}, and hence separate from those supporting $\tilde{B}_p$ operators. The operators $a^{\dagger}$ and a are fermionic creation and annihilation operators, respectively. The transformation $\mathcal{U}_S$ is split into $N + 2$ unitaries,

$$\mathcal{U}_S = U_{N+2}...U_2U_1, \tag{4.7}$$

where $N = L^2 - 1$ is the number of plaquettes in the $L \times L$ surface code. Each of the U's has a similar structure, transforming one of the L^2-1 plaquette stabilizers,

or 2 logical operators into single spin operators. The first $N/2$ unitary parts, $\{U_1, ..., U_{N/2}\}$, correspond to the transformation of black plaquette operators with support on four qubits, $B_b^{\text{IV}} = \sigma^{[0...]zzzz[0...]}$, or two qubits, $B_b^{\text{II}} = \sigma^{[0...]zz[0...]}$, as shown in Fig. 4.1(a) and (b). The mappings take the form,

$$\begin{aligned} B_b^{\text{IV}} &\xrightarrow{R_{C_4}(\sigma^{[0...]yzzz[0...]})} \sigma^{[0...]x000[0...]} \xrightarrow{R_{C_4}(-\sigma^{[0...]y000[0...]})} \sigma^{[0...]z000[0...]}, \\ B_b^{\text{II}} &\xrightarrow{R_{C_4}(\sigma^{[0...]yz[0...]})} \sigma^{[0...]x0[0...]} \xrightarrow{R_{C_4}(-\sigma^{[0...]y0[0...]})} \sigma^{[0...]z0[0...]}, \end{aligned} \tag{4.8}$$

where $R_{C_4}(\sigma^{[0...]yzzz[0...]})R_{C_4}(-\sigma^{[0...]y000[0...]})$ is one unitary part, U. We label the resulting operators $\tilde{B}_b^{\text{IV}} = \sigma^{[0...]z000[0...]}$ and $\tilde{B}_b^{\text{II}} = \sigma^{[0...]z0[0...]}$. These operators have support on the top left qubit of the corresponding plaquette b or just the top qubit for the order two stabilizers. All other Pauli operators in the C_4 rotation are equal to those in the operator being mapped from at each stage, but at this top left qubit the Pauli operator is replaced with a σ^y in the first step and a $-\sigma^y$ in the second. There is a lot of freedom in the choice of the specific form of C_4 rotations throughout this section. For example, the first R_{C_4} could have a $-\sigma^y$ and the second could have a σ^y. This section just presents two particular collections of C_4 rotations that work for the surface and toric code, respectively. These $N/2$ unitary parts act in order from the top to bottom row of the lattice. This ensures that their effect on all other black plaquettes are trivial. The effect of these unitaries on the white (X) plaquettes, however are non-trivial. Fig. 4.1(b) and (c) shows that some σ^x operators of the white plaquettes are mapped to σ^z operators by the first $N/2$ unitaries. These σ^x operators are those with support on the same qubits as the σ^y operators in 4.8, indicated by the blue arrows.

The white plaquette stabilizers are mapped by the next $N/2$ unitary parts to σ^z operators on the bottom right qubit of the plaquette, or the right qubit in the case of the order two operators. They are mapped individually, each by their own U in order from the right to left column. The form of the U's that perform this mapping vary depending on the effect of the U's corresponding to the black plaquettes. The mapping $(U_{N/2}...U_1)$ acts trivially on the semi circle plaquette stabilizers on the bottom row of the lattice, as shown in Fig. 4.1(c), $(U_{N/2}...U_1)B_w^{\text{II}}(U_1^\dagger...U_{N/2}^\dagger) = B_w^{\text{II}} = \sigma^{[0...]xx[0...]}$. For these types of plaquettes the

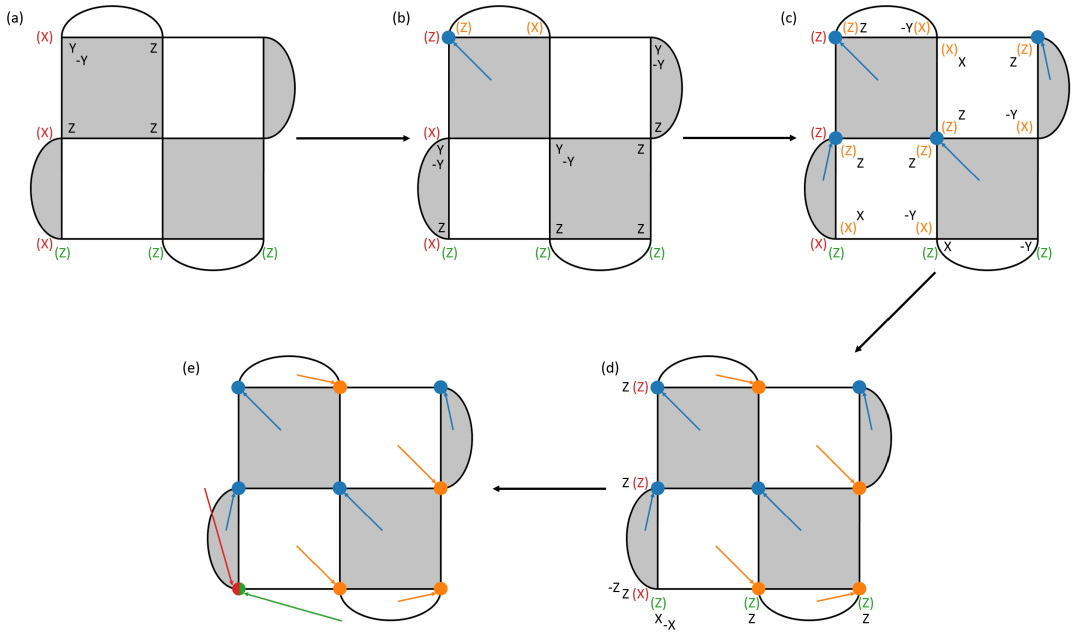

Figure 4.1: Mapping of the 3×3 surface code under $\mathcal{U}_S$. (a) Rotations $R_{C_4}(\sigma^{[0\ldots]yzzz[0\ldots]})$ and $R_{C_4}(-\sigma^{[0\ldots]y000[0\ldots]})$ acting on the top left black plaquette stabilizer B_{b_1} are labelled in black on the interior of b_1. (b) Blue arrows indicate the free fermion modes supporting transformed black plaquette stabilizers $\tilde{B}_b$. The letters in parentheses show the form of operators acted on non-trivially by the rotations. The letters are orange for white plaquettes, red for S_x and green for S_z. Rotations for the other three black plaquettes are labelled in black in their interior. (c) The C_4 rotations corresponding to the white plaquettes are labelled in black in their interior. (d) Orange arrows show the positions of free fermion modes supporting transformed white plaquette stabilizers, $\tilde{B}_w$. The rotations mapping $(U_N...U_1)S_x(U_1^\dagger...U_N^\dagger)$ and $(U_N...U_1)S_z(U_1^\dagger...U_N^\dagger)$ to a single σ^x and σ^z, respectively, with support on the logical mode are labelled along the left and bottom of the lattice. (e) Red and green arrows point to the logical mode supporting $\tilde{S}_x$ and $\tilde{S}_z$.

rotations take the form,

$$B_w^{\mathrm{II}} \xrightarrow{R_{C_4}(-\sigma^{[0\ldots]xy[0\ldots]})} \sigma^{[0\ldots]0z[0\ldots]} \tag{4.9}$$

All others are acted on non-trivially, such as the top right square plaquette stabi-

lizer, B_w^{IV}, in Fig. 4.1(c), $(U_{N/2}...U_1)B_w^{\mathrm{IV}}(U_1^\dagger...U_{N/2}^\dagger) = \bar{B}_w^{\mathrm{IV}} = \sigma^{[0...]xzzx[0...]}$, where $\bar{B}_w^{\mathrm{IV}}$ labels the intermediate form of the operator. For such an operator of the rotation takes the form,

$$\bar{B}_w^{\mathrm{IV}} \xrightarrow{R_{C_4}(-\sigma^{[0...]xzzy[0...]})} \sigma^{[0...]000z[0...]}, \tag{4.10}$$

where the Pauli operators in the R_{C_4} rotation are equal to those in the operator being mapped from, $\bar{B}_w^{\mathrm{IV}}$, except at the bottom right qubit of the plaquette where the σ^x is replaced with a $-\sigma^y$. The operator on the bottom right qubit of a white plaquette is always unaffected by any previous U's by construction, thus will remain a σ^x.

Once the N plaquette operators have been transformed, the logical operators are transformed with the two remaining unitaries, U_{N+1} and U_{N+2}. The logical operator, S_x is mapped by all previous unitaries to a string of σ^z operators along the left boundary attached to a σ^x on the bottom left qubit of the lattice, where it intersects with S_z, which is acted on trivially by all previous unitaries. These intermediate forms of the operators are labelled as $\bar{S}_x = \sigma^{[0...]xzz...[0...]}$ and $\bar{S}_z = \sigma^{[0...]zzz...[0...]}$, respectively. They are both shown in Fig. 4.1(d), along with the form of U_{N+1} and U_{N+2}, for a 3×3 lattice. These act as,

$$\begin{aligned} \bar{S}_x &\xrightarrow{R_{C_4}(\sigma^{[0...]zzz...[0...]})} \sigma^{[0...]y00...[0...]} \xrightarrow{R_{C_4}(-\sigma^{[0...]z00...[0...]})} \sigma^{[0...]x00...[0...]}, \\ \bar{S}_z &\xrightarrow{R_{C_4}(\sigma^{[0...]xzz...[0...]})} -\sigma^{[0...]y00...[0...]} \xrightarrow{R_{C_4}(-\sigma^{[0...]x00...[0...]})} \sigma^{[0...]z00...[0...]} \end{aligned} \tag{4.11}$$

for a general size code. Thus S_x and S_z are mapped to $\tilde{S}_x = \sigma^{[0...]x00...[0...]}$ and $\tilde{S}_z = \sigma^{[0...]z00...[0...]}$, respectively, with support on a single shared qubit. U_{N+1} and U_{N+2} act trivially on all previously obtained $\tilde{B}_b$ and $\tilde{B}_w$ operators.

The toric code mapping $\mathcal{U}_T$ take a similar form to $\mathcal{U}_S$. $\mathcal{U}_T$ transforms each plaquette stabilizer, B_p, in H_{TC} to an operator $\tilde{B}_p = \sigma^z$ on a single free fermion mode, except one black, B_{b_1}, and one white, B_{w_1}, stabilizer, which are mapped to symmetry operators, $\tilde{P}_{b_1} = \prod_{b \setminus b_1} \tilde{B}_b$ and $\tilde{P}_{w_1} = \prod_{w \setminus w_1} \tilde{B}_w$, which are the products of all other black and white transformed stabilizers, respectively. The four logical operators, S_{x_1}, S_{z_1}, S_{x_2} and S_{z_2}, are mapped to operators $\tilde{S}_{x_1} = \sigma_j^x$, $\tilde{S}_{z_1} = \sigma_j^z$, $\tilde{S}_{x_2} = \sigma_k^x$ and $\tilde{S}_{z_2} = \sigma_k^z$ with support on two zero modes j and k not in

the Hamiltonian H_{TS}, and hence separate from those supporting $\tilde{B}_p$ operators. The operator $\mathcal{U}_T$ is split into $M+2$ unitaries,

$$\mathcal{U}_T = U_{M+2}...U_2U_1, \tag{4.12}$$

where $M = L^2$ is the number of plaquettes in the $L \times L$ toric code. Each of the U's transforms one of the L^2 plaquette stabilizers, or 4 logical operators into single spin operators. The first $M/2-1$ unitary parts, $\{U_1, ..., U_{M/2-1}\}$, correspond to the transformation of black plaquette operators, $B_b = \sigma^{[0...]zzzz[0...]}$, as shown in Fig. 4.2(a) and (b). The mappings take the following form,

$$B_b \xrightarrow{R_{C_4}(\sigma^{[0...]yzzz[0...]})} \sigma^{[0...]x000[0...]} \xrightarrow{R_{C_4}(-\sigma^{[0...]y000[0...]})} \sigma^{[0...]z000[0...]}, \tag{4.13}$$

where $\tilde{B}_b = \sigma^{[0...]z000[0...]}$. This operator has support on one of the four qubits of the corresponding plaquette b the same qubit that supports the σ^y operators in the C_4 rotations. These qubits are the ones positioned at the heads of blue arrows in Fig. 4.2(c) to (f). The orientation of unitary parts, and hence these arrows, vary depending on the location of plaquette b on the lattice. The rule for an arbitrarily sized $L \times L$ lattice with the S_{x_i} operators positioned along the central row and column and the S_{z_i} operators along the top row and left column of the lattice, as depicted in Fig. 4.2, goes as follows. The blue arrows of plaquettes in the top right quarter of the lattice point towards the bottom left, those in the bottom left and right quarters point towards the top right and left, respectively, and those in the top left in general point towards the bottom right. There are two exceptions to this rule. One of which is the top left plaquette, which will be mapped to a symmetry operator $\tilde{P}_{b_1}$ with support over all other $\tilde{B}_b$ plaquettes, labelled by underlined blue (Z)'s in Fig. 4.2(c) to (f). Hence, it does not have a unitary part, U, corresponding to it. The second exception is all other plaquettes in the top left quarter of the lattice that run along the diagonal line of black plaquettes from the top left to the bottom right of the lattice. All arrows along this diagonal point towards the top left of the lattice. The orientation of all arrows for the 6×6 toric code is shown in Fig. 4.3.

These $M/2-1$ unitary parts act in a certain order. No unitary part may act before the unitary corresponding to the plaquette their arrow points at. So

as can be seen from Fig. 4.2 the first plaquette is the one whose arrow points towards the top left plaquette, as this has no unitary part of its own. This ordering ensures that the effect of each part on all other black plaquettes that are yet to be transformed is trivial. However, the effect of each of these parts on the top left plaquette is non-trivial. This is mapped to a symmetry operator $\tilde{P}_{b_1}$ consisting of a σ^z supported at each qubit supporting a $\tilde{B}_b$. This non-trivial effect is marked in Fig. 4.2(b) to (f), by the position of underlined blue (Z)'s. Similarly to the surface code mapping, the effect of these unitaries on the white plaquettes are also non-trivial. Fig. 4.2(b) to (d) shows that some σ^x operators on white plaquettes are mapped to σ^z operators by the first $M/2-1$ unitaries. These σ^x operators are those with support on the qubits pointed at by the blue arrows.

The next $M/2-1$ unitary parts each act on a white plaquette stabilizer mapping them to single σ^z operators. The form of the U's that perform this mapping vary depending on the effect of the U's corresponding to the black plaquettes. The mapping $(U_{M/2-1},...,U_1)$ acts trivially on the two plaquette stabilizers in the bottom left and top right corner of the lattice, as is shown in Fig. 4.2(c), $(U_{N/2}...U_1)B_w(U_1^\dagger...U_{N/2}^\dagger) = B_w = \sigma^{[0...]xxxx[0...]}$. For these plaquettes the rotation takes the form,

$$B_w \xrightarrow{R_{C_4}(-\sigma^{[0...]xyxx[0...]})} \sigma^{[0...]0z00[0...]} \tag{4.14}$$

All others are acted on non-trivially, such as the leftmost plaquette on the top row, B_w, in Fig. 4.2(c), $(U_{M/2-1}...U_1)B_w(U_1^\dagger...U_{M/2-1}^\dagger) = \bar{B}_w = \sigma^{[0...]xxzz[0...]}$, where $\bar{B}_w$ labels the intermediate form of the operator. For such an operator the rotation takes the form,

$$\bar{B}_w \xrightarrow{R_{C_4}(-\sigma^{[0...]yxzz[0...]})} \sigma^{[0...]z000[0...]}, \tag{4.15}$$

where the Pauli operators in the R_{C_4} rotation are equal to those in the operator being mapped from, $\bar{B}_w$, except at the top left qubit where the σ^x is replaced with a $-\sigma^y$. The operator on the qubit that will support the final $\tilde{B}_w$ operator will always be unaffected by any previous U's by construction, thus will remain a σ^x. These qubits are the ones positioned at the heads of orange arrows in Fig. 4.2(e) and (f). The orientation of the second $M/2-1$ unitaries, and hence

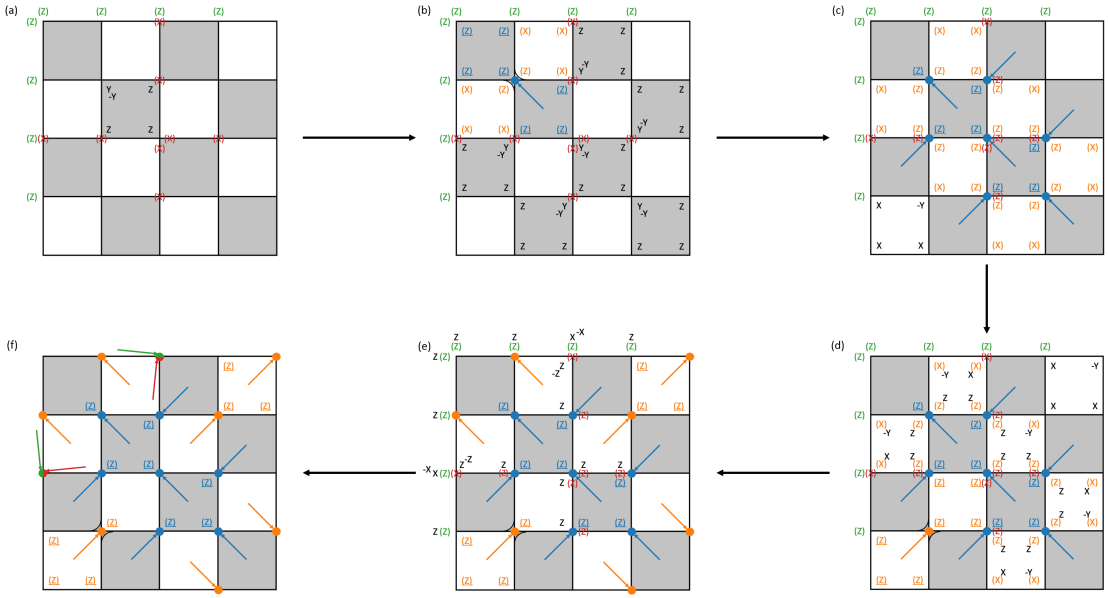

Figure 4.2: Mapping of the 4×4 toric code under $\mathcal{U}_T$ (a) Rotations $R_{C_4}(\sigma^{[0...]yzzz[0...]})$ and $R_{C_4}(-\sigma^{[0...]y000[0...]})$ acting on the black plaquette stabilizer B_{b_2} are labelled in black on the interior of b_2. (b) Blue arrows indicate the fermion modes supporting transformed black plaquette stabilizers $\tilde{B}_b$. The letters in parentheses show the form of operators acted on non-trivially by the rotations. The letters are orange for white plaquettes, blue for black plaquettes, red for X logical operators and green for Z logical operators. They are underlined for the two plaquette operators that will be mapped to fermionic parity operators. Rotations for the remaining black plaquettes are labelled in black in their interior. (c) The C_4 rotation corresponding to the bottom left white plaquette is shown labelled in black in its interior. (d) Orange arrows show the positions of fermion modes supporting transformed white plaquette stabilizers $\tilde{B}_w$. Rotations for the remaining white plaquettes are shown in their interior. (e) Rotations mapping the partially transformed logical operators to single Pauli operators with support on the two logical modes are labelled in black. (f) Red and green arrows point to the logical modes supporting $\tilde{S}_{x_1}$, $\tilde{S}_{z_1}$, $\tilde{S}_{x_2}$ and $\tilde{S}_{z_2}$. The black $\tilde{P}_{b_1}$ and white $\tilde{P}_{w_1}$ symmetry operators are labelled in blue and orange, respectively, with support on all transformed operators of the same colour.

the orange arrows, are fixed in a similar way to the first $M/2-1$. The rule for an arbitrarily sized $L \times L$ lattice goes as follows. The orange arrows of plaquettes in the top left and right quarters of the lattice point towards the top left and right, respectively, those in the bottom right quarters point towards the bottom right, and those in the bottom left in general point towards the bottom left. There are again two exceptions to this rule. One of which is the top rightmost plaquette in the bottom left quarter, which will be mapped to a symmetry operator $\tilde{P}_{w_1}$ with support over all other $\tilde{B}_w$ plaquettes, labelled by underlined orange (X)'s in Fig. 4.2(e) and (f), and thus does not have a unitary part corresponding to it. The second is all other plaquettes in the bottom left quarter of the lattice which run along the diagonal line of white plaquettes from the top right to the bottom left of the lattice. All other arrows along this diagonal point towards the top right of the lattice. The orientation of all arrows for the 6×6 toric code is shown in Fig. 4.3.

As with the first $M/2-1$ unitary parts, the second $M/2-1$ act in a particular order. No unitary part may act before the unitary corresponding to the plaquette their arrow points at. As can be seen from Fig. 4.2 the first plaquette must be the one whose arrow points towards the top right plaquette of the bottom left quarter of the lattice, as this has no unitary part of its own. This ordering ensures that the effect of each part on all other white plaquettes that are yet to be transformed is trivial.

Once all plaquette operators have been mapped to single σ^z operators or symmetry operators the logical operators are transformed with the four remaining unitaries $U_{M-1}, ..., U_{M+2}$. The logical operators S_{x_1} and S_{x_2}, are mapped by all previous unitaries to strings of σ^z operators along the qubits they originally had support on with a σ^x on the qubits that intersect with S_{z_1} and S_{z_2}, respectively. While S_{z_1} and S_{z_2} are acted on trivially by all previous unitaries. These intermediate forms of the operators are labelled as $\bar{S}_{x_1} = \sigma^{[0...]xzz...[0...]}$, $\bar{S}_{x_2} = \sigma^{[0...]xzz...[0...]}$, $\bar{S}_{z_1} = \sigma^{[0...]zzz...[0...]}$ and $\bar{S}_{z_2} = \sigma^{[0...]zzz...[0...]}$. They are shown in Fig. 4.2(e), along with the form of the unitaries $U_{M-1}, ..., U_{M+2}$, for a 4×4 lattice. These act as,

$$\begin{aligned} \bar{S}_{x_1} &\xrightarrow{R_{C_4}(\sigma^{[0...]zzz...[0...]})} \sigma^{[0...]y00...[0...]} \xrightarrow{R_{C_4}(-\sigma^{[0...]z00...[0...]})} \sigma^{[0...]x00...[0...]}, \\ \bar{S}_{z_1} &\xrightarrow{R_{C_4}(\sigma^{[0...]xzz...[0...]})} -\sigma^{[0...]y00...[0...]} \xrightarrow{R_{C_4}(-\sigma^{[0...]x00...[0...]})} \sigma^{[0...]z00...[0...]}, \end{aligned} \tag{4.16}$$

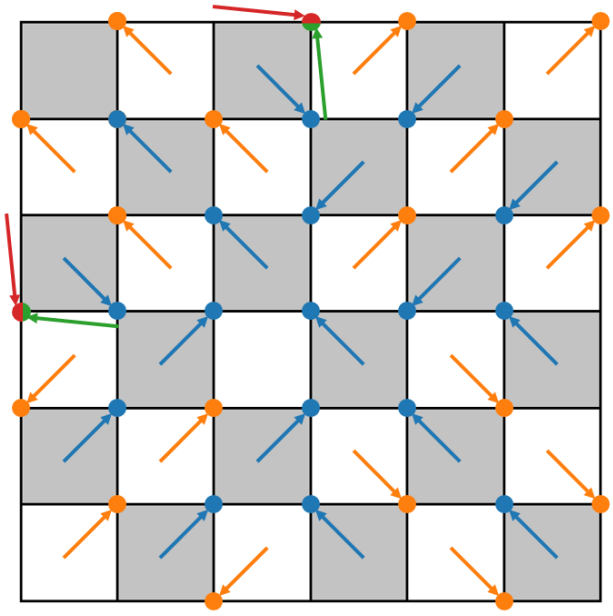

Figure 4.3: The orientation of all unitary parts U_i for the 6×6 toric code.

where the operators $\bar{S}_{x_2}$ and $\bar{S}_{z_2}$ are transformed in a similar way. Thus S_{x_1}, S_{z_1}, S_{x_2} and S_{z_2} are mapped to $\tilde{S}_{x_1} = \sigma_j^x$, $\tilde{S}_{z_1} = \sigma_j^z$, $\tilde{S}_{x_2} = \sigma_k^x$ and $\tilde{S}_L^{z_2} = \sigma_k^z$. The unitaries $U_{M-1}, ..., U_{M+2}$ act trivially on all previously obtained $\tilde{B}_b$ and $\tilde{B}_w$ operators.

4.3 The Fermion Models

This section focuses on the properties of the models, H_{FS} and H_{FT}, that result from the transformations (4.3) of the surface and toric code, respectively. Initially consider the surface code. The plaquette stabilizers are mapped to σ^z operators on free spins (qubits), which are equivalent to free fermion modes. The excitations of plaquettes can now be encoded by the occupation of isolated dynamic fermion modes subject to a local chemical potential that encode the corresponding increase of the energy by 2 when the plaquettes are populated. As a result the Hamiltonian of the transformed model is,

$$H_{\mathrm{FS}} = -\sum_p \tilde{B}_p, \tag{4.17}$$

where $\tilde{B}_p = \sigma^z = 1 - 2a^\dagger a$ Nielsen (2005), and $a^\dagger$ and a are fermionic creation and annihilation operators, respectively.

Applying $\mathcal{U}_T$ to a state of the surface code, $|\psi\rangle_{\mathrm{S}}$, gives,

$$\mathcal{U}\,|\psi\rangle_{\mathrm{SC}} = |\tilde{\psi}\rangle_{\mathrm{SC}}. \tag{4.18}$$

In general for a distance L code, any given state, $|\tilde{\psi}\rangle_{\mathrm{SC}}$, has $L^2 - 1$ dynamic modes, each corresponding to a plaquette of the surface code and one zero mode, which supports the transformed logical operators, $\tilde{S}_x$ and $\tilde{S}_z$. The ground state, $|\psi_g\rangle_{\mathrm{SC}}$, of the original surface code, H_{SC}, is stabilized by all plaquette operators, i.e. $B_p\,|\psi_g\rangle_{\mathrm{SC}} = |\psi_g\rangle_{\mathrm{SC}}$ for all plaquettes p. This relationship is preserved by the transformation, $\mathcal{U}_T$. Therefore, $\tilde{B}_p|\tilde{\psi_g}\rangle_{\mathrm{SC}} = |\tilde{\psi_g}\rangle_{\mathrm{SC}}$ for all p, implying the ground state of this model is a collection of $L^2 - 1$ empty free fermion modes, with a degeneracy of 2 encoded by the logical zero mode. Occupied dynamic modes indicate the positions of local anyonic excitations in this model.

The transformed $L \times L$ toric code, H_{FT}, has many of the same properties as H_{FS}. The Hamiltonian is,

$$H_{\mathrm{FT}} = -\sum_{b\setminus b_1} \tilde{B}_b - \sum_{w\setminus w_1} \tilde{B}_w - \prod_{b\setminus b_1} \tilde{B}_b - \prod_{w\setminus w_1} \tilde{B}_w), \tag{4.19}$$

where $b\setminus b_1$ and $w\setminus w_1$ are the sets of all black and white plaquettes, respectively, minus the plaquettes, b_1 and w_1, that become fermionic symmetry operators over all other transformed plaquettes of the same colour. These symmetry operators are $\tilde{P}_{b_1} = \prod_{b\setminus b_1} \tilde{B}_b$ and $\tilde{P}_{w_1} = \prod_{w\setminus w_1} \tilde{B}_w$ in (4.19). The other $L^2 - 2$ transformed plaquette stabilizers have the same form as those in (4.17), $\tilde{B}_p = \sigma^z = 1 - 2a^\dagger a$.

Any transformed state has $L^2 - 2$ dynamic modes, each corresponding to a plaquette of the toric code and two zero modes, which support the four transformed logical operators. The ground state, $|\psi_g\rangle_{\mathrm{TC}}$, of the toric code is stabilized by all plaquette operators, i.e. $B_p\,|\psi_g\rangle_{\mathrm{TC}} = |\psi_g\rangle_{\mathrm{TC}}$ for all p. Hence, the transformed ground state, $|\tilde{\psi_g}\rangle_{\mathrm{TC}}$, is stabilized by all transformed plaquette stabilizers, including the symmetry operators, $\tilde{B}_p|\tilde{\psi_g}\rangle_{\mathrm{TC}} = \tilde{P}_{b_1}|\tilde{\psi_g}\rangle_{\mathrm{TC}} = \tilde{P}_{w_1}|\tilde{\psi_g}\rangle_{\mathrm{TC}} = |\tilde{\psi_g}\rangle_{\mathrm{TC}}$ for all p, implying the ground state is a collection of $L^2 - 2$ empty free fermion modes, with a degeneracy of 4 encoded by the two logical zero modes. Occupied dynamic modes indicate the positions of local anyonic excitations in this model.

A single occupied mode b would result in an increase in energy due to the violated stabilizer operator $\tilde{B}_b$ and symmetry operator $\tilde{S}_{b_1}$. This reflects the fact that excitations are created in pairs at the ends of string operators in H_{TC} with one end of the string at plaquette b and one at b_1. The symmetry operators $\tilde{P}_{b_1}$ and $\tilde{P}_{w_1}$ restrict excitations in H_{FT} to also be created in pairs. A more detailed discussion of the excitations of H_{FS} and H_{FT} is provided in the next section.

4.4 Encoding Anyonic Statistics in Free Fermions

Previous sections have shown that the $\mathbb{Z}_2$ surface and toric code are unitarily equivalent to a free fermion model and to free fermions coupled to two interacting fermionic parity operators, respectively. Hence, these models should have equivalent physical properties. Nevertheless, operators on single fermion modes cannot account for the anyonic statistics supported by the surface and toric code. The exotic statistics of the excitations arises due to the commutation and anti-commutation relations of the σ^x and σ^z's the string operators are built from. This section shows how these relations are preserved by the unitary transformations $\mathcal{U}_S$ and $\mathcal{U}_T$ and how they are encoded in the action of non-local interacting operators on the dynamic and logical modes of the system.

The string operators of the surface code $O_x^{C_S}$ and $O_z^{C_S}$, introduced in Section 2.2.2, are a product of σ_j^x or σ_j^z operators, respectively, along the path C_S. They produce local excitations at their endpoints. Crossings of these strings give rise to the anyonic statistics through the Pauli commutation relations. These string operators transform as follows,

$$\begin{aligned} \mathcal{U}_S O_x^{C_S} \mathcal{U}_S^\dagger &= \tilde{O}_x^{\tilde{C}_S} \\ \mathcal{U}_S O_z^{C_S} \mathcal{U}_S^\dagger &= \tilde{O}_z^{\tilde{C}_S}, \end{aligned} \tag{4.20}$$

where $\tilde{O}_x^{\tilde{C}_S}$ and $\tilde{O}_z^{\tilde{C}_S}$ are string operators acting on the dynamical and logical fermion modes along the path $\tilde{C}_S$ in H_{FS}.

All commutation relations of operators are preserved by $\mathcal{U}_S$. If $O_x^{C_S}$ creates an excitation at plaquette b, then $\{O_x^{C_S}, B_b\} = 0 = \{\tilde{O}_x^{\tilde{C}_S}, \tilde{B}_b\}$. If not, $[O_x^{C_S}, B_b] = 0 = [\tilde{O}_x^{\tilde{C}_S}, \tilde{B}_b]$. Hence, the endpoints of $\tilde{C}_S$ are the transformed versions of the plaquettes, which were the endpoints of C_S. Paths between endpoints of string

operators may change, but the endpoints are fixed at the transformed versions of the plaquettes. Hence, the paths remain homotopically equivalent to those of the untransformed operators. The commutation relations of operators with each other are also preserved, by the mapping $\mathcal{U}_S$. Crossings of these strings may appear in the dynamic or logical modes. Therefore, the anyonic statistics of excitations of the surface code are encoded in the free model by a mix of the dynamic and logical modes.

It is more instructive to look at how string operators $\tilde{O}_\alpha^{\tilde{C}_S}$ in the free model H_{FS} are mapped under the inverse unitary transformation $\mathcal{U}_S^\dagger$ to string operators $O_\alpha^{C_S}$ in the surface code H_{SC}. A σ^x operator on a single spin (or $a^\dagger + a$ on a single mode) in the free model transforms to a string operator with one end point at the plaquette p corresponding to that spin (or mode) and one at a boundary not associated with a logical degree of freedom. This will be the top boundary if p is black and the right if p is white. This has to be the case as it is the only type of operator that anti-commutes with just one plaquette. This also suggests why there could not exist a unitary transformation from the toric code to decoupled free fermions without the symmetry operators in (4.19). If each plaquette in the toric code were mapped to a fermion mode in the free model, any operator creating a single fermion population would be mapped to one creating a single plaquette excitation in the toric code. However, all excitations in the toric code must be created in pairs, as dictated by its periodic boundary conditions. In other words, the boundary conditions of the surface code are what facilitate such a mapping.

A string operator with end points on any two plaquettes of the same colour in the surface code may be obtained by mapping from a product of two σ^x's at the modes corresponding to those plaquettes in H_{FS}. Consider the string operators $\tilde{O}_x^{\tilde{C}_S}$ and $\tilde{O}_z^{\tilde{C}_S}$ that map to string operators $O_x^{C_S}$ and $O_z^{C_S}$ creating logical excitations, i.e. those with end points at the bottom and left boundaries, respectively. These operators contain $\tilde{S}_x$ and $\tilde{S}_z$, respectively. Any other string operator $O_x^{C_S}$ or $O_z^{C_S}$ with the same end points and effect on the logical qubit as those already mentioned may be obtained by including some combination of σ^z's in the operators $\tilde{O}_x^{\tilde{C}_S}$ or $\tilde{O}_z^{\tilde{C}_S}$. These σ^z's alter the string operator's path by

applying stabilizer operations, thus including a loop around the corresponding plaquette to the path, C_S.

The string operators of the toric code $O_x^{C_T}$ and $O_z^{C_T}$, introduced in Section 2.2.2, are a product of σ_j^x or σ_j^z operators, respectively, along the path C_T. These operators are mapped via the unitary transformation $\mathcal{U}_T$ to string operators in a system of fermion modes coupled to two fermionic parity constraints, in a similar way to those in the surface code,

$$\begin{aligned} \mathcal{U}_T O_x^{C_T} \mathcal{U}_T^\dagger &= \tilde{O}_x^{\tilde{C}_T} \\ \mathcal{U}_T O_z^{C_T} \mathcal{U}_T^\dagger &= \tilde{O}_z^{\tilde{C}_T}, \end{aligned} \tag{4.21}$$

where $\tilde{O}_x^{\tilde{C}_T}$ and $\tilde{O}_z^{\tilde{C}_T}$ are string operators acting on the dynamical and logical fermion modes along the path $\tilde{C}_T$ in H_{FT}.

The commutation relations of operators are preserved by $\mathcal{U}_T$. If $O_x^{C_T}$ creates an excitation at a black plaquette b, then $\{O_x^{C_T}, B_b\} = 0 = \{\tilde{O}_x^{\tilde{C}_T}, \tilde{B}_b\}$ and $\{\tilde{O}_x^{\tilde{C}_T}, \tilde{P}_{b_1}\} = 0$. If $b = b_1$ then $\tilde{B}_b = \tilde{P}_{b_1}$. If $O_x^{C_T}$ does not create an excitation at any black plaquette then, $[O_x^{C_T}, B_b] = 0 = [\tilde{O}_x^{\tilde{C}_T}, \tilde{B}_b]$ and $[\tilde{O}_x^{\tilde{C}_T}, \tilde{P}_{b_1}] = 0$ for all b. Hence, the endpoints of $\tilde{C}_T$ are the transformed versions of the plaquettes, which were the endpoints of C. Paths between endpoints of string operators may change, but the endpoints remain fixed. As in the surface code transformation the commutation relations of operators with each other are also preserved by the mapping $\mathcal{U}_T$. Crossings of these strings may appear in the dynamic or logical modes. Therefore, as with the surface code mapping, the anyonic statistics of excitations of the toric code are encoded in the fermionic model by a mix of the dynamic and logical modes.

Consider now how string operators $\tilde{O}_\alpha^{\tilde{C}_T}$ in the fermion model H_{FT} are mapped under the inverse unitary transformation $\mathcal{U}_T^\dagger$ to string operators $O_\alpha^{C_T}$ in the toric code H_{TC}. A σ^x operator on a single spin in the free model transforms to a string operator with one end point at the plaquette p corresponding to that spin and one at the plaquette that was mapped to the symmetry operator of the same colour as p. This will be b_1 if p is black and w_1 if p is white. This demonstrates how the symmetry operators ensure excitations are created in pairs in H_{FT}, as they are in the toric code.

A string operator with end points on any two plaquettes of the same colour in the toric code may be obtained by mapping from a product of two σ^x's at the spins corresponding to those plaquettes in H_{FT}. Consider the string operators $\tilde{O}_x^{\tilde{C}_T}$ and $\tilde{O}_z^{\tilde{C}_T}$ that map to string operators $O_x^{C_T}$ and $O_z^{C_T}$ with strings of σ^x's around a non-contractible loop of the torus i.e. those which cross the S_{z_1} and/or S_{z_2} operator. These operators contain $\tilde{S}_{x_1}$ and/or $\tilde{S}_{x_2}$, respectively. Those mapping to operators with strings of σ^z's around a non-contractible loop of the torus i.e. those which cross the S_{x_1} and/or S_{x_2} operator, contain $\tilde{S}_{z_1}$ and/or $\tilde{S}_{z_2}$, respectively. Any other string operator $O_x^{C_T}$ or $O_z^{C_T}$ with the same end points and effects on the logical qubits as those already mentioned are produced by the same method as those in the surface code, by including some combination of σ^z's in the operators $\tilde{O}_x^{\tilde{C}_T}$ or $\tilde{O}_z^{\tilde{C}_T}$. These σ^z's alter the string operator's path by including a loop around the corresponding plaquette to the path C_T.

Therefore, although the transformations $\mathcal{U}_S$ and $\mathcal{U}_T$ are local the statistics of both the surface and toric code are encoded by highly non-local interacting operators acting on the dynamic and logical modes of the resulting fermionic systems

4.5 Conclusions and Outlook

This chapter has shown that the $\mathbb{Z}_2$ surface and toric code are unitarily equivalent to free fermions and free fermions coupled to a fermionic parity constraint, respectively. Moreover, it presents the explicit form of unitary transformations $\mathcal{U}_S$ and $\mathcal{U}_T$ that map these codes to their fermionic counterparts for any system size. It was demonstrated that the anyonic statistical properties of the surface and toric code excitations map to the localised excitations of the fermionic models. The periodic boundary conditions of the toric code introduce the need for non-local interacting fermionic parity operators in the fermion model. Interestingly, although the energy spectra as well as any state of the codes can be reproduced with free fermions, in order to encode the exotic anyonic statistics of the models highly non-local interacting operators are required.

The ability to map the surface code to free fermions, could have a number of applications. For example, how the anyonic statistics of the excitations are

encoded by the unitary transformation allows for an intuitive and unique understanding of the origins of these statistics. Moreover, the construction and manipulation of free fermion systems are more efficient than current interacting descriptions of the surface code Bravyi *et al.* (2017). Extending the group of mappings, $\mathcal{U}$, to other topological models in two and higher dimensions, such as $\mathbb{Z}_{2^n}$ string-nets and Walker-Wang models, could provide valuable insight into the emergence of exotic statistics in these systems Meichanetzidis *et al.* (2018).

Chapter 5

Background 2: The Kitaev model and Riemann-Cartan Geometry

This chapter is split into two parts. The first part introduces the the Kitaev honeycomb model as presented by Kitaev Kitaev (2006). The second part outlines the components of $(2+1)-$dimensional Riemann-Cartan geometry. More comprehensive introductions are avaliable in Nakahara (2003), Carroll (2003); Reall (2017); Schutz (2009); Wald (1984). This chapter provide essential background knowledge for understanding the derivation of the effective geometric description of the low-energy limit of the Kitaev honeycomb model detailed in Chapter 6.

5.1 Kitaev's Honeycomb Model

This section introduces the Kitaev honeycomb model as presented by Kitaev Kitaev (2006) and gives the continuum limit approximation of the low energy limit of the model Pachos (2012). In Section 5.1.1 the model is presented in terms of spins on a honeycomb lattice. Section 5.1.2 then details Kitaev's fermionisation procedure redefining the spin model in terms of Majorana fermions. Section 5.1.3 discusses the interpretation of the model as a $\mathbb{Z}_2$ gauge theory coupled to Majorana fermions. Section 5.1.4 introduces the continuum limit approximation of the Kitaev honeycomb model. Section 5.1.5 explores the phase diagram of the Kitaev honeycomb model. Finally, Section 5.1.6 presents the calculation of the

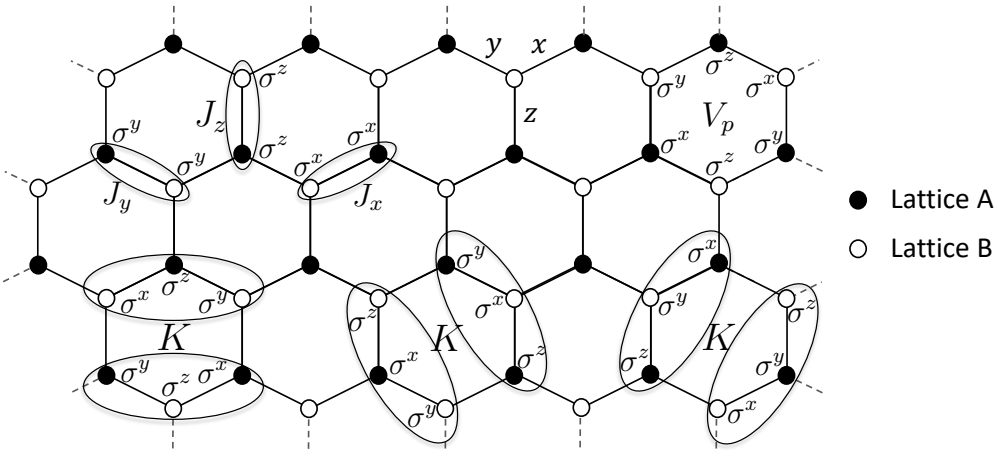

Figure 5.1: The Kitaev honeycomb model in terms of spins showing the three types of nearest neighbour two-body interactions with strength J_x, J_y and J_z. One of each possible configuration of three-body interactions with strength K, is depicted. The form of the local symmetry operator V_P is also shown.

two-point Majorana correlations, which will be studied in Section 6.2 in order to verify the geometric description of the model.

5.1.1 Spin Model

The Kitaev honeycomb model is an exactly solvable model of interacting spin-1/2 particles living on the vertices of a honeycomb lattice Kitaev (2006). The lattice is split into two triangular sub-lattices, A and B, as depicted in Fig 5.1 by full and empty circles respectively. Links are labelled x, y or z depending on their orientation. Spins interact via anisotropic nearest neighbour two-body terms, and three-body terms between nearest neighbour triplets. These interactions do not commute with each other, making the model difficult to solve. The Hamiltonian is

$$H = -4\left(J_x \sum_{(i,j)\in x} \sigma_i^x \sigma_j^x + J_y \sum_{(i,j)\in y} \sigma_i^y \sigma_j^y + J_z \sum_{(i,j)\in z} \sigma_i^z \sigma_j^z + K \sum_{(i,j,k)} \sigma_i^x \sigma_j^y \sigma_k^z\right), \tag{5.1}$$

where $(i,j) \in \alpha$ means we sum over all pairs of i and j that form an α link. As we can see from (5.1) these spins interact via a two-body term $\sigma_i^\alpha \sigma_j^\alpha$, as depicted in Fig. 5.1. The (i,j,k) sum runs over all triplets of neighbouring spins. If the pairs (i,j) and (j,k) are connected via α and γ links, respectively, the three-body terms are $\sigma_i^\alpha \sigma_j^\beta \sigma_k^\gamma$, where $\alpha \neq \beta \neq \gamma$. J_x, J_y and J_z are nearest neighbour coupling strengths and $|K| \ll J_\alpha$ $(\forall\ \alpha)$ sets the strength of the three-body terms. Note, In Eq. 5.1 we have introduced a factor of 4 compared to Ref. Kitaev (2006) in order to simplify the algebra in Chapters 5 and 6.

The three-body terms emerge as a perturbation due to the introduction of an external magnetic field Kitaev (2006). These terms explicitly break time-reversal symmetry allowing for topologically non-trivial behaviour as a non-zero Chern number $\nu \neq 0$ requires broken time-reversal symmetry Kitaev (2006); Pachos (2012). We can easily see this symmetry breaking by studying the behaviour of a single Pauil operator under a time-reversal transformation,

$$T \sigma_i^\mu T^\dagger = -\sigma_i^\mu \tag{5.2}$$

Therefore, any product of an odd (even) number of Pauli operators will break (respect) time-reversal symmetry.

Interestingly, all terms in the Hamiltonian (5.1) commute with the local symmetry operators $\hat{V}_p$ associated to plaquettes of the lattice, shown in Fig. 5.1,

$$\begin{aligned} \hat{V}_p &= (\sigma_1^y \sigma_2^y)(\sigma_2^z \sigma_3^z)(\sigma_3^x \sigma_4^x)(\sigma_4^y \sigma_5^y)(\sigma_5^z \sigma_6^z)(\sigma_6^x \sigma_1^x) \\ &= \sigma_1^z \sigma_2^x \sigma_3^y \sigma_4^z \sigma_5^x \sigma_6^y. \end{aligned} \tag{5.3}$$

These operators square to the identity, $\hat{V}_p^2 = \mathbb{I}$, so their eigenvalues are $V_p = \pm 1$. All $\hat{V}_p$ commute with each other as well as commuting with the Hamiltonian,

$$[\hat{V}_p, \hat{V}_q] = [\hat{V}_p, H] = 0. \tag{5.4}$$

These operators define conserved quantities (generators of the local symmetry), which makes solving the model much easier. The Hilbert space can be divided into sectors labelled by specific choices of eigenvalues $V_p = \pm 1$ for each plaquette p. We label these physical sectors w. There are $N/2$ plaquettes on a lattice of N sites, therefore, there are $2^{N/2}$ unique sectors each with dimensionality $2^{N/2}$. Thus

we are able to reduce the Hamiltonian to a specific sector and study the physics of each independently. This still has not solved the model, but we will see in the following sections how via Kitaev's fermionisation procedure the Hamiltonian for an individual sector becomes a Hamiltonian that is quadratic in terms of Majorana fermions, hence exactly solvable.

5.1.2 Majorana Fermionisation

The spin model presented in the previous section can be represented by Majorana fermion operators. This will result in a diagonalisable, quadratic Hamiltonian describing non-interacting fermions. Let us first define a Majorana fermion. A fermionic system with n modes can be described by complex fermion annihilation and creation operators, a_i and $a_i^\dagger$, where $i = 1, 2, ..., n$. These modes can be redefined in terms of Majorana operators,

$$c_{2i-1} = a_i + a_i^\dagger, \qquad c_{2i} = -i(a_i - a_i^\dagger). \tag{5.5}$$

Unlike complex fermions, these real fermions are their own anti-particle. They obey the following relations,

$$c_i = c_i^\dagger, \qquad c_i^2 = \mathbb{I}, \qquad \{c_i, c_j\} = 0 \tag{5.6}$$

Kitaev's fermionisation procedure uses four Majorana operators, c_i, b_i^x, b_i^y and b_i^z, to represent one spin-$\frac{1}{2}$. This is equivalent to using two complex fermions as each can be decomposed into two Majoranas. A single complex fermion and a spin-$\frac{1}{2}$ particle both have a Hilbert space of dimension two, so the Hilbert space of the four Majorana operators, $\mathcal{L}_i$, is twice as large as that of the spin they are supposed to represent. To rectify this we define half of the states to be in the *"physical"* subspace, $\mathcal{L}_i^p \subset \tilde{\mathcal{L}}_i$, and the other half in the *"unphysical"* subspace, $\mathcal{L}_i \subset \tilde{\mathcal{L}}_i$. We say that a state $|\Psi\rangle$ is in $\mathcal{L}_i^p$ if and only if,

$$D_i |\Psi\rangle = |\Psi\rangle, \qquad \text{where } D_i = b_i^x b_i^y b_i^z c_i. \tag{5.7}$$

We could have equivalently chosen all -1 eigenstates of D_i to be in the physical subspace. We can represent the Pauli operators σ_i^α by operators $\tilde{\sigma}_i^\alpha$ acting on the full space $\tilde{\mathcal{L}}_i$,

$$\tilde{\sigma}_i^\alpha = i b_i^\alpha c_i. \tag{5.8}$$

We are able to replace σ^α with $\tilde{\sigma}^\alpha$ as the physical subspace is closed under application of $\tilde{\sigma}^\alpha$, $[D_i, \tilde{\sigma}_i^\alpha] = 0$ for all α, and they obey the Pauli algebra when restricted to the physical subspace, $[\tilde{\sigma}_i^\alpha, \tilde{\sigma}_i^\beta] = i\epsilon^{\alpha\beta\gamma}\tilde{\sigma}^\alpha$, $(\tilde{\sigma}^\alpha)^2 = \mathbb{I}$ and $(\tilde{\sigma}^\alpha)^\dagger = \tilde{\sigma}^\alpha$.

We now restrict to the physical subspace $\mathcal{L}^p$ for every site and write the spin Hamiltonian (5.1) in terms of Majoranas,

$$H = i\sum_{i,j}\left(2J_{ij}\hat{u}_{ij} + 2K\sum_k \hat{u}_{ik}\hat{u}_{kj}\right)c_i c_j = i\sum_{i,j}\hat{A}_{ij}c_i c_j. \tag{5.9}$$

We have defined link operators,

$$\hat{u}_{ij} = ib_i^\alpha b_j^\alpha, \tag{5.10}$$

where α is determined by the orientation of the link connecting i and j. The $\hat{u}_{ij}$ are Hermitian, $\hat{u}_{ij}^\dagger = \hat{u}_{ij}$ and anti-symmetric, $\hat{u}_{ij} = -\hat{u}_{ji}$. They also square to the identity, $\hat{u}_{ij}^2 = \mathbb{I}$, so they have eigenvalues ± 1. A useful way to represent the patterns of $\hat{u}_{ij}$ eigenvalues is by drawing arrows between sites. The direction of the arrows determines the ordering of i, j that gives a $+1$ eigenvalue.

We can define the conserved quantities V_p of the model in terms of the eigenvalues u_{ij},

$$V_p = \prod_{(i,j)\in\partial p} u_{ij}, \tag{5.11}$$

where (i, j) are pairs of neighbouring sites and ∂p is the boundary of the plaquette p. Each pattern of V_p can be produced by many configurations of u_{ij}, labelled u. In the next section we will see how reducing the Hamiltonian to a specific physical sector w can be achieved by producing an equal weight superposition of all u in the corresponding equivalence class. We will also use the physical symmetries of the model to reduce further to a specific u and obtain a quadratic Hamiltonian from the highly interacting (5.9).

5.1.3 Vortices and Lattice Gauge Theory

Interestingly link operators $\hat{u}_{ij}$ commute with the Hamiltonian H, making them local symmetries of the model. We can split the full Hilbert space into spaces of states with specific configurations of eigenvalues u_{ij}, $\tilde{\mathcal{L}} = \bigoplus_u \mathcal{L}^u$. Fixing a u and

restricting to this space results in a quadratic fermionic Hamiltonian that can be easily solved. However, eigenstates of this Hamiltonian are not physical, they do not satisfy the equation (5.7), as $\hat{u}_{ij}$ and D_i do not commute, they anti-commute $\{\hat{u}_{ij}, D_i\} = 0$. Projecting a state $|\Psi_u\rangle$ of a particular configuration u to a physical state,

$$|\Psi_w\rangle = \mathcal{P}\,|\Psi_u\rangle \in \mathcal{L}^p, \qquad \mathcal{P} = \prod_i \frac{\mathbb{I} + D_i}{2} \tag{5.12}$$

produces a superposition of many different u's. However, the operators H and $\hat{V}_p$ do commute with D, hence are invariant under the projection $\mathcal{P}$. In fact the $|\Psi_w\rangle$ are uniquely characterised by their V_p configuration.

This means the model can be thought of as lattice gauge theory. The eigenvalues u_{ij} are a $\mathbb{Z}_2$ gauge field coupled to Majorana fermions and the D_i are local gauge transformations. The gauge invariant operators $\hat{V}_p$ are the Wilson loops operators and an eigenvalue of $V_p = -1$ can be thought of as a π-flux or vortex on the plaquette p. We call different configurations of V_p vortex sectors. A useful way to visualise the gauge field is by viewing negative eigenvalues of link operators $u_{ij} = -1$ as an unphysical strings passing perpendicularly through the link. Open ends of these strings correspond to plaquettes with $V_p = -1$. Applying a local gauge transformation D_i to a site flips the three surrounding u_{ij}. This is equivalent to producing a closed loop or deforming a string about a vertex. This does not change the end points of the strings, so does not change the vortex sector. The state $|\Psi_w\rangle$ is then a superposition of all possible loop and string configurations u in the same vortex sector w.

We are able to restrict to a particular vortex sector by picking a specific configuration u. We can then solve the resultant quadratic Hamiltonian. Although the states $|\Psi_u\rangle$ are not physical we are allowed to do this as long as all observables we are interested in studying are gauge invariant, i.e. they are invariant under projection $\mathcal{P}$ to the physical subspace $\mathcal{L}^p$. The quadratic Hamiltonian has the form

$$H = i \sum_{i,j} \left(2J_{ij} u_{ij} + 2K \sum_k u_{ik} u_{kj} \right) c_i c_j = i \sum_{i,j} A_{ij} c_i c_j, \tag{5.13}$$

where the J_{ij} term describes interactions between c Majoranas on nearest neighbour sites i, j and the K term describes next to nearest neighbour interactions

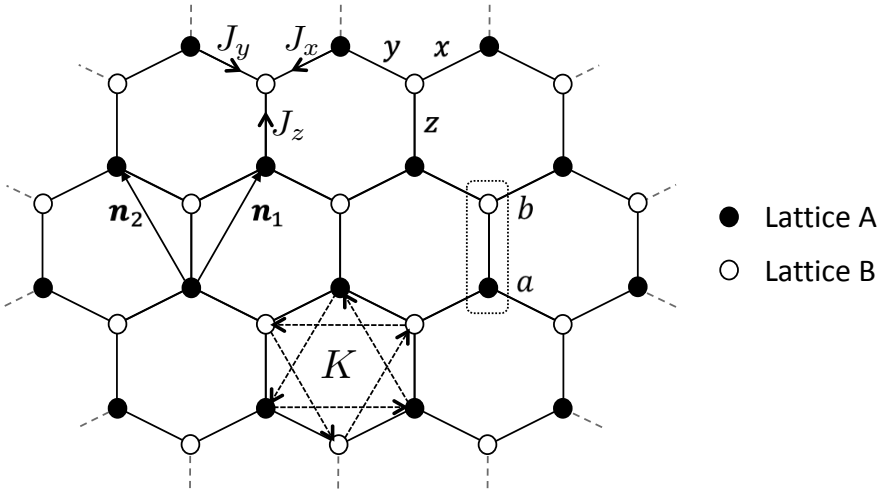

Figure 5.2: The Kitaev honeycomb model in terms of Majorana fermions. Majorana fermions tunnel between nearest neighbouring sites with couplings J_x, J_y and J_z depending on the direction of the link. Tunnelling between next-to-nearest neighbouring sites with coupling K is also indicated. The honeycomb lattice comprises two triangular sub-lattices, A and B, denoted by full and empty circles, respectively. The unit cell is taken along the z-links. The translation vectors between sites of the same sub-lattices are $\boldsymbol{n}_1 = (\frac{\sqrt{3}}{2}, \frac{3}{2})$ and $\boldsymbol{n}_2 = (-\frac{\sqrt{3}}{2}, \frac{3}{2})$. The orientations of nearest neighbour tunnellings (from A to B sites) and next-to-nearest neighbour tunnellings (anticlockwise) are indicated.

between sites i, j connected by k, these are shown in Fig. 5.2. In order to solve this model we need only diagonalise the antisymmetric $L \times L$ matrix A_{ij}, where L is the linear system size. The matrix A_{ij} grows polynomially with system size as opposed to the exponential growth of the spin Hamiltonian.

For the rest of Section 5.1 we will restrict to the no-vortex sector, the sector with $V_p = +1$ for all p.

5.1.4 Continuum Limit

This section presents the continuum limit, or low energy limit, of the Kitaev honeycomb model with isotropic, homogeneous couplings, i.e. $J_x = J_y = J_z = J$ and $\partial_\mu J = \partial_\mu K = 0$ with $\mu \in (t, x, y)$. The notation set up in this section will be used

in Chapter 6. Consider the no-vortex sector, which contains the lowest energy states of the model Lieb (1994). Specifically restrict to the trivial u configuration, where $u_{ij} = +1$ for all links oriented from sub-lattice A to B, as shown in Fig. 5.2 for an x, y and z link. Similar to graphene Castro Neto *et al.* (2009); DiVincenzo & Mele (1984); Semenoff (1984) this model has a continuum limit given in terms of a Dirac Hamiltonian with a linear energy-momentum dispersion relation. To see this we consider the low energy limit of the model where long wavelengths are dominant, lattice spacing is negligible and the continuum limit approximation is most applicable. In this low energy regime the Kitaev model can be effectively described by by a quantum field theory of relativistic Majorana fermions.

Chapter 6 presents a description of the low energy limit of the generally anisotropic, inhomogeneous Kitaev honeycomb model in terms of massless Majorana spinors obeying the Dirac equation embedded in a $(2+1)-$dimensional Riemann-Cartan spacetime which is locally Lorentz invariant. This differs to the Dirac equation of the isotropic, homogeneous case presented here which is embedded in flat $(2+1)-$dimensional Minkowski spacetime. However, the initial part of the continuum limit calculation is identical for both coupling regimes and will be referred back to in Chapter 6. For now restrict to the isotropic case when studying the low energy behaviour of the model.

The Hamiltonian (5.13) can be split into two parts,

$$H = H_1 + H_2. \tag{5.14}$$

H_1 contains the nearest neighbour interactions,

$$H_1 = i \sum_{i,j} 2J_{ij} u_{ij} c_i c_j, \tag{5.15}$$

and H_2 contains the next to nearest neighbour interactions,

$$H_2 = i \sum_{i,j} 2K \sum_{k} u_{ik} u_{kj} c_i c_j. \tag{5.16}$$

The Honeycomb lattice contains two triangular sub-latices A and B, represented in Fig 5.2 by black and white dots respectively. The vectors $\boldsymbol{n}_1 = (\frac{\sqrt{3}}{2}, \frac{3}{2})$ and $\boldsymbol{n}_2 = (-\frac{\sqrt{3}}{2}, \frac{3}{2})$ generate the sub-lattices A and B. The unit cell of the lattice

contains two sites. We take them to be two sites connected by a z link, also shown in Fig 5.2. We label two Majorana operators in the same unit cell by $c^a_{\boldsymbol{r}}$ and $c^b_{\boldsymbol{r}}$, where the superscript determines which sub-lattice they act on and the subscript describes the real space position of the unit cell. Note that the introduction of vortices changes the unit cell of the lattice. The following calculations can be easily reworked by redefining the unit cell of the lattice if vortices are introduced in a regular, periodic fashion. Here we focus only on the no-vortex sector.

Diagonalising H_1

We can rewrite the nearest neighbour interactions as,

$$H_1 = i\sum_{\boldsymbol{r}} 2c^b_{\boldsymbol{r}}(J_x c^a_{\boldsymbol{r}+\boldsymbol{n}_1} + J_y c^a_{\boldsymbol{r}+\boldsymbol{n}_2} + J_z c^a_{\boldsymbol{r}}) + \text{h.c.}, \tag{5.17}$$

where $\boldsymbol{r}$ sums over all unit cells in the lattice. We diagonalise the Hamiltonian by Fourier transforming,

$$c^{a/b}_{\boldsymbol{r}} = \sum_{\boldsymbol{q}} e^{-i\boldsymbol{q}\cdot\boldsymbol{r}} c^{a/b}_{\boldsymbol{q}} \tag{5.18}$$

Substituting (5.18) into (5.17) gives,

$$\begin{aligned} H_1 &= i\sum_{\boldsymbol{p},\boldsymbol{q}}\sum_{\boldsymbol{r}} 2e^{-i(\boldsymbol{p}+\boldsymbol{q})\cdot\boldsymbol{r}}\left(J_x e^{-i\boldsymbol{p}\cdot\boldsymbol{n}_1} + J_y e^{-i\boldsymbol{p}\cdot\boldsymbol{n}_2} + J_z\right) c^b_{\boldsymbol{q}} c^a_{\boldsymbol{q}} + \text{h.c.} \\ &= i\sum_{\boldsymbol{q}} 2(J_x e^{i\boldsymbol{q}\cdot\boldsymbol{n}_1} + J_y e^{i\boldsymbol{q}\cdot\boldsymbol{n}_2} + J_z) c^b_{\boldsymbol{q}} c^a_{-\boldsymbol{q}} + \text{h.c.} \end{aligned} \tag{5.19}$$

From (5.18) we see that $c_{-\boldsymbol{q}} = c^\dagger_{\boldsymbol{q}}$. Then,

$$H_1 = \sum_{\boldsymbol{q}} (-if(\boldsymbol{q}) c^{a\dagger}_{\boldsymbol{q}} c^b_{\boldsymbol{q}} + if^*(\boldsymbol{q}) c^{b\dagger}_{\boldsymbol{q}} c^a_{\boldsymbol{q}}), \tag{5.20}$$

where,

$$f(\boldsymbol{q}) = 2(J_x e^{i\boldsymbol{q}\cdot\boldsymbol{n}_1} + J_y e^{i\boldsymbol{q}\cdot\boldsymbol{n}_2} + J_z). \tag{5.21}$$

Diagonalising H_2

The next to nearest neighbour interactions become,

$$H_2 = iK\sum_{\boldsymbol{r}} c^a_{\boldsymbol{r}}(-c^a_{\boldsymbol{r}+\boldsymbol{n}_1} + c^a_{\boldsymbol{r}+\boldsymbol{n}_2} + c^a_{\boldsymbol{r}+\boldsymbol{n}_1-\boldsymbol{n}_2}) + c^b_{\boldsymbol{r}}(c^b_{\boldsymbol{r}+\boldsymbol{n}_1} - c^b_{\boldsymbol{r}+\boldsymbol{n}_2} - c^b_{\boldsymbol{r}+\boldsymbol{n}_1-\boldsymbol{n}_2}) + \text{h.c.} \tag{5.22}$$

We Fourier transform again to produce

$$\begin{aligned} H_2 &= iK \sum_{\boldsymbol{p},\boldsymbol{q}} \sum_{\boldsymbol{r}} e^{-i(\boldsymbol{p}+\boldsymbol{q})\cdot\boldsymbol{r}} \left[-e^{-i\boldsymbol{p}\cdot\boldsymbol{n}_1} + e^{-i\boldsymbol{p}\cdot\boldsymbol{n}_2} + e^{-i\boldsymbol{p}\cdot(\boldsymbol{n}_1-\boldsymbol{n}_2)}\right] (c^a_{\boldsymbol{q}} c^a_{\boldsymbol{p}} - c^b_{\boldsymbol{q}} c^b_{\boldsymbol{p}}) + \text{h.c} \\ &= 2K \sum_{\boldsymbol{q}} \left[-\sin(\boldsymbol{q}\cdot\boldsymbol{n}_1) + \sin(\boldsymbol{q}\cdot\boldsymbol{n}_2) + \sin(\boldsymbol{q}\cdot(\boldsymbol{n}_1-\boldsymbol{n}_2))\right] (c^{a\dagger}_{\boldsymbol{q}} c^a_{\boldsymbol{q}} - c^{b\dagger}_{\boldsymbol{q}} c^b_{\boldsymbol{q}}). \end{aligned} \tag{5.23}$$

Therefore we have

$$H_2 = \sum_{\boldsymbol{q}} \Delta(\boldsymbol{q}) (c^{a\dagger}_{\boldsymbol{q}} c^a_{\boldsymbol{q}} - c^{b\dagger}_{\boldsymbol{q}} c^b_{\boldsymbol{q}}) \tag{5.24}$$

where

$$\Delta(\boldsymbol{q}) = 2K[-\sin(\boldsymbol{q}\cdot\boldsymbol{n}_1) + \sin(\boldsymbol{q}\cdot\boldsymbol{n}_2) + \sin(\boldsymbol{q}\cdot(\boldsymbol{n}_1-\boldsymbol{n}_2))]. \tag{5.25}$$

Total Hamiltonian $H = H_1 + H_2$

If we define the two-component spinor $\psi_{\boldsymbol{q}} = (c^a_{\boldsymbol{q}}\ ic^b_{\boldsymbol{q}})^{\mathrm{T}}$, then the Hamiltonian (5.14) becomes

$$H = H_1 + H_2 = \sum_{\boldsymbol{q}} \psi^\dagger_{\boldsymbol{q}} h(\boldsymbol{q}) \psi_{\boldsymbol{q}}, \tag{5.26}$$

with the single particle Hamiltonian $h(\boldsymbol{q})$ given by,

$$h(\boldsymbol{q}) = \begin{pmatrix} \Delta(\boldsymbol{q}) & -f(\boldsymbol{q}) \\ -f^*(\boldsymbol{q}) & -\Delta(\boldsymbol{q}) \end{pmatrix} \tag{5.27}$$

Eigenvalues of the single-particle Hamiltonian are given by

$$E(\boldsymbol{q}) = \pm\sqrt{\Delta^2(\boldsymbol{q}) + |f(\boldsymbol{q})|^2}. \tag{5.28}$$

Taylor expanding about the Fermi points

In the low energy limit wavelengths increase, lattice spacing becomes negligible and we may use the continuum limit approximation. The points in the Brillouin zone for which energy $E(\boldsymbol{q})$ is a minimum are the Fermi points. The spectrum for $K = 0$ is plotted in Fig. 5.3. We see that the system has two independent Fermi points $\boldsymbol{P}_\pm$. We will produce a continuum limit approximation of the low-energy behaviour of the model by substituting $\boldsymbol{q} = \boldsymbol{P}_\pm + \boldsymbol{p}$ for small $\boldsymbol{p}$ and Taylor

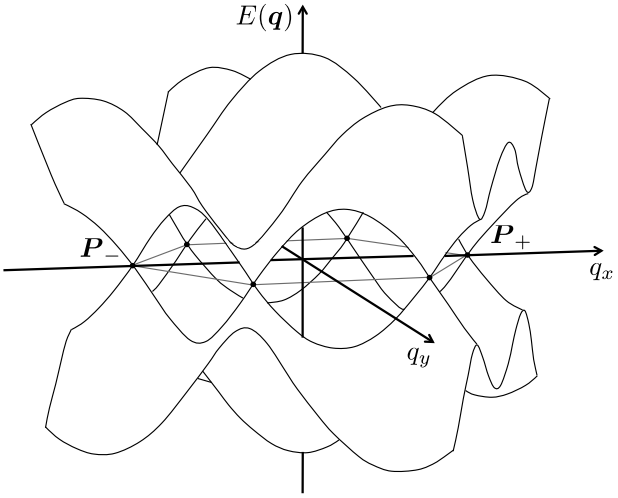

Figure 5.3: The dispersion relation $E(\boldsymbol{q})$ for the honeycomb Hamiltonian when $J_x = J_y = J_z = J$ and $K = 0$. The Fermi points are the points where $E(\boldsymbol{q}) = 0$. The two inequivalent Fermi points within the Brillouin zone are given by $\boldsymbol{P}_+$ and $\boldsymbol{P}_-$.

expanding $h(\boldsymbol{q})$ in (5.27) around the Fermi points up to first order in $\boldsymbol{p}$. For convenience we define the Hamiltonians $h_\pm(\boldsymbol{p}) \equiv h(\boldsymbol{P}_\pm + \boldsymbol{p})$. We now restrict to the isotropic coupling regime, where $J_x = J_y = J_z = J$. Chapter 6 explores the anisotropic case.

Let us first find the Fermi points of the system with $K = 0$. In this case $E(\boldsymbol{q}) = \pm|f(\boldsymbol{q})|$. This is at a minimum when

$$f(\boldsymbol{q}) = 2J(e^{i\boldsymbol{q}\cdot\boldsymbol{n}_1} + e^{i\boldsymbol{q}\cdot\boldsymbol{n}_2} + 1) = 0, \tag{5.29}$$

giving the equations

$$\cos(\boldsymbol{q}\cdot\boldsymbol{n}_1) + \cos(\boldsymbol{q}\cdot\boldsymbol{n}_2) + 1 = 0 \tag{5.30}$$

$$\sin(\boldsymbol{q}\cdot\boldsymbol{n}_1) + \sin(\boldsymbol{q}\cdot\boldsymbol{n}_2) = 0, \tag{5.31}$$

which have two solutions

$$\boldsymbol{P}_\pm = \pm\left(\frac{4\pi}{3\sqrt{3}}, 0\right). \tag{5.32}$$

Taylor expanding (5.21) about $\boldsymbol{P}_\pm$, remembering that $f(\boldsymbol{P}_\pm) = 0$, gives

$$f(\boldsymbol{P}_\pm + \boldsymbol{p}) = \nabla f(\boldsymbol{P}_\pm)\cdot p = -3J(\pm p_x + ip_y) + O(\boldsymbol{p}^2). \tag{5.33}$$

Now let us take $K \neq 0$ and expand (5.25) about $\boldsymbol{P}_\pm$. As $\nabla(\Delta(\boldsymbol{P}_\pm))$ vanishes at $\boldsymbol{P}_\pm$ we are left with,

$$\Delta(\boldsymbol{P}_\pm + \boldsymbol{p}) = \Delta(\boldsymbol{P}_\pm) = \mp 3\sqrt{3}K + O(\boldsymbol{p}^2). \tag{5.34}$$

This has no linear momentum contribution, so does not change the Fermi point. It does shift the energy of the Fermi point and produces a gap $\Delta = 3\sqrt{3}K$ in the dispersion.

Using (5.33) and (5.34) we can expand the single particle Hamiltonian (5.27) to give

$$\begin{aligned} h_\pm(\boldsymbol{p}) \equiv h(\boldsymbol{P}_\pm + \boldsymbol{p}) &= \begin{pmatrix} \Delta(\boldsymbol{P}_\pm + \boldsymbol{p}) & -f(\boldsymbol{P}_\pm + \boldsymbol{p}) \\ -f^*(\boldsymbol{P}_\pm + \boldsymbol{p}) & -\Delta(\boldsymbol{P}_\pm + \boldsymbol{p}) \end{pmatrix} \\ &= \begin{pmatrix} \mp 3\sqrt{3}K & 3J(\pm p_x + i p_y) \\ 3J(\pm p_x - i p_y) & \pm 3\sqrt{3}K \end{pmatrix} + O(\boldsymbol{p}^2) \end{aligned} \tag{5.35}$$

or equivalently

$$h_\pm(\boldsymbol{p}) = 3J\big(\pm \sigma^x p_x - \sigma^y p_y\big) \mp 3\sqrt{3}K\sigma^z + O(\boldsymbol{p}^2), \tag{5.36}$$

which acts on the spinors $\psi_+ = (c_+^a \; i c_+^b)^T$ and $\psi_- = (c_-^a \; i c_-^b)^T$, respectively, where $c_\pm^{a/b} = c_{\boldsymbol{P}_\pm}^{a/b}$.

Weyl (chiral) basis

Now consider the two Hamiltonians $h(\boldsymbol{p})_+$ and $h(\boldsymbol{p})_-$ simultaneously. The two Fermi points can be treated as pseudo-spin or chiral degrees of freedom by defining a Dirac-like spinor

$$\Psi_{\boldsymbol{p}} = \begin{pmatrix} c_+^a \\ i c_+^b \\ i c_-^b \\ c_-^a \end{pmatrix}, \quad \Psi_{\boldsymbol{p}}^\dagger = (c_+^{a\dagger} \; -i c_+^{b\dagger} \; -i c_-^{b\dagger} \; c_-^{a\dagger}). \tag{5.37}$$

Taking the direct sum of $h(\boldsymbol{p})_+$ and $h(\boldsymbol{p})_-$ in their respective bases defined by (5.37) gives the complete 4×4 Hamiltonian

$$h_{\text{total}}(\boldsymbol{p}) = 3J(\sigma^z \otimes \sigma^x p_x - \sigma^z \otimes \sigma^y p_y) - 3\sqrt{3}K\mathbb{I}_2 \otimes \sigma^z, \tag{5.38}$$

where $\mathbb{I}_d$ is the d dimensional identity matrix. Note that a σ^x rotation is applied to $h_-(\boldsymbol{p})$ before direct summing with $h_+(\boldsymbol{p})$.

The low energy limit Hamiltonian (5.38) takes the form of a Dirac operator with Dirac $\boldsymbol{\alpha}$ and β matrices

$$\boldsymbol{\alpha} = \begin{pmatrix} \boldsymbol{\sigma} & 0 \\ 0 & -\boldsymbol{\sigma} \end{pmatrix} = \sigma^z \otimes \boldsymbol{\sigma}, \quad \beta = \begin{pmatrix} 0 & \mathbb{I}_2 \\ \mathbb{I}_2 & 0 \end{pmatrix} = \sigma^x \otimes \mathbb{I}_2, \tag{5.39}$$

where $\boldsymbol{\sigma} = (\sigma^x, \sigma^y, \sigma^z)$ are the Pauli matrices. The corresponding gamma matrices are defined by $\gamma^0 = \beta$ and $\boldsymbol{\gamma} = \beta^{-1}\boldsymbol{\alpha}$

$$\boldsymbol{\gamma} = \begin{pmatrix} 0 & -\boldsymbol{\sigma} \\ \boldsymbol{\sigma} & 0 \end{pmatrix} = -i\sigma^y \otimes \boldsymbol{\sigma} \tag{5.40}$$

These gamma matrices satisfy the flat space Clifford algebra $\{\gamma^a, \gamma^b\} = 2\eta^{ab}$, where the Latin indices $a, b, ... \in (0, 1, 2, 3)$ and $\eta^{ab} = \text{diag}(1, -1, -1, -1)$ is the $(3+1)-$dimensional Minkowski metric. Although the Kitaev model is $(2+1)-$dimensional, we have a four dimensional representation of the gamma matrices so are able to define an extra matrix γ^3. The fifth gamma matrix is then given by

$$\begin{aligned} \gamma^5 &= -i\alpha^1\alpha^2\alpha^3 \\ &= i\gamma^0\gamma^1\gamma^2\gamma^3 \\ &= \sigma^z \otimes \mathbb{I}_2. \end{aligned} \tag{5.41}$$

Note that $(\gamma^5)^2 = \mathbb{I}_4$.

The charge conjugate of a Dirac spinor Ψ is defined by $\Psi^{(c)} = C\Psi^*$, where C is the charge conjugation operator C defined as a matrix which satisfies $C^\dagger C = \mathbb{I}$ and $C^\dagger \gamma^a C = -(\gamma^a)^*$ for all a. In the Weyl or chiral basis of gamma matrices (5.40) the charge conjugation matrix is given by

$$C = -\sigma^y \otimes \sigma^y = i \begin{pmatrix} 0 & \sigma^y \\ -\sigma^y & 0 \end{pmatrix}. \tag{5.42}$$

This clearly satisfies the condition $C^\dagger C = \mathbb{I}$. It also satisfies the second condition for γ^i with $i \in (1, 2, 3)$

$$\begin{aligned} C^\dagger \gamma^i C &= (-\sigma^y \otimes \sigma^y)^\dagger (-i\sigma^y \otimes \sigma^i)(-\sigma^y \otimes \sigma^y) \\ &= -i\sigma^y\sigma^y\sigma^y \otimes \sigma^y\sigma^i\sigma^y \\ &= -(-i\sigma^y \otimes \sigma^i)^* \\ &= -(\gamma^i)^*, \end{aligned} \tag{5.43}$$

where we have used the fact that $\sigma^y\sigma^i\sigma^y = -(\sigma^i)^*$. Similarly for γ^0

$$\begin{aligned} C^\dagger\gamma^i C &= (-\sigma^y\otimes\sigma^y)^\dagger(\sigma^x\otimes\mathbb{I}_2)(-\sigma^y\otimes\sigma^y) \\ &= \sigma^y\sigma^x\sigma^y\otimes\sigma^y\sigma^y \\ &= -(\sigma^x\otimes\mathbb{I}_2)^* \\ &= -(\gamma^0)^*. \end{aligned} \tag{5.44}$$

To prove that the spinor $\Psi_{\boldsymbol{p}}$ in (5.37) is a Majorana spinor we must show that it satisfies the neutrality condition $\Psi^{(c)}_{\boldsymbol{p}} = \Psi_{\boldsymbol{p}}$. The charge conjugation matrix (5.42) is given explicitly in the Weyl basis as

$$C = \begin{pmatrix} 0 & 0 & 0 & 1 \\ 0 & 0 & -1 & 0 \\ 0 & -1 & 0 & 0 \\ 1 & 0 & 0 & 0 \end{pmatrix} \tag{5.45}$$

The fourier transformation of a Majorana mode (5.18) implies that $(c^{a/b}_p)^* = c^{a/b}_{-p}$, so

$$\Psi^{(c)} = \begin{pmatrix} 0 & 0 & 0 & 1 \\ 0 & 0 & -1 & 0 \\ 0 & -1 & 0 & 0 \\ 1 & 0 & 0 & 0 \end{pmatrix} \begin{pmatrix} c^a_+ \\ ic^b_+ \\ ic^b_- \\ c^a_- \end{pmatrix}^* = \begin{pmatrix} c^a_+ \\ ic^b_+ \\ ic^b_- \\ c^a_- \end{pmatrix} = \Psi. \tag{5.46}$$

Hence, the spinor (5.37) is indeed a Majorana spinor.

Using the gamma matrices (5.40) the total Hamiltonian (5.38) becomes

$$h_{\text{total}}(\boldsymbol{p}) = 3J(\gamma^0\gamma^1 p_x - \gamma^0\gamma^2 p_y) - i3\sqrt{3}K\gamma^1\gamma^2. \tag{5.47}$$

Note (5.47) is independent of the choice of β, it is completely fixed by α^1 and α^2.

The low energy limit many-body Hamiltonian is then given by

$$H_{\text{total}} = \int \mathrm{d}^2p\,\Psi^\dagger_{\boldsymbol{p}} h(\boldsymbol{p})_{\text{total}}\Psi_{\boldsymbol{p}}. \tag{5.48}$$

Therefore, the low energy limit of the isotropic Kitaev honeycomb model is given by Majorana spinors (5.37) obeying a Dirac equation (5.47) embedded in flat $(2+1)-$dimensional Minkowski spacetime. This Dirac Hamiltonian has a linear energy dispersion relation, much like graphene, and a K-term that gives rise to an energy gap at the Fermi points. It is shown in Chapter 6 that the K-term is proportional to the completely anti-symmetric part of the torsion tensor in $2+1$ dimensions. Hence, a non-zero K couples the Majorana spinors (5.37) to a non-trivial torsion field.

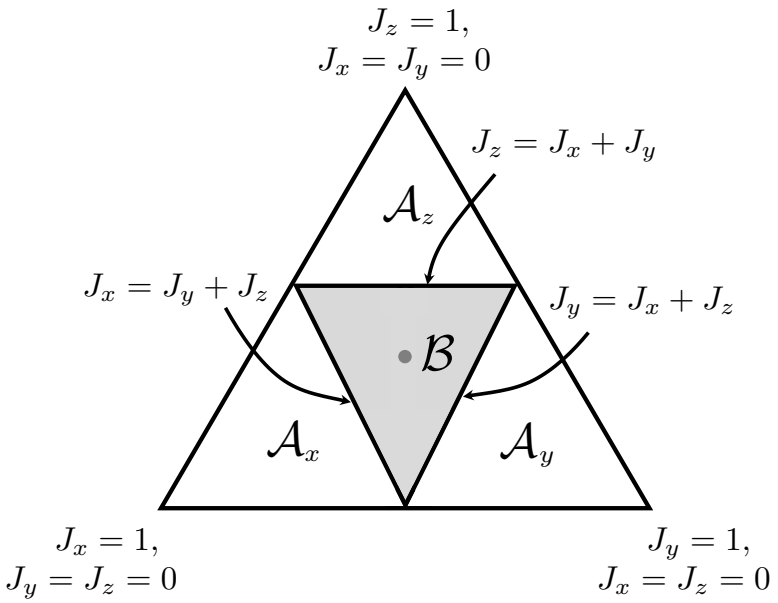

Figure 5.4: The phase diagram of the anisotropic KHLM, where the couplings are normalised as $J_x + J_y + J_z = 1$. The isotropic case with $J_x = J_y = J_z$ is denoted by a dot in the centre of the triangles. The quantum spin liquid topological phase that supports Majorana fermions, denoted as $\mathcal{B}$, sits in the centre of the diagram. The topological phases $\mathcal{A}_i$ correspond to the Toric Code phase. The boundaries between the $\mathcal{A}_i$ and $\mathcal{B}$ phases are defined by (5.49).

5.1.5 Phases and Anyonic Excitations

This section explores the phase diagram of the Kitaev honeycomb model. For certain values of the couplings $\{J_i\}$ and K, the ground state of the Kitaev honeycomb model exhibits topological order due to long-range entanglement Lahtinen & Pachos (2009b, 2010); Lahtinen *et al.* (2012), which can lead to excitations that behave as Abelian or non-Abelian anyons Kitaev (2006). Consider the model with $K = 0$. It is clear from (5.21) and (5.28) that the model is only gapless if $J_x e^{i\boldsymbol{q}\cdot\boldsymbol{n}_1} + J_y e^{i\boldsymbol{q}\cdot\boldsymbol{n}_2} + J_z = 0$ for some $\boldsymbol{q}$. This has solutions when

$$|J_x| \leq |J_y| + |J_z|, \quad |J_y| \leq |J_z| + |J_x|, \quad |J_z| \leq |J_x| + |J_y|. \tag{5.49}$$

Fig. 5.4 shows the phase diagram of the no-vortex sector of the Kitaev honeycomb model, where $J_i \geq 0$ and $J_x + J_y + J_z = 1$. The central $\mathcal{B}$ phase in Fig. 5.4

is the gapless quantum spin liquid topological phase Balents (2010); Knolle & Moessner (2019); Savary & Balents (2017) defined by (5.49). Taking $K \neq 0$ opens a gap in the spectrum. The model in this phase is a p+ip superconductor in the D class with a non-trivial Chern number $\nu = 1$ Chiu *et al.* (2016). In the $\mathcal{B}$ phase sufficiently separated vortices, of the type discussed in Section 5.1.3, bind Majorana zero modes Dusuel *et al.* (2008); Kitaev (2003); Otten *et al.* (2019); Schmidt *et al.* (2008); **?**. These Majoranas behave like Ising anyons σ Lahtinen & Pachos (2009b) sharing the same anyonic statistics as the excitations of the $SU(2)_2$ string-net Bonderson (2007).

The $\mathcal{A}_i$ phases in Fig. 5.4 are gapped phases with Chern number $\nu = 0$ Kitaev (2006). The phase transitions between the $\mathcal{B}$ and $\mathcal{A}_i$ phases are defined by the boundaries of the region (5.49). For example, the transition between the $\mathcal{B}$ and $\mathcal{A}_x$ phase is defined by $J_x = J_y + J_z$. Due to the rotational symmetry of the lattice the three $\mathcal{A}_i$ phases are the same up to some permutation of the x, y, and z links. The $\mathcal{A}_i$ phases of the Kitaev honeycomb model are actually equivalent to the toric code Kitaev (2006), reviewed in Section 2.2. Vortices in these phases behave like the Abelian e and m anyons of the toric code.

5.1.6 Two-Point Majorana Correlations

The two-point Majorana correlations are the expectation values $\langle c_i c_j \rangle = \mathrm{tr}(\rho c_i c_j)$ of Majorana operators at different lattice sites. The Majorana correlation matrix can be easily found through exact diagonalisation of the Kitaev honeycomb Hamiltonian (5.13) given here for convenience

$$H = i \sum_{i,j=1}^{N} A_{ij} c_i c_j, \tag{5.50}$$

where N is the number of sites in the lattice. This section presents the calculation. A_{ij} is an anti-symmetric matrix with purely imaginary eigenvalues that occur in positive/negative pairs, $\pm i\epsilon_k$. Therefore, A_{ij} can be diagonalised with complex

matrices as follows,

$$\begin{aligned} A &= UDU^\dagger \\ &= \begin{pmatrix} \mathbf{u}_1 \\ \mathbf{u}_1^* \\ \mathbf{u}_2 \\ \mathbf{u}_2^* \\ \vdots \end{pmatrix}^T \begin{pmatrix} i\epsilon_1 & 0 & 0 & 0 & \dots \\ 0 & -i\epsilon_1 & 0 & 0 & \dots \\ 0 & 0 & i\epsilon_2 & 0 & \dots \\ 0 & 0 & 0 & -i\epsilon_2 & \dots \\ \vdots & \vdots & \vdots & \vdots & \ddots \end{pmatrix} \begin{pmatrix} (\mathbf{u}_1)^\dagger \\ (\mathbf{u}_1^*)^\dagger \\ (\mathbf{u}_2)^\dagger \\ (\mathbf{u}_2^*)^\dagger \\ \vdots \end{pmatrix}, \end{aligned} \tag{5.51}$$

where U is a unitary matrix. The Hamiltonian then becomes

$$H = \frac{1}{4}\mathbf{c}^T(iA)\mathbf{c} = \frac{1}{4}\mathbf{c}^T U(iD)U^\dagger \mathbf{c}, \tag{5.52}$$

where $\mathbf{c}$ is a column vector of Majorana operators. This gives the complex fermion representation of the normal modes, $\mathbf{g} = \frac{1}{\sqrt{2}}U^\dagger \mathbf{c}$,

$$\begin{pmatrix} g_1^\dagger \\ g_1 \\ \vdots \end{pmatrix} = \frac{1}{\sqrt{2}} U^\dagger \begin{pmatrix} c_1 \\ c_2 \\ \vdots \end{pmatrix}. \tag{5.53}$$

Using (5.52) and (5.53) the Hamiltonian (5.50) can be rewritten as,

$$H = \sum_{k=1}^{N/2} \epsilon_k \left(g_k^\dagger g_k - \frac{1}{2} \right) \tag{5.54}$$

Taking the outer product of $\mathbf{c}$ with $\mathbf{c}^T$ gives a matrix of correlation operators. Using (5.53) gives

$$\begin{pmatrix} c_1c_1 & c_1c_2 & \dots \\ c_2c_1 & c_2c_2 & \dots \\ \vdots & \vdots & \ddots \end{pmatrix} = 2U \begin{pmatrix} g_1^\dagger g_1 & 0 & \dots \\ 0 & g_1 g_1^\dagger & \dots \\ \vdots & \vdots & \ddots \end{pmatrix} U^\dagger. \tag{5.55}$$

The right hand side of this equation becomes a linear sum of elements of $\mathbf{g}\mathbf{g}^\dagger$. As the expectation value of a linear sum of operators is equal to the linear sum of the expectation values, each element in $\mathbf{g}\mathbf{g}^\dagger$ can be replaced by its expectation value,

$$\begin{pmatrix} 1 & \langle c_1c_2 \rangle & \dots \\ \langle c_2c_1 \rangle & 1 & \dots \\ \vdots & \vdots & \ddots \end{pmatrix} = 2U \begin{pmatrix} \langle g_1^\dagger g_1 \rangle & 0 & \dots \\ 0 & \langle g_1 g_1^\dagger \rangle & \dots \\ \vdots & \vdots & \ddots \end{pmatrix} U^\dagger. \tag{5.56}$$

The expectation value $\langle g_i^\dagger g_j \rangle$ at zero temperature is then given by the Fermi-Dirac distribution with a Fermi energy of zero. This result is used in Section 6.2.2 to analyse the behaviour of the Majorana correlations for different coupling regimes of Kitaev's honeycomb model in order to verify the accuracy of the effective geometric description of the model.

5.2 Riemann-Cartan Spacetime in $2+1$ Dimensions

Section 5.1 shows the continuum limit of the Kitaev honeycomb lattice model is described by Majorana spinors obeying a Dirac Hamiltonian on a flat $(2+1)-$dimensional Minkowski spacetime. This section considers Majorana spinors on a curved spacetime. The notation introduced in this section will be used in Chapter 6. The first half of the section introduces the tools needed to transform from a flat space to a curved space. Specifically, Section 5.2.1 introduces the dreibein and metric and Section 5.2.2 discusses the covariant derivative, the connection of a spacetime and the contorsion tensor. Section 5.2.3 then considers the idea of parallel transport and how this pertains to the curvature and torsion of a spacetime. Curved spacetimes that support torsion are of particular interest, as in Chapter 6 it will be shown that the K term in the Kitaev honeycomb model couples the majorana spinors to a non-trivial torsion. Such spacetimes are called Riemann-Cartan spacetimes Carroll (2003); Nakahara (2003); Reall (2017). Finally, Section 5.2.4 presents the form of the Dirac action and Hamiltonian of spinors on a $(2+1)-$dimensional Riemann-Cartan spacetime. The form of the Hamiltonian is specific to a static spacetime Schutz (2009); Wald (1984).

5.2.1 Dreibein and Metric

Consider a $(2+1)-$dimensional spacetime (M, g) with coordinate system (t, x, y). M is a differentiable manifold and g is a metric tensor. At every point p in M we have a *tangent space* which is the space of vectors tangent to functions in M passing through the point p. The *coordinate basis vectors* $\{e_\mu = \partial_\mu\}$ of a tangent space give the rate of change of the corresponding functions in M as you

move along a coordinate vector x_μ of M. The *dual basis vectors* $\{e^\mu = \mathrm{d}x^\mu\}$ are defined such that $e^\mu(e_\nu) = \delta^\mu_\nu$. The metric tensor g is a function which defines the inner product of two tangent vectors v and w at a point p in M and produces a real scalar $g(v, w)$. This defines idea of distances on a manifold. *Greek* indices ranging over t, x, y are used to represent components of tensors with respect to the coordinate basis.

To work with spinors on a general spacetime we need to define an orthonormal basis with respect to the metric tensor g. The *dreibein basis* is a set of orthonormal basis vectors given by $\{e_a = e_a{}^\mu e_\mu\}$ with a corresponding dual basis $\{e^a = e^a{}_\mu e^\mu\}$, which satisfies $g(e_a, e_b) = \eta_{ab}$ and $e^a(e_b) = \delta^a_b$, where $\eta_{ab} = \mathrm{diag}(1, -1, -1)$ is the Minkowski metric. In components, these relations read

$$g_{\mu\nu} e_a{}^\mu e_b{}^\nu = \eta_{ab}, \quad e^a{}_\mu e_b{}^\mu = \delta^a_b, \tag{5.57}$$

where $g(e_\mu, e_\nu) = g_{\mu\nu}$ are the components of the metric with respect to the coordinate basis. Note the choice of dreibein basis is not unique. *Latin* indices ranging over $0, 1, 2$ are used to represent components of tensors with respect to the dreibein basis.

The components of the dreibein $e_a{}^\mu$ themselves are sometimes called the *dreibein*, while the components of the dual dreibein $e^a{}_\mu$ are called the *inverse dreibein* as they allow one to invert the expressions in (5.57). This thesis adopts the convention of calling them both the dreibein. The dreibein allow us to transform components between frames (basis representations), i.e. for a $(0, 1)$ tensor A we have $A_\mu = e^a{}_\mu A_a$ and $A_a = e_a{}^\mu A_\mu$, for a $(0, 2)$ tensor we need only look at the example of the metric tensor in (5.57) and so on for higher rank tensors. The metrics $g_{\mu\nu}$ and η_{ab} and their inverses $g^{\mu\nu}$ and η^{ab} lower and raise Greek and Latin indices, respectively.

5.2.2 Spin Connection

Differentiation is the process of comparing a tensor at two infinitesimally separated points on the manifold M. This presents a problem, tensors defined at different points are exist in different spaces. In order to compare tensors consistently we define the *covariant derivative* which can be viewed as the basis (or

frame) independent generalisation of the partial derivative at all points on M. Unlike the partial derivative of a tensor the covariant derivative transforms via a *covariant transformation* under a change of basis, retaining certain identifying properties in the same way that a tensor does. This is because the covariant derivative of a tensor is also a tensor. The covariant derivative of a rank $(1,1)$ tensor $A^{\mu}{}_{\nu}$ in the coordinate basis is given by

$$\nabla_{\alpha} A^{\mu}{}_{\nu} = \partial_{\alpha} A^{\mu}{}_{\nu} + \Gamma^{\mu}{}_{\beta\alpha} A^{\beta}{}_{\nu} - \Gamma^{\beta}{}_{\nu\alpha} A^{\mu}{}_{\beta}, \tag{5.58}$$

where $\Gamma^{\alpha}{}_{\beta\gamma}$ are the components of the *connection*. This definition can be extended to arbitrary rank tensors with a factor of $\Gamma^{\alpha}{}_{\beta\gamma}$ for each index of the tensor.

The covariant derivative is defined by the choice of connection. A *metric compatible* connection is one for which the metric is covariantly constant $\nabla g = 0$. Any metric compatible connection has the form

$$\Gamma^{\rho}{}_{\mu\nu} = \tilde{\Gamma}^{\rho}{}_{\mu\nu} + K^{\rho}{}_{\mu\nu}, \tag{5.59}$$

where $\tilde{\Gamma}^{\rho}{}_{\mu\nu}$ are the components of the unique torsion free metric compatible connection also known as the *Levi-Civita* connection or the *Christoffel symbols*, and $K^{\rho}{}_{\mu\nu}$ is the *contortion tensor*. The contortion tensor is given by

$$K^{\rho}{}_{\mu\nu} = \frac{1}{2}(T^{\rho}{}_{\mu\nu} + T_{\mu}{}^{\rho}{}_{\nu} + T_{\nu}{}^{\rho}{}_{\mu}). \tag{5.60}$$

where $T^{\rho}_{\mu\nu} = 2\Gamma^{\rho}_{[\mu\nu]}$ is the *torsion tensor*. Square brackets denote anti-symmetrisation over indices within the bracket, i.e. $\Gamma^{\rho}_{[\mu\nu]} = \frac{1}{2}(\Gamma^{\rho}_{\mu\nu} - \Gamma^{\rho}_{\nu\mu})$. The Levi-Civita connection is completely defined by the metric

$$\tilde{\Gamma}^{\rho}{}_{\mu\nu} = \frac{1}{2} g^{\rho\sigma}(\partial_{\mu} g_{\sigma\nu} + \partial_{\nu} g_{\sigma\mu} - \partial_{\sigma} g_{\mu\nu}), \tag{5.61}$$

and is symmetric on exchange of μ and ν. This is why we called the Levi-Civita connection "torsion free", as $T^{\rho}_{\mu\nu} = 2\Gamma^{\rho}_{[\mu\nu]} = 0$ if $\Gamma^{\rho}_{\mu\nu} = \tilde{\Gamma}^{\rho}_{\mu\nu}$. Torsion and the torsion tensor will be discussed in more detail in Section 5.2.3.

The covariant derivative can be written in terms of the dreibein basis. The covariant derivative of a $(1,1)$ tensor $A^{a}{}_{b}$ in the dreibein basis has a similar form to the coordinate basis in (5.58)

$$\nabla_{\mu} A^{a}{}_{b} = \partial_{\mu} A^{a}{}_{b} + \omega^{a}_{\mu c} A^{c}{}_{b} - \omega^{c}_{\mu b} A^{a}{}_{c}, \tag{5.62}$$

where $\omega^a_{\mu b}$ are the components of the *spin connection* given by

$$\omega^a_{\mu b} = e^a{}_\alpha(\partial_\mu e_b{}^\alpha + \Gamma^\alpha{}_{\beta\mu} e_b{}^\beta). \tag{5.63}$$

Besides defining the covariant derivative in the driebein basis, the spin connection allows one to take covariant derivatives of spinors. This will be discussed further in Section 5.2.4.

Metric compatible connections given by (5.59), result in spin connections of the form

$$\omega^a_{\mu b} = \tilde{\omega}^a_{\mu b} + K^a{}_{\mu b}, \tag{5.64}$$

where $\tilde{\omega}^a_{\mu b}$ is the Levi-Civita spin connection obtained by substituting the coordinate Levi-Civita connection from (5.61) into (5.63). The contortion tensor in the dreibein basis is $K^a_{\mu b} = e^a{}_\rho e_b{}^\nu K^\rho{}_{\mu\nu}$. Note, although the Levi-Civita connection is unique the Levi-Civita spin connection is not as the dreibein basis is non-unique. There is a unique Levi-Civita spin connection for each choice of driebein.

It can be shown that if the connection is metric compatible as in (5.59) then $\nabla_\mu e_a{}^\nu = 0$, where we have taken the dreibein $e_a{}^\mu$ to be the components of a $(1,1)$ tensor. This is sometimes called the *dreibein postulate* or the *tetrad postulate*.

5.2.3 Curvature and Torsion

The connection defines the curvature and torsion of a spacetime. It is beneficial to first discuss the geometrical meaning of these quantities. To do this we need to introduce the idea of *parallel transport*. Parallel transport can be crudely defined as the act of transporting a tensor A along a curve defined on the manifold M while keeping its relative orientation to the manifold constant. The components of a $(1,1)$ tensor A^μ_ν for example, vary with the basis vectors e_μ and e^ν to keep the relative orientation constant. More concretely the condition for parallel transport of a tensor is the components of the covariant derivative of the tensor vanish, i.e. $\nabla A = 0$ or for a $(1,1)$ tensor

$$\nabla_\alpha A^\mu{}_\nu = 0. \tag{5.65}$$

With this definition let us now discuss the geometrical meaning of torsion. Take the point p with coordinates $\{x^\rho\}$ and the infinitesimal vectors $X = \epsilon^\rho e_\rho$ and

$Y = \delta^\rho e_\rho$. Parallel transporting X along the infinitesimal displacement defined by Y to the point s with coordinates $\{x^\rho + \delta^\rho\}$ and vice versa for Y to q with coordinates $\{x^\rho + \epsilon^\rho\}$ results in two vectors sr_1 and qr_2 respectively. These are defined as $sr_1 = \epsilon^\rho + (\partial_\nu \epsilon^\rho)\delta^\nu$ and $qr_2 = \delta^\rho + (\partial_\mu \delta^\rho)\epsilon^\mu$. The vectors X, Y, sr_1 and qr_2 do not in general define a closed parallelogram as the points r_1 and r_2 do not necessarily coincide. The vector $r_1 r_2$ is given by

$$\begin{aligned} r_1 r_2 &= pq + qr_2 - ps - sr_1 \\ &= T^\rho{}_{\mu\nu}\epsilon^\mu \delta^\nu, \end{aligned} \tag{5.66}$$

where $T^\rho_{\mu\nu}$ is the *torsion tensor* which has already been defined as

$$T^\rho{}_{\mu\nu} = 2\Gamma^\rho_{[\mu\nu]}, \tag{5.67}$$

with respect to the coordinate basis. Hence, the torsion tensor gives a measure of the separation of r_1 and r_2. Note in (5.66) we have used $\partial_\nu \epsilon^\rho = -\Gamma^\rho{}_{\mu\nu}\epsilon^\mu$ and $\partial_\mu \delta^\rho = -\Gamma^\rho{}_{\nu\mu}\delta^\nu$ which can be derived from the definition of parallel transport (5.65).

We now discuss the geometrical meaning of curvature. Parallel transporting a vector from a point p to r along two different paths will in general result in two different vectors. The difference in the resulting vectors is due the *Riemann tensor*, sometimes called the *Riemann curvature tensor*. Take a parallelogram $pqrs$ with coordinates $\{x^\rho\}$, $\{x^\rho + \epsilon^\rho\}$, $\{x^\rho + \epsilon^\rho + \delta^\rho\}$ and $\{x^\rho + \delta^\rho\}$, where ϵ^ρ and δ^ρ are infinitesimal displacements. A vector V_p defined at p will result in the vector V_r when parallel transported along $C = pqr$ and the vector V'_r when parallel transported along $C' = psr$. From the definition of the parallel transport (5.65) one finds the difference between these vectors is

$$V'_r - V_r = V^\sigma_p R^\rho_{\sigma\mu\nu}\epsilon^\mu \delta^\nu, \tag{5.68}$$

where V^σ_p are the components of V_p and $R^\rho_{\sigma\mu\nu}$ are the components of the Riemann tensor which gives the curvature of a connection and is defined as

$$R^\rho{}_{\sigma\mu\nu} = \partial_\mu \Gamma^\rho{}_{\nu\sigma} - \partial_\nu \Gamma^\rho{}_{\mu\sigma} + \Gamma^\rho{}_{\mu\lambda}\Gamma^\lambda{}_{\nu\sigma} - \Gamma^\rho{}_{\nu\lambda}\Gamma^\lambda{}_{\mu\sigma}. \tag{5.69}$$

From the Riemann tensor, we can define two more geometric quantities, the *Ricci tensor* $R_{\mu\nu}$ and the *Ricci scalar* R

$$R_{\mu\nu} = R^\sigma{}_{\mu\sigma\nu}, \quad R = R^\mu{}_\mu. \tag{5.70}$$

In terms of a full metric compatible connection $\Gamma^{\alpha}_{\mu\nu} = \tilde{\Gamma}^{\rho}{}_{\mu\nu} + K^{\rho}{}_{\mu\nu}$ the Riemann tensor is given by

$$\begin{aligned} R^{\rho}{}_{\sigma\mu\nu} = \tilde{R}^{\rho}{}_{\sigma\mu\nu} + 2\partial_{[\mu}K^{\rho}{}_{\nu]\sigma} + 2\tilde{\Gamma}^{\rho}_{[\mu|\lambda}K^{\lambda}{}_{\nu]\sigma} \\ + 2K^{\rho}{}_{[\mu|\lambda}\tilde{\Gamma}^{\lambda}_{\nu]\sigma} + 2K^{\rho}{}_{[\mu|\lambda}K^{\lambda}{}_{\nu]\sigma}, \end{aligned} \tag{5.71}$$

where $\tilde{R}^{\rho}{}_{\sigma\mu\nu}$ is defined by replacing all $\Gamma^{\alpha}{}_{\beta\mu}$ in (5.69) with the Levi-Civita connection $\tilde{\Gamma}^{\alpha}{}_{\beta\mu}$. The square bracket notation $A_{[\mu|\nu}B_{\rho]}$ denotes anti-symmetrisation over μ and ρ, leaving ν unchanged. The corresponding Ricci scalar can be written as

$$R = \tilde{R} - K_{\rho\mu\nu}K^{\rho\mu\nu}, \tag{5.72}$$

where it is assumed that the contortion is completely anti-symmetric. This assumption is made because spinor fields on Riemann-Cartan geometry only couple to the completely anti-symmetric part of the contorsion and torsion tensors. This will be discussed in more detail in Section 5.2.4. The Ricci scalar gives the scalar curvature of spacetime.

5.2.4 Spinor Fields on Riemann-Cartan Geometry

The Dirac Action

The action for a spin-$\frac{1}{2}$ particle ψ of mass m defined on a general (2+1)−dimensional Riemann-Cartan spacetime (M, g) is given by Nakahara (2003)

$$S_{\text{RC}} = \frac{i}{2}\int_M \mathrm{d}^{2+1}x|e|\left(\bar{\psi}\gamma^{\mu}D_{\mu}\psi - \overline{D_{\mu}\psi}\gamma^{\mu}\psi + 2im\bar{\psi}\psi\right), \tag{5.73}$$

where $\{\gamma^{\mu}\}$ are the *curved* space gamma matrices. These matrices obey the Clifford algebra $\{\gamma^{\mu}, \gamma^{\nu}\} = 2g^{\mu\nu}$ and are related to the flat space gamma matrices $\{\gamma^{a}\}$ defined in (5.40) via $\gamma^{\mu} = e_a{}^{\mu}\gamma^{a}$, which obey the flat space Clifford algebra $\{\gamma^{a}, \gamma^{b}\} = 2\eta^{ab}$. The gamma matrices obey $(\gamma^{a})^{\dagger} = \gamma^{0}\gamma^{a}\gamma^{0}$. The object $|e| = |\det[e^{a}{}_{\mu}]|$ which from (5.57) obeys $|e| = \sqrt{|g|}$, where g is the determinant of the metric. The flat space gamma matrices are used to define the *Dirac adjoint* $\bar{\psi} = \psi^{\dagger}\gamma^{0}$.

The covariant derivative of a spinor ψ is given by

$$D_{\mu}\psi = \partial_{\mu}\psi + \omega_{\mu}\psi, \tag{5.74}$$

$$\overline{D_{\mu}\psi} = (D_{\mu}\psi)^{\dagger}\gamma^{0} = \partial_{\mu}\bar{\psi} - \bar{\psi}\omega_{\mu}, \tag{5.75}$$

where ω_μ is given by

$$\omega_\mu = \frac{i}{2}\omega_{\mu ab}\Sigma^{ab}, \quad \Sigma^{ab} = \frac{i}{4}[\gamma^a, \gamma^b], \tag{5.76}$$

and $\omega_{\mu ab} = \eta_{ac}\omega^c_{\mu b}$ are the components of the spin connection defined in (5.63). The notation D_μ is used instead of ∇_μ to distinguish between the covariant derivative of a spinor and that of a tensor. The rest of this thesis will refer to ω_μ as the connection as well.

To quantise this theory the curved space anti-commutation relations are imposed on the spinors

$$\begin{aligned} \{\psi_\alpha(t,\boldsymbol{x}), \psi_\beta(t,\boldsymbol{x}')\} &= \{\psi^\dagger_\alpha(t,\boldsymbol{x}), \psi^\dagger_\beta(t,\boldsymbol{x}')\} = 0, \\ \{\psi^\dagger_\alpha(t,\boldsymbol{x}), \psi_\beta(t,\boldsymbol{x}')\} &= \frac{i}{|e|}\delta_{\alpha\beta}\delta^{(2)}(\boldsymbol{x}-\boldsymbol{x}'), \end{aligned} \tag{5.77}$$

where α, β label the components of the spinors and $\delta^{(2)}(\boldsymbol{x}-\boldsymbol{x}')$ is the two dimensional Dirac delta function.

As shown in Section 5.1.4, the continuum limit of the Kitaev honeycomb model can be described with a single-particle Hamiltonian (5.47) expressed with respect to a spinor field Ψ obeying *flat* spacetime anti-commutation relations i.e. (5.77) with $|e| = 1$. Chapter 6 focuses on comparing the single particle Kitaev and quantum field theory Hamiltonians. This means the corresponding spinors of each must satisfy the same anti-commutation relations. Hence, the spinors ψ of the Riemann-Cartan theory in (5.73) are renormalised by defining

$$\chi = \sqrt{|e|}\psi, \tag{5.78}$$

which indeed obeys the flat spacetime anti-commutation relations, $\{\chi^\dagger_\alpha(t,\boldsymbol{x}), \chi_\beta(t,\boldsymbol{x}')\} = i\delta_{\alpha\beta}\delta^{(2)}(\boldsymbol{x}-\boldsymbol{x}')$. The identification $\Psi = \chi$ can then be made between the spinors of the Kitaev model around the Fermi points (5.37) and those of the Riemann-Cartan theory (5.78).

Substituting the new spinor χ into the Dirac action (5.73) and explicitly expanding out the covariant derivatives gives

$$S_{\text{RC}} = \frac{i}{2}\int_M \mathrm{d}^{2+1}x \left(\bar{\chi}\gamma^\mu\partial_\mu\chi - \partial_\mu\bar{\chi}\gamma^\mu\chi + \bar{\chi}\{\gamma^\mu, \omega_\mu\}\chi\right), \tag{5.79}$$

where $m = 0$ is taken until the end of this section in order to tidy up the algebra. Integrating by parts to remove $\partial_\mu \bar{\chi}$ gives

$$S_{\mathrm{RC}} = \int \mathrm{d}^{2+1}x \bar{\chi} \left(i\gamma^\mu \partial_\mu + \frac{i}{2}\{\gamma^\mu, \omega_\mu\} + \frac{i}{2}\partial_\mu \gamma^\mu \right) \chi. \tag{5.80}$$

It can be shown that in $(2+1)-$dimensional spacetime $\{\gamma^a, [\gamma^b, \gamma^c]\} = 4\epsilon^{abc}\gamma^0\gamma^1\gamma^2$, where ϵ^{abc} is the Levi-Civita symbol. The Levi-Civita symbol is totally anti-symmetric on exchange of any two indices. Hence, the second term in the integrand can be written as

$$\{\gamma^\mu, \omega_\mu\} = -\frac{1}{8}\omega_{\mu ab}\{e_c{}^\mu \gamma^c, [\gamma^a, \gamma^b]\} = -\frac{1}{2}\omega_{abc}\epsilon^{abc}\gamma^0\gamma^1\gamma^2, \tag{5.81}$$

where $\omega_{abc} = e_a{}^\mu \omega_{\mu bc}$. The action is then given by

$$S_{\mathrm{RC}} = \int \mathrm{d}^{2+1}x \bar{\chi} \left(i\gamma^\mu \partial_\mu - \frac{i}{4}\omega_{abc}\epsilon^{abc}\gamma^0\gamma^1\gamma^2 + \frac{i}{2}\partial_\mu \gamma^\mu \right) \chi. \tag{5.82}$$

The Hamiltonian

To produce a Riemann-Cartan Hamiltonian comparable to the Hamiltonian of the Kitaev honeycomb model (5.48) one must first restrict to the appropriate type of spacetime. A static spacetime is one which is constant in time and time-reversal invariant Schutz (2009); Wald (1984). These conditions are both true for the Kitaev honeycomb model with couplings that are constant in time. Hence, (M, g) is restricted to be a static spacetime with M taking the form

$$M = \mathbb{R} \times \Sigma \tag{5.83}$$

with the coordinate system (t, x^i), where $\mathbb{R}$ corresponds to time and Σ is a two dimensional "spacial" curved surface. In this way, only the purely spatial part of spacetime is curved with an orthogonal "temporal" vector field which can be viewed simply as some parameter. This corresponds to the geometric description of the Kitaev model as time remains unaffected by the distortion of the system's couplings.

The metric tensor g takes a block-diagonal form in this coordinate system

$$g_{\mu\nu} = \begin{pmatrix} 1 & 0 & 0 \\ 0 & g_{xx} & g_{xy} \\ 0 & g_{xy} & g_{yy} \end{pmatrix} \tag{5.84}$$

and is constant in coordinate time, $\partial_t g_{\mu\nu} = 0$, as long as the system's couplings are similarly constant. The dreibein that corresponding to this metric take the form

$$e^a{}_\mu = \begin{pmatrix} 1 & 0 & 0 \\ 0 & e^1{}_x & e^1{}_y \\ 0 & e^2{}_x & e^2{}_y \end{pmatrix}, \quad e_a{}^\mu = \begin{pmatrix} 1 & 0 & 0 \\ 0 & e_1{}^x & e_1{}^y \\ 0 & e_2{}^x & e_2{}^y \end{pmatrix}, \tag{5.85}$$

where the convention taken is that the index a runs down the columns while the index μ runs along the rows.

From the definition (5.61), it is clear that all time components of the Levi-Civita connection $\tilde{\Gamma}^\rho{}_{\mu\nu}$ will vanish, $\tilde{\Gamma}^t{}_{\mu\nu} = \tilde{\Gamma}^\rho{}_{t\nu} = \tilde{\Gamma}^\rho{}_{\nu t} = 0$. This along with the definition (5.63) means the time components of the corresponding Levi-Civita spin connection will also vanish, $\tilde{\omega}^a_{tb} = \tilde{\omega}^0_{\mu b} = \tilde{\omega}^a_{\mu 0} = 0$. The contortion of the spin connection remains unaffected. Expanding out the spin connection term in the action (5.82) gives

$$\omega_{abc}\epsilon^{abc} = \tilde{\omega}_{abc}\epsilon^{abc} + K_{abc}\epsilon^{abc} = \frac{1}{2}T_{abc}\epsilon^{abc}, \tag{5.86}$$

where the contortion is replaced with torsion using the definition (5.60) and the fact that $\tilde{\omega}_{abc}\epsilon^{abc} = 0$ on a $(2+1)-$dimensional static spacetime is used. This can be easily derived by observing that $\epsilon^{abc} = 0$ if any of the indices a, b, and c are equal. However, if the indices are unique then $\tilde{\omega}_{abc} = 0$ as one must necessarily be the time component in $2+1$ dimensions.

Due to (5.86), the spinor field only couples to the completely anti-symmetric part of the torsion T_{abc} or contorsion K_{abc}. For this reason, without loss of generality, the torsion can be taken to to be completely anti-symmetric

$$T_{abc} = \frac{1}{3!}\phi\epsilon_{abc}, \tag{5.87}$$

where ϕ is referred to as the *torsion pseudoscalar*. This is the assumption made to produce (5.72).

Using (5.86) and (5.87), the action (5.82) reduces to the simple form

$$\begin{aligned} S_{\text{RC}} &= \int \mathrm{d}^{2+1}x\bar{\chi}\left(i\gamma^\mu\partial_\mu - \frac{i}{8}\phi\gamma^0\gamma^1\gamma^2 + \frac{i}{2}\partial_i\gamma^i\right)\chi \\ &\equiv \int \mathrm{d}^{2+1}x\mathcal{L}_{\text{RC}}, \end{aligned} \tag{5.88}$$

where $\mathcal{L}_{\mathrm{RC}}$ is the Lagrangian density.

With a static spacetime, the Hamiltonian can be defined from the Lagrangian density via a Legendre transformation as

$$H_{\mathrm{RC}} = \int \mathrm{d}^2x \left(\frac{\partial \mathcal{L}_{\mathrm{RC}}}{\partial \dot{\chi}} \dot{\chi} - \mathcal{L}_{\mathrm{RC}} \right) \equiv \int \mathrm{d}^2x \chi^\dagger h_{\mathrm{RC}} \chi, \tag{5.89}$$

where h_{RC} is the single-particle Hamiltonian given by

$$h_{\mathrm{RC}} = e_a{}^i \gamma^0 \gamma^a p_i + \frac{i}{8} \phi \gamma^1 \gamma^2 + \frac{i}{2} \partial_i e_a{}^i \gamma^0 \gamma^a + m\gamma^0, \tag{5.90}$$

where the mass m has be reintroduced and $p_i = -i\partial_i$ is the canonical momentum operator. Hence, (5.89) gives the form of a Hamiltonian of spinors on a static Riemann-Cartan spacetime.

The formulas presented here are used in Chapter 6 to determine the effective curvature and torsion of the Kitaev honeycomb model with various coupling parameters. The geometric meaning of the couplings of the Kitaev model are derived through comparison of the single particle Hamiltonian (5.90) with a generalised version of (5.47). The behaviour of the two-point correlations and vortex excitations of the Kitaev honeycomb model are numerically studied showing a strong agreement with the Riemann-Cartan description.

5.3 Summary

This chapter introduced the basics of the Kitaev honeycomb model. A Dirac Hamiltonian describing the continuum limit behaviour of the model is derived from its original definition as a model of interacting spin-1/2 particles on a lattice. This chapter also presents the components of $(2+1)-$dimensional Riemann-Cartan geometry and uses them to define a Hamiltonian of spinors on a spacetime with curvature and torsion.

The next chapter brings these two topics together to produce an effective geometric description of the Kitaev honeycomb model, relating coupling parameters of the Kitaev honeycomb model to components of $(2+1)-$dimensional Riemann-Cartan geometry. The accuracy of this description is studied numerically by analysing the response of physical observables to variations in the couplings.

Specifically the spacial profiles of two-point correlations and vortex excitations are studied.

Chapter 6

Geometric description of the Kitaev honeycomb lattice model

This chapter studies the continuum limit of the Kitaev honeycomb model in a variety of coupling regimes deriving a geometric description of the model in terms of Majorana spinors obeying the Dirac equation embedded in a Riemann-Cartan spacetime. Moreover, the Majorana spinors are coupled to a non-trivial torsion. This geometry emerges purely from distortions in the couplings of the system and *not* from the geometry of the lattice itself. Note, this description is numerically verified by studying the behaviour of the spacial distribution of the quantum correlations in the ground state of the model. As the couplings are varied the numerically observed geometric distortion of the two-point Majorana correlations agrees faithfully with the stretching of space theoretically predicted by the metric of the geometric description. Hence, the Riemann-Cartan description can be employed to accurately describe the behaviour of the Kitaev honeycomb model in a quantum field theory language. This opens up the exciting possibility to theoretically study dynamical or response properties of the model, such as the energy-momentum currents and momentum densities Golan & Stern (2018) as a function of coupling distortions or temperature gradients, in a quantitative way.

The continuum limit of the Kitaev honeycomb model is compared to the dirac equation in $(2+1)-$dimensional Riemann-Cartan spacetime. and coupling parameters of the model are identified with components of the spacetime. The nearest neighbour interactions define the non-trivial dreibein and metric. While

the next to nearest neighbour interactions couple the Majorana spinors of the theory to a non-trivial torsion. These spinors become massive when a Kekulé distortion is introduced to the nearest neighbour interactions.

The chapter is organised as follows. Section 6.1 demonstrates that the low energy limit of the Kitaev honeycomb model can be faithfully described by massless Majorana fermions propagating on a Riemann-Cartan background, with geometric characteristics fully determined by the coupling constants of the model. It is broken down into three parts each studying a different coupling regime. Section 6.1.1 looks at the isotropic regime, where $J_x = J_y = J_z = 1$. For this case it is also shown that a Kekulé distortion of the nearest neighbour couplings generates mass in the continuum limit. Section 6.1.2 studies the generally anisotropic regime, where all $\{J_i\}$ are independent of each other. Section 6.1.3 then restricts to a specific case of the anisotropic coupling regime, where $J_x = J_y = 1$ and $0 \leq J_z \leq 2$. Section 6.2 is broken down into two parts. Section 6.2.1 determines the specific form of the effective stretching predicted by the non-trivial metric for the specific anisotropic coupling regime studied in Section 6.1.3. Section 6.2.2 then presents a numerical investigation comparing this stretching to the observed distortions of the two point Majorana correlations for various coupling configurations within this regime, thus verifying the non-trivial description of the model in terms of the metric. Finally, Section 6.3 presents the conclusions and outlines possible areas of future research based on this work.

6.1 Riemann-Cartan geometry from the Kitaev model

This section compares the continuum limit single particle Hamiltonian of the Kitaev honeycomb model in a variety of coupling regimes to the Riemann-Cartan Hamiltonian given in (5.90). An effective geometric description of the model is formed and several components of the corresponding spacetime are identified with couplings of the microscopic model.

The non-trivial geometric features of a Riemann-Cartan theory are encoded in the dreibein $e_a{}^\mu$ and torsion pseudoscalar ϕ. These quantities are found to corre-

spond to the nearest and next to nearest neighbour interactions of the microscopic model, respectively. The curvature of the geometric theory is fully determined by the dreibein and torsion pseudoscalar. In order to achieve non-trivial curvature the couplings of the model are upgraded to space dependent parameters. It is assumed that the Fourier transformation (5.18) at each point in space is still approximately valid for space dependent couplings that vary slowly with respect to the overall magnitude of J and K. Hence, the continuum limit of the model is taken to be of the same form as the model with constant parameters, where the couplings have been simply upgraded to slowly varying space dependent functions. For this reason the $\partial_i e_a{}^i$ term of the general Riemann-Cartan Hamiltonian (5.90) is set to zero. The mass m of the Riemann-Cartan theory is identified with a Kekeulé distortion of the original Kitaev honeycomb model as presented in Yang *et al.* (2019).

This section is broken down as follows. Section 6.1.1 compares the continuum limit of the isotropic Kitaev model to the Riemann-Cartan theory. Section 6.1.2 derives the continuum limit of the generally anisotropic case, where the $\{J_i\}$ couplings are taken to be independent from one another. The K term is also modified in an anisotropic manner, such that the Fermi points still depend solely on the nearest neighbour couplings. Section 6.1.3 studies the geometric properties of a specific coupling regime within the generally anisotropic case, where $J_x = J_y = 1$ and $0 \leq J_z \leq 2$. The accuracy of the effective geometric description of this specific case is probed numerically in Section 6.2 by studying the response of two point Majorana correlations to variations in J_z.

6.1.1 The isotropic $J_x = J_y = J_z = J$ model

Consider the Kitaev honeycomb model with isotropic nearest neighbour couplings, $J_x = J_y = J_z = J$. The corresponding single particle continuum limit Hamiltonian for which J is a constant is given in (5.47) and repeated here for convenience

$$h_{\mathrm{KHLM}}(\boldsymbol{p}) = 3J(\gamma^0\gamma^1 p_x - \gamma^0\gamma^2 p_y) - i3\sqrt{3}K\gamma^1\gamma^2. \tag{6.1}$$

This can be interpreted as a Riemann-Cartan Hamiltonian of the form (5.90) and the corresponding dreibein, metric, curvature and torsion of the model can be identified.

Dreibein and Metric

A direct comparison of the isotropic continuum limit (6.1) with the Riemann-Cartan Hamiltonian (5.90) reveals that the dreibein of the model are given by

$$e_a{}^{\mu} = \begin{pmatrix} 1 & 0 & 0 \\ 0 & 3J & 0 \\ 0 & 0 & -3J \end{pmatrix}, \quad e^a{}_{\mu} = \begin{pmatrix} 1 & 0 & 0 \\ 0 & \frac{1}{3J} & 0 \\ 0 & 0 & -\frac{1}{3J} \end{pmatrix}, \tag{6.2}$$

with the corresponding metric

$$g_{\mu\nu} = e^a{}_{\mu} e^b{}_{\nu} \eta_{ab} = \begin{pmatrix} 1 & 0 & 0 \\ 0 & -\frac{1}{9J^2} & 0 \\ 0 & 0 & -\frac{1}{9J^2} \end{pmatrix}. \tag{6.3}$$

We see that the J term alone determines the metric of the model and is unaffected by the K term. The time components of the dreibein and metric are fixed by the assumption of a static spacetime (5.83).

Curvature and Torsion

For a static spacetime of the form $M = \mathbb{R} \times \Sigma$, the metric, after diagonalisation, takes the form

$$g_{\mu\nu} = \begin{pmatrix} 1 & 0 & 0 \\ 0 & F & 0 \\ 0 & 0 & G \end{pmatrix}, \tag{6.4}$$

where $F = F(x, y)$ and $G = G(x, y)$ are arbitrary functions of space only.

The curvature of a spacetime can be derived as in (5.71) from the Riemann tensor of the Levi-Civita connection and the contorsion tensor.

From (5.61) the metric (6.4) gives the components of the Levi-Civita connection as

$$\begin{aligned} \tilde{\Gamma}^x_{xx} &= \frac{1}{2F}\partial_x F, \quad \tilde{\Gamma}^x_{xy} = \tilde{\Gamma}^x_{yx} = \frac{1}{2F}\partial_y F, \\ \tilde{\Gamma}^x_{yy} &= -\frac{1}{2F}\partial_x G, \quad \tilde{\Gamma}^y_{yy} = \frac{1}{2G}\partial_y G, \\ \tilde{\Gamma}^y_{xy} &= \tilde{\Gamma}^y_{yx} = \frac{1}{2G}\partial_x G, \quad \tilde{\Gamma}^y_{xx} = -\frac{1}{2G}\partial_y F, \end{aligned} \tag{6.5}$$

where all of the time components vanish.

With a Levi-Civita connection of the form (6.5), the corresponding Ricci scalar is given by

$$\tilde{R} = -\frac{1}{2}\left[\partial_x\left(\frac{\partial_x G}{FG}\right) + \partial_y\left(\frac{\partial_y F}{FG}\right) + \frac{\partial_x^2 G + \partial_y^2 F}{FG}\right]. \tag{6.6}$$

Evaluating (6.6) for the isotropic case $F = G = -\frac{1}{9J^2}$ given in (6.3), by upgrading the parameter J to an arbitrary function of space yields the Ricci scalar

$$\tilde{R} = 2\partial^2 \ln J, \tag{6.7}$$

where $\partial^2 = g^{\mu\nu}\partial_\mu\partial_\nu$ is the Laplacian operator.

All of the time components of the Levi-Civita connection vanish. Thus all of the time components of the corresponding curvature will also vanish. This means it is sufficient to study the curvature of the two dimensional spatial hypersurface Σ. It can be shown from its definition (5.69) that the Riemann tensor of a two dimensional torsion free space satisfies the symmetries $\tilde{R}_{ijkl} = -\tilde{R}_{jikl}$, $\tilde{R}_{ijkl} = -\tilde{R}_{ijlk}$ and $\tilde{R}_{[ijk]l} = 0$. As before, square brackets denote anti-symmeterisation over all indices within the bracket. From these symmetries and the definitions of the Ricci tensor and scalar (5.70) it can further be shown that the Riemann tensor in a two dimensional space has only one independent component given by

$$\tilde{R}_{ijkl} = \frac{1}{2}\tilde{R}(g_{ik}g_{lj} - g_{il}g_{kj}), \tag{6.8}$$

where R is the Ricci scalar and i, j, k, l denote spatial components. Hence, the Riemann tensor is completely determined by the Ricci scalar (6.3) and the metric (6.7).

In order to obtain non-zero curvature from the Levi-Civita connection, the coupling constant J must be position dependent as $\partial_i J = 0$ implies $\tilde{R} = 0$. However, the continuum limit of the Kitaev honeycomb model was derived in Section 5.1.4 with the assumption that the couplings are constant $\partial_\mu J = 0$ and the system is homogeneous. It is proposed here that upgrading J to a position dependent parameter that varies slowly with respect to the overall magnitude of the couplings J and K means the Fourier transformation (5.18) at each point in space still holds approximately and the obtained effective curvature of the geometric picture is still valid. No specific numerics testing the accuracy of (6.8) are presented

in this thesis. Possible probes of the curvature may be bulk fermionic energy currents and momentum densities induced by a spacial derivatives of the Ricci scalar. These observables are studied theoretically in detail in Golan & Stern (2018) for a system of spinless fermions on a two dimensional square lattice.

Comparison of the Hamiltonians (6.1) and (5.90) reveals that the torsion pseudoscalar ϕ and mass m are given by

$$\phi = -24\sqrt{3}K, \quad m = 0. \tag{6.9}$$

From ϕ, via the relation (5.87), the corresponding components of the torsion and contortion in the dreibein basis are given by

$$T_{abc} = -4\sqrt{3}K\epsilon_{abc}, \quad K_{abc} = -2\sqrt{3}K\epsilon_{abc}, \tag{6.10}$$

The contorsion tensor K_{abc} also determines the total Ricci scalar via (5.72) which is given by

$$R = 2\partial^2 \ln J - 72K^2, \tag{6.11}$$

where the identity $\epsilon_{abc}\epsilon^{abc} = 6$ is used. The total Ricci scalar R is non-zero even when $\partial_i J = 0$ due to the contribution from the torsion pseudoscalar ϕ. Note that although (6.8) does not hold for spacetimes with torsion, the Riemann tensor is still completely defined by the Levi-Civita connection (6.5), the corresponding Ricci scalar (6.7) and the contorsion tensor (6.10) through the relation (5.71).

In summary, the continuum limit of the isotropic Kitaev honeycomb model describes massless Majorana fermions on a curved spacetime with torsion proportional to the next to nearest neighbour K term. The nearest neighbour J terms become the kinetic terms defining non-trivial dreibein. Both the J and K terms contribute to the curvature of the model.

The K term is inserted into the Kitaev honeycomb model as three-spin interactions which generates an energy gap and gives rise to a well defined non-Abelian topological phase discussed in Section 5.1.5. This energy gap is the microscopic signature of torsion in the continuum limit, not mass.

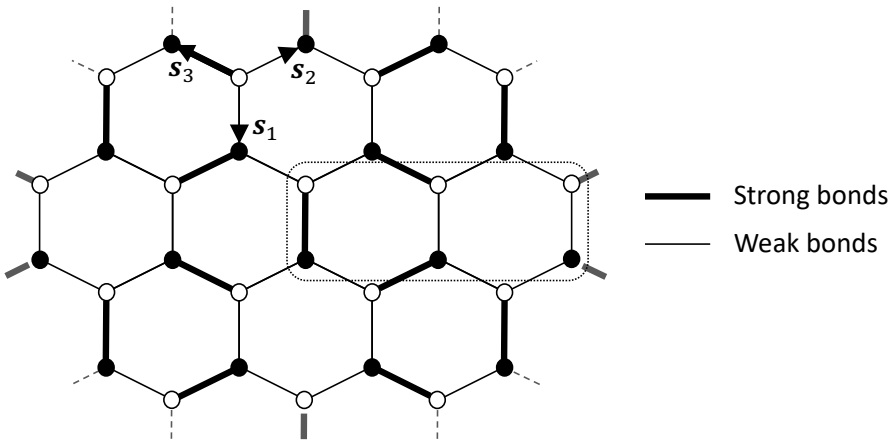

Figure 6.1: The Kekulé distortion in the couplings of the honeycomb lattice model, as described by Eqns. (6.12) and (6.13), which generate a mass term in the Hamiltonian. Strong and weak tunnelling couplings are indicated as thick and thin bonds, respectively, between lattice sites. This configuration of couplings is periodic with respect to a unit cell with six sites, as shown. The vectors $\boldsymbol{s}_1 = (0, -1)$, $\boldsymbol{s}_2 = (\frac{\sqrt{3}}{2}, \frac{1}{2})$ and $\boldsymbol{s}_3 = (-\frac{\sqrt{3}}{2}, \frac{1}{2})$, used in (6.12) and (6.13), which translate between lattices A and B are also depicted.

Mass from Kekulé distortion

The natural question now arises as to what term could be introduced to the microscopic Kitaev Hamiltonian (5.13) to give rise to mass in the continuum limit. One such term is a Kekulé distortion of the nearest neighbour couplings of the Majorana fermions as studied in Yang *et al.* (2019). This type of interaction has been theoretically studied in graphene for complex fermions and shown to generate a mass gap in Hou *et al.* (2007).

A Kekulé distortion is produced by introducing a term to the microscopic Hamiltonian of the Kitaev honeycomb model (5.13) of the form

$$\delta H = i \sum_{i \in A} \sum_{k=1}^{3} \delta J_{ik} c^a_{\boldsymbol{r}_i} c^b_{\boldsymbol{r}_i + \boldsymbol{s}_k} + \text{h.c.}, \tag{6.12}$$

where the sub-lattice A is defined in Fig. 5.2 and the vectors $\boldsymbol{s}_1 = (0, -1)$, $\boldsymbol{s}_2 = (\frac{\sqrt{3}}{2}, \frac{1}{2})$ and $\boldsymbol{s}_3 = (-\frac{\sqrt{3}}{2}, \frac{1}{2})$ are shown in Fig. 6.1. The J_i couplings for $i \in (x, y, z)$

are effectively inhomogeneously distorted by

$$\delta J_{ik} = \frac{M}{3} e^{i\boldsymbol{P}_+ \cdot \boldsymbol{s}_k} e^{i(\boldsymbol{P}_+ - \boldsymbol{P}_-)\cdot \boldsymbol{r}_i} + \text{c.c.}, \tag{6.13}$$

where $M = m + im_i$ is a complex constant number and $\boldsymbol{P}_\pm$ are the Fermi points of the model given in (5.32). This is a Kekulé distortion of the J couplings shown in Fig. 6.1.

The Kekulé distortion expands the unit cell of the lattice to include six sites rather than the original two, causing the Brillouin zone to fold three times compared to the undisturbed case. Fourier transforming and restricting to low energy contributions near the Fermi points (6.12) gives, up to first order in momenta, Yang *et al.* (2019)

$$\delta H = \Psi^\dagger(\gamma^0 m + \gamma^0\gamma^5 m_i)\Psi. \tag{6.14}$$

The contribution to the single-particle Hamiltonian (5.47) is

$$h_m = m\gamma^0 + \gamma^0\gamma^5 m_i, \tag{6.15}$$

where γ^0 and γ^5 are given in (5.39) and (5.41) respectively. The first term is equivalent to the mass term in (5.90). Hence, the Majoranas fermions in the geometric description of the Kitaev honeycomb model acquire a mass from a non-trivial real Kekulé distortion. The second term takes the form of an imaginary mass or pseudoscalar term present in the "tachyonic" Dirac Hamiltonian Jentschura (2012).

When $M = 0$, the K term produces an energy gap due to a non-zero torsion and breaks time reversal and chiral symmetry. The model is in the $\mathcal{B}$ phase in Fig. 6.4 in Section 5.1.5, a $p+ip$ superconductor in the D class with a non-trivial Chern number $\nu = 1$ Chiu *et al.* (2016). On the other hand, when $K = 0$ the Kekulé distortion creates an energy gap in the Kitaev model proportional to a non-zero mass M_0, where $M = M_0 e^{i\phi}$. Time reversal and chiral symmetry of the model are no longer broken. This phase of the system belongs to the BDI class with a trivial Chern number $\nu = 0$ Chiu *et al.* (2016). Upgrading ϕ to a space dependent parameter can produce vortices, which trap chiral Majorana zero modes Jackiw & Rossi (1981); Yang *et al.* (2019).

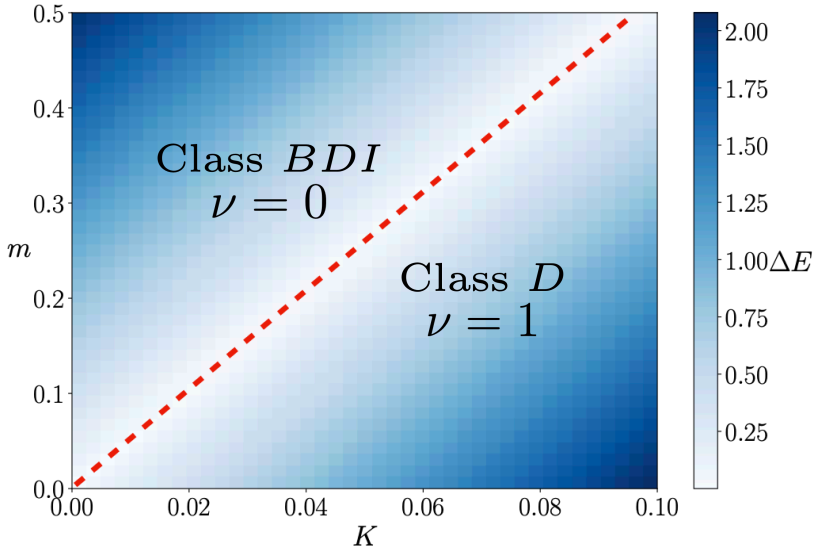

Figure 6.2: Phase diagram of the KHLM with its energy gap ΔE varying as a function of the K coupling and the mass, m. By increasing the Kekulé distortion a first order phase transition is induced from the gapped topological phase of the KHLM with Chern number $\nu = 1$ that belongs in class D to a gapped Kekulé phase with Chern number $\nu = 0$ that belongs in class BDI. Both of these phases support vortices that bound Majorana zero modes. The red dashed line denotes the analytically obtained phase transition boundary.

There is a phase transition between the BDI and D class of the extended Kitaev model. The phase diagram of the model for varying m and K is plotted in Fig. 6.2, where $m_i = \phi = 0$. The quantum field theory description of the isotropic homogeneous model is given by the single particle Hamiltonian (5.90), where $\phi = -24\sqrt{3}K$ and $\partial_i e^i_a = 0$. The phase transition occurs when the energy gap is at a minimum, so the Hamiltonian is studied exactly at the Fermi points $p_i = 0$. The Hamiltonian becomes a sum of two commuting terms $[i\gamma^1\gamma^2, \gamma^0] = 0$. Therefore, the phase transition should occur when the coefficients are equal $m = 3\sqrt{3}K$. This is in agreement with Fig. 6.2, where the red dotted line marks out this relation between m and K. As the terms commute this is a first order phase transition due to an energy level crossing.

Section 6.1.2 performs a comparable investigation to that of the isotropic case

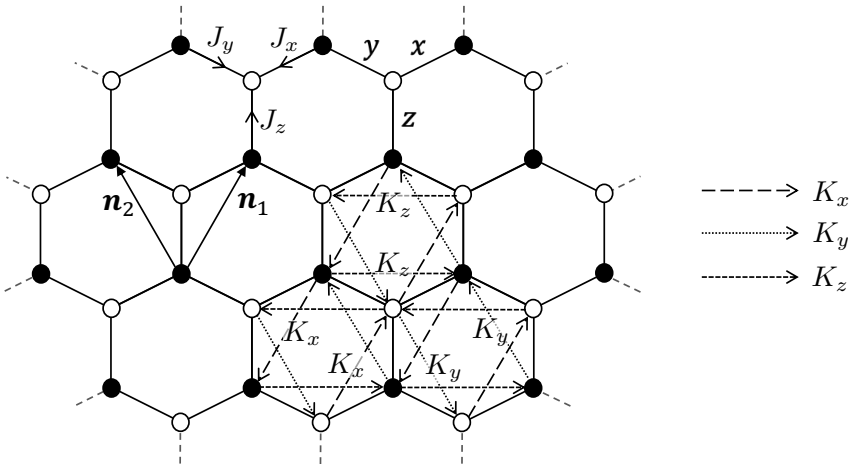

Figure 6.3: The anisotropic KHLM is given by choosing the couplings J_x, J_y and J_z to be unequal, giving rise to an anisotropic model. In order to have the K-term contribute purely to an energy gap the couplings K_x, K_y and K_z are chosen to be also anisotropic and functions of J_i's, as given by (6.28).

in this Section and Section 5.1.4 for the generally anisotropic case. That is for the Kitaev model with J_x, J_y and J_z couplings all independent of each other. The K term is also modified in an anisotropic manner. Mass producing terms are not studied for any of the other cases considered in this chapter, although it is predicted that they will be similar in form to (6.12).

6.1.2 The generally anisotropic J coupling case

This section considers the Kitaev honeycomb model with anisotropic J couplings where all $\{J_i\}$ are independent of each other. The next to nearest neighbour Majorana interactions are also modified, producing anisotropy in the K terms taking values K_x, K_y and K_z depending on the orientation of the links, as shown in Fig. 6.3. This is to ensure that the Fermi points remain independent of K. This will be discussed in more detail later in this section. This case is referred to as the generally anisotropic case.

Continuum Limit

The continuum limit of the isotropic model was presented in Section 5.1.4. This calculation is repeated here for the generally anisotropic case with constant couplings. The Hamiltonian can be written as a sum of the nearest neighbour interactions given in (5.17) and next to nearest neighbour interactions, shown in Fig. 6.3, taking the modified form

$$\begin{aligned} H_2 = iK \sum_{\boldsymbol{r}} & c^a_{\boldsymbol{r}}(-K_x c^a_{\boldsymbol{r}+\boldsymbol{n}_1} + K_y c^a_{\boldsymbol{r}+\boldsymbol{n}_2} + K_z c^a_{\boldsymbol{r}+\boldsymbol{n}_1-\boldsymbol{n}_2}) \\ & + c^b_{\boldsymbol{r}}(K_x c^b_{\boldsymbol{r}+\boldsymbol{n}_1} - K_y c^b_{\boldsymbol{r}+\boldsymbol{n}_2} - K_z c^b_{\boldsymbol{r}+\boldsymbol{n}_1-\boldsymbol{n}_2}) + \text{h.c.} \end{aligned} \tag{6.16}$$

The continuum limit Hamiltonian in momentum space takes the familiar form $H = \int \mathrm{d}^2 q \psi^\dagger_{\boldsymbol{q}} h(\boldsymbol{q}) \psi_{\boldsymbol{q}}$ from (5.26), where $\psi_{\boldsymbol{q}} = (c^a_{\boldsymbol{q}}\ ic^b_{\boldsymbol{q}})^{\mathrm{T}}$, and the single-particle Hamiltonian $h(\boldsymbol{q})$ is given by

$$h(\boldsymbol{q}) = \begin{pmatrix} \Delta(\boldsymbol{q}) & -f(\boldsymbol{q}) \\ -f^*(\boldsymbol{q}) & -\Delta(\boldsymbol{q}) \end{pmatrix}, \tag{6.17}$$

where

$$f(\boldsymbol{q}) = 2(J^x e^{i\boldsymbol{q}\cdot\boldsymbol{n}_1} + J^y e^{i\boldsymbol{q}\cdot\boldsymbol{n}_2} + J^z), \tag{6.18}$$

as in (5.21) and

$$\begin{aligned} \Delta(\boldsymbol{q}) = 2\big[& - K_x \sin(\boldsymbol{q}\cdot\boldsymbol{n}_1) + K_y \sin(\boldsymbol{q}\cdot\boldsymbol{n}_2) \\ & + K_z \sin(\boldsymbol{q}\cdot(\boldsymbol{n}_1 - \boldsymbol{n}_2))\big] \end{aligned} \tag{6.19}$$

as can be seen from a modified (5.25).

Consider the Fermi points of the system for the case $K_i = 0$ for all i. As in the isotropic case $E(\boldsymbol{q}) = \pm|f(\boldsymbol{q})|$. This is at a minimum when $f(\boldsymbol{q}) = 0$, giving the equations for the real and imaginary parts of (6.18)

$$J_x \cos(\boldsymbol{q}\cdot\boldsymbol{n}_1) + J_y \cos(\boldsymbol{q}\cdot\boldsymbol{n}_2) + J_z = 0, \tag{6.20}$$

$$J_x \sin(\boldsymbol{q}\cdot\boldsymbol{n}_1) + J_y \sin(\boldsymbol{q}\cdot\boldsymbol{n}_2) = 0. \tag{6.21}$$

These have two solutions corresponding to the two Fermi points located at

$$\boldsymbol{P}_\pm = \pm \begin{pmatrix} \frac{1}{\sqrt{3}}\big(\mathrm{sgn}(J_y)\arccos(a) + \mathrm{sgn}(J_x)\arccos(b)\big) \\ \frac{1}{3}\big(\mathrm{sgn}(J_y)\arccos(a) - \mathrm{sgn}(J_x)\arccos(b)\big) \end{pmatrix}, \tag{6.22}$$

where

$$a = \frac{J_y^2 - J_x^2 - J_z^2}{2J_xJ_z}, \quad b = \frac{J_x^2 - J_y^2 - J_z^2}{2J_yJ_z}. \tag{6.23}$$

Taylor expanding to first order about these points gives

$$f(\boldsymbol{P}_\pm + \boldsymbol{p}) = f(\boldsymbol{P}_\pm) + \boldsymbol{p}\cdot\boldsymbol{\nabla} f(\boldsymbol{P}_\pm) + O(p^2), \tag{6.24}$$

$$\Delta(\boldsymbol{P}_\pm + \boldsymbol{p}) = \Delta(\boldsymbol{P}_\pm) + \boldsymbol{p}\cdot\boldsymbol{\nabla}\Delta(\boldsymbol{P}_\pm) + O(p^2). \tag{6.25}$$

The first order terms are given by

$$\begin{aligned}\boldsymbol{\nabla} f(\boldsymbol{P}_\pm) = 2i\Big[&J_x\left(a \pm i\sqrt{1-a^2}\right)\boldsymbol{n}_1 \\ &+ J_y\left(b \mp i\sqrt{1-b^2}\right)\boldsymbol{n}_2\Big],\end{aligned} \tag{6.26}$$

$$\begin{aligned}\boldsymbol{\nabla}\Delta(\boldsymbol{P}_\pm) = 2\Big[&-K_x a\boldsymbol{n}_1 + K_y b\boldsymbol{n}_2 \\ &+K_z\left(ab - \sqrt{1-a^2}\sqrt{1-b^2}\right)(\boldsymbol{n}_1 - \boldsymbol{n}_2)\Big].\end{aligned} \tag{6.27}$$

Section 6.1.1 shows that in the continuum limit of the isotropic case $f(\boldsymbol{p})$ corresponds to the kinetic term and defines the Fermi points while $\Delta(\boldsymbol{p})$ produces an energy gap at these Fermi points. To keep this separation of the kinetic and gap producing terms $\Delta(\boldsymbol{p})$ must not shift the Fermi points. Hence, the couplings $\{K_i\}$ are chosen such that (6.27) vanishes

$$\begin{aligned}K_x &= 4Kb\left(ab - \sqrt{1-a^2}\sqrt{1-b^2}\right), \\ K_y &= 4Ka\left(ab - \sqrt{1-a^2}\sqrt{1-b^2}\right), \\ K_z &= 4Kab,\end{aligned} \tag{6.28}$$

where $K \in \mathbb{R}$ determines the overall magnitude of the couplings and the factor of 4 ensures the gap agrees with the one obtained in the isotropic case.

The energy gap at each Fermi point is given by $\Delta(\boldsymbol{P}_\pm) = \pm\Delta$, where

$$\Delta = 8K\sqrt{(1-a^2)(1-b^2)}\left(a\sqrt{1-b^2} + b\sqrt{1-a^2}\right). \tag{6.29}$$

Note, at the isotropic point, $J_x = J_y = J_z = J$, (6.23) gives $a = b = -1/2$, (6.26) reduces to (5.33) and (6.29) reproduces the corresponding gap $\Delta = 3\sqrt{3}K$, all in agreement with the isotropic Hamiltonian (6.30).

Using (6.26) and (6.29) the single particle Hamiltonian (6.17) is expanded about the Fermi points as in (5.35) to give

$$h_{\pm}(\boldsymbol{p}) = (\pm A\sigma^x + B\sigma^y)p_x + C\sigma^y p_y \mp \Delta\sigma^z + O(\boldsymbol{p}^2), \tag{6.30}$$

where

$$\begin{aligned} A &= \mathrm{sgn}(J_x)\mathrm{sgn}(J_y)\sqrt{12J_x^2 - 3\frac{(J_y^2 - J_x^2 - J_z^2)^2}{J_z^2}}, \\ B &= \sqrt{3}\frac{(J_y^2 - J_x^2)}{J_z^2}, \\ C &= -3J_z. \end{aligned} \tag{6.31}$$

To consider the Fermi points simultaneously in the Weyl (chiral) basis as in Section 5.1.4 the four component spinor $\Psi = (c_+^a \; ic_+^b \; ic_-^b \; c_-^a)^{\mathrm{T}}$ is defined (5.37), where $c_\pm^{a/b} = c_{\boldsymbol{P}_\pm}^{a/b}$ are now defined at the new Fermi points (6.22). Taking the direct sum of the Hamiltonians $h_+(\boldsymbol{p})$ and $h_-(\boldsymbol{p})$ with respect to the basis defined by Ψ yields the final generally anisotropic Hamiltonian

$$\begin{aligned} h_{\mathrm{KHLM}} = &(A\sigma^z \otimes \sigma^x + B\sigma^z \otimes \sigma^y)\, p_x \\ &+ C\sigma^z \otimes \sigma^y p_y + \Delta\mathbb{I} \otimes \sigma^z. \end{aligned} \tag{6.32}$$

This can be written in terms of gamma matrices defined in (5.40), to give

$$h_{\mathrm{KHLM}} = (A\gamma^0\gamma^1 + B\gamma^0\gamma^2)p_x + C\gamma^0\gamma^2 p_y + i\Delta\gamma^1\gamma^2, \tag{6.33}$$

This reduces to the original isotropic continuum limit given in (5.47) when $J_x = J_y = J_z = J$.

The Metric and Torsion

Direct comparison of the generally anisotropic continuum limit Hamiltonian (6.33) with the general Riemann-Cartan Hamiltonian (5.90) for constant parameters shows the dreibein of the model are given by

$$e_a{}^\mu = \begin{pmatrix} 1 & 0 & 0 \\ 0 & A & 0 \\ 0 & B & C \end{pmatrix}, \quad e^a{}_\mu = \begin{pmatrix} 1 & 0 & 0 \\ 0 & \frac{1}{A} & 0 \\ 0 & -\frac{B}{AC} & \frac{1}{C} \end{pmatrix} \tag{6.34}$$

with the corresponding metric

$$g_{\mu\nu} = e^{a}{}_{\mu} e^{b}{}_{\nu} \eta_{ab} = \begin{pmatrix} 1 & 0 & 0 \\ 0 & -\frac{1}{A^2} - \frac{B^2}{A^2 C^2} & \frac{B}{AC^2} \\ 0 & \frac{B}{AC^2} & -\frac{1}{C^2} \end{pmatrix}. \tag{6.35}$$

The torsion pseudoscalar and mass are easily identified as

$$\phi = 8\Delta, \quad m = 0. \tag{6.36}$$

From ϕ, via the relation (5.87), the corresponding components of the torsion and contortion in the dreibein basis are given by

$$T_{abc} = -\frac{4}{3}\Delta\epsilon_{abc}, \quad K_{abc} = -\frac{2}{3}\Delta\epsilon_{abc}, \tag{6.37}$$

Interestingly, the singularities of the metric (6.35), when $A = 0$ or $C = 0$, correspond to the well studied phase transitions of the Kitaev honeycomb model Kitaev (2006) detailed in Section 5.1.5. The condition $A = 0$ is equivalent to the couplings satisfying one of the following relations

$$\begin{aligned} J_x + J_y + J_z &= 0, \\ J_x - J_y - J_z &= 0, \\ J_x - J_y + J_z &= 0, \\ J_x + J_y - J_z &= 0. \end{aligned} \tag{6.38}$$

If the assumption is made that $J_i \geq 0$ for all i then (6.38) reduces to $J_x = J_y + J_z$, $J_y = J_x + J_z$ or $J_z = J_x + J_y$. These conditions define the phase boundaries between the gapless non-Abelian phase $\mathcal{B}$ and the gapped Toric Code Browne (2014); Kitaev (2003); Resende (2017) phases $\mathcal{A}_i$, as shown in Fig. 6.4. The condition $C = 0$ corresponds to the case where $J_z = 0$. This coupling configuration is located along the base of the large triangle in Fig. 6.4 where the model becomes a set of disentangled one dimensional chains with zero energy gap Kitaev (2001). Therefore, the geometric description of the Kitaev honeycomb model within the $\mathcal{B}$ phase is entirely non-singular and the singular regions coincide with the phase transitions of the model.

In summary, the continuum limit of the generally anisotropic Kitaev honeycomb model describes massless Majorana fermions on a curved spacetime with

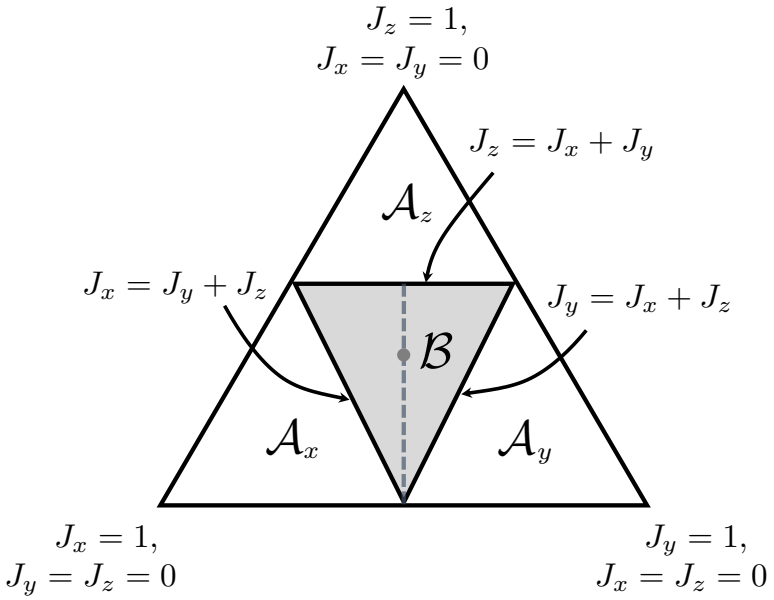

Figure 6.4: The phase diagram of the anisotropic KHLM, where the couplings are normalised as $J_x + J_y + J_z = 1$. The isotropic case with $J_x = J_y = J_z$ is denoted by a dot in the centre of the triangles. The quantum spin liquid phase that supports Majorana fermions, denoted as $\mathcal{B}$, sits in the centre of the diagram. The topological phases $\mathcal{A}_i$ correspond to the Toric Code phase. The singularity condition of the metric (6.38) defines the boundaries between the $\mathcal{A}_i$ and $\mathcal{B}$ phases. The dashed line corresponds to the specific anisotropic change of couplings in the $\mathcal{B}$ phase considered in Section 6.1.3.

torsion proportional to the next to nearest neighbour term. The nearest neighbour terms become the kinetic terms defining non-trivial dreibein. These dreibein define a metric with singularities at the well known phase transitions of the model. Note that although all necessary components are present in (6.35) and (6.36) in order to obtain the connection of space, Ricci scalar, Riemann tensor, etc. these term are not explicitly calculated here.

A possible mass producing term for the generally anisotropic case could be a Kekulé distortion anisotropically modified in a similar way to the K term in (6.16), such that the Fermi points of the model are not shifted. The specific form of such a coupling is not studied here.

Section 6.1.3 studies a specific case of the anisotropic Kitaev honeycomb model in more detail. Section 6.2 then numerically investigates the accuracy of the geometric description of this specific case by observing the response of two point Majorana correlations to variations of the couplings within this regime.

6.1.3 The anisotropic case with $J_x = J_y = 1$ and $0 \leq J_z \leq 2$

This section considers a particular anisotropic case of the Kitaev honeycomb model, where $J_x = J_y = 1$ and $0 \leq J_z \leq 2$. This coupling configuration corresponds to the dotted vertical line in Fig. 6.4. The two points $J_z = 0$ and $J_z = 2$ correspond to phase transitions of the model. This case is referred to as the anisotropic case.

The Metric

By fixing $J_x = J_y = 1$ in (6.29) and (6.31) the continuum limit Hamiltonian of the anisotropic case can be obtained from (6.33) as

$$\begin{aligned} h_{\text{KHLM}} =& \sqrt{12 - 3J_z^2}\gamma^0\gamma^1 p_x - 3J_z\gamma^0\gamma^2 p_y \\ & - KJ_z(4 - J_z^2)^{\frac{3}{2}} i\gamma^1\gamma^2. \end{aligned} \tag{6.39}$$

Using (6.34) the dreibein of the model are given by

$$e_a{}^{\mu} = \begin{pmatrix} 1 & 0 & 0 \\ 0 & \sqrt{12 - 3J_z^2} & 0 \\ 0 & 0 & -3J_z \end{pmatrix}, \quad e^a{}_{\mu} = \begin{pmatrix} 1 & 0 & 0 \\ 0 & \frac{1}{\sqrt{12-3J_z^2}} & 0 \\ 0 & 0 & -\frac{1}{3J_z} \end{pmatrix} \tag{6.40}$$

with the corresponding metric from (6.35)

$$g_{\mu\nu} = \begin{pmatrix} 1 & 0 & 0 \\ 0 & \frac{1}{3J_z^2 - 12} & 0 \\ 0 & 0 & -\frac{1}{9J_z^2} \end{pmatrix}. \tag{6.41}$$

When $J_z = 1$ these equations agree with the isotropic case presented in 6.1.1 for $J = 1$.

Curvature and Torsion

The metric (6.41) is a diagonal metric of a static spacetime taking the form (6.4). Hence, direct substitution of

$$F = \frac{1}{3J_z^2 - 12}, \quad G = -\frac{1}{9J_z^2} \tag{6.42}$$

into the general formula (6.6) yields the Ricci scalar $\tilde{R}$ of the Levi-Civita connection as

$$\begin{aligned}\tilde{R} =& 3\Bigg[\left(-\frac{4}{J_z} + J_z\right) 2\partial_x^2 J_z + \left(\frac{8}{J_z^2} - 1\right) 2(\partial_x J_z)^2 + \left(3\frac{-J_z^4 + 8J_z^2}{(J_z^2-4)^2} + 2\right) J_z \partial_y^2 J_z \\ &+ \left(4\frac{J_z^6 - 5J_z^4 - 12}{(J_z^2-4)^2} + -J_z^4 + 4J_z^2\right) \frac{3}{J_z^2 - 4} (\partial_y J_z)^2\Bigg].\end{aligned} \tag{6.43}$$

It is clear from this messy expression that the Ricci scalar is non-zero and space dependent when J_z is allowed to vary in space. This coupling may be upgraded to a position dependent parameter, varying slowly with respect to the overall magnitude of the couplings J and K, without diminishing the validity of the geometric description of the model as discussed in Section 6.1.1. The Ricci scalar (6.43) fully determines the Riemann tensor of the Levi-Civita connection via the relation (6.8).

From the gap at the Fermi points $\Delta = -KJ_z(4 - J_z^2)^{\frac{3}{2}}$ and equation (6.36) the torsion pseudoscalar and mass are given by

$$\phi = -8KJ_z(4 - J_z^2)^{\frac{3}{2}}, \quad m = 0. \tag{6.44}$$

From (5.87) the torsion pseudoscalar fully determines the components of the torsion and contorsion tensor in the dreibein basis

$$T_{abc} = 2K_{abc} = -\frac{4}{3} KJ_z(4 - J_z^2)^{\frac{3}{2}} \epsilon_{abc}. \tag{6.45}$$

The Ricci scalar of the full model is then given via equation (5.72) as

$$R = \tilde{R} - \frac{8}{3} K^2 J_z^2 (4 - J_z^2)^3. \tag{6.46}$$

Section 6.1.1 showed that the torsion of the isotropic case (6.10) is completely determined by K and is independent of J. On the other hand, in this anisotropic

case, the torsion in (6.45) has a dependence on J_z. This is due to the fact that the K term has been modified as in (6.16) and the next to nearest neighbour interactions now depend on J_z via (6.28). However, the relative scale of the torsion compared to the kinetic terms of the continuum limit is still determined by K and it will vanish if $K = 0$. Hence, the next to nearest neighbour interactions are still the source of torsion in the model, while the kinetic terms are defined by the nearest neighbour interactions. It just so happens that in this special case of the model these two types of interactions are interdependent.

In summary, the continuum limit of this specific case of the anisotropic Kitaev honeycomb model describes massless Majorana fermions on a curved spacetime with torsion proportional to the next to nearest neighbour interaction terms. The nearest neighbour terms become the kinetic terms defining non-trivial dreibein. Note that as in the isotropic case all of the components necessary to obtain the full spacetime connection (5.59) and Riemann tensor (5.71) are provided.

Section 6.2 numerically investigates how faithfully the metric (6.41) predicts the stretching and squeezing of the "*spacial profile*" of the two point Majorana correlations induced by varying the strength of the J_z and K couplings within this regime. What is meant by the spacial profile of these quantities will be discussed in Section 6.2.

6.2 Spatial distribution of quantum correlations

This section numerically studies the Kitaev honeycomb lattice model with periodic boundary conditions and anisotropic J couplings, such that $J_x = J_y = 1$ and $0 \leq J_z \leq 2$. Specifically the accuracy of the effective geometric picture is assessed by comparing the stretching of space predicted by the metric (6.41) to the observed distortions of the two point Majorana correlations of the Hamiltonian of the microscopic model (5.13), with the modified K term given in (6.16). From the correlation strength between two points on the lattice for a particular coupling configuration the correlation strength of these points for any other configuration can be determined by considering the spatial transformation described by the corresponding change of metric.

It is shown that the geometric description of the Kitaev honeycomb model holds very well, particularly for smaller values of K as this is when the correlation length is largest. Hence, the discrete lattice effects become negligible and the behaviour of the model more closely resembles that of the continuous approximation.

Section 6.2.1 determines the specific form of the effective stretching predicted by the metric (6.41). Section 6.2.2 then compares this predicted stretching to the observed distortions of the two point correlations of the Kitaev honeycomb model with different coupling configurations.

6.2.1 Effective Stretching

The metric (6.41) describes how the effective distance of the geometric picture in the x and y direction changes as J_z varies, for the homogeneous anisotropic case where $J_x = J_y = J_z = 1$ and $0 \leq J_z \leq 2$, as in Fig. 6.4. The spacial distance d between two points on the the two dimensional curved space Σ is given by

$$d = \sqrt{-g_{ij}\Delta X^i \Delta X^j}, \tag{6.47}$$

where ΔX^i is the difference in spacial coordinates between each point and g_{ij} are the spatial components of the metric. The principle axes d_x and d_y along the x and y directions, respectively, are deformed according to the relations

$$d_x = \sqrt{-g_{xx}} = \sqrt{3}J_z, \quad d_y = \sqrt{-g_{yy}} = \sqrt{4 - J_z^2}. \tag{6.48}$$

If points on Σ are portrayed as fixed in space, shapes will appear to deform in the inverse way to the change in effective distance. Take a line l of length d_l between two points A and B on the surface Σ. If the effective distance between these points is scaled by a factor of a the length of the line will *appear* to scale by a factor of a^{-1} to keep the effective length of the line fixed. This is the case in the numerical investigation presented in Section 6.2.2. The lattice sites are portrayed as fixed in space, while the effective distance between them varies with J_z.

Section 6.2.2 investigates how faithfully the deformation of the spacial profiles of two-point Majorana correlations Kitaev (2006) are described by the ratio

$$\frac{d_x}{d_y} = \frac{\sqrt{3}J_z}{\sqrt{4 - J_z^2}}. \tag{6.49}$$

The spacial profiles are approximately circular at $J_z = 1$ and are deformed into ellipses when $J_z \neq 1$. As J_z decreases the ellipse appears to stretch and contract along the x and y axis, respectively, and vice versa as J_z increases.

6.2.2 Two Point Quantum Correlations

Two point Majorana correlations are the expectation value of a product of two Majorana operators at different sites with respect to the ground state $|\psi_0\rangle$, i.e. $i\langle c_i c_j\rangle = \langle\psi_0| ic_i c_j |\psi_0\rangle$. They are an important quantity as any other property of the model can be deduced from them as the model is effectively free Meichanetzidis *et al.* (2018). As the system is gapped the two-point correlations will decrease exponentially fast with respect to the distance $|\boldsymbol{r}_i - \boldsymbol{r}_j|$, where $\boldsymbol{r}_i$ is the position of site i. The correlation matrix of the Kitaev honeycomb model is calculated via exact diagonalisation of the Hamiltonian (5.13) in Section 5.1.6 as (5.56). Taking the i-th row or column of the correlation matrix gives a discrete spacial profile of the two-point correlations of each site with respect to a central reference site i, as shown in Fig. 6.5(a).

To study the effect of varying J_z on this spacial profile a continuous approximation is produced by replacing the two point correlation data at each lattice point with a two dimensional Gaussian centred at the site,

$$i\langle c_j c(\boldsymbol{r})\rangle = \sum_i i\langle c_j c_i\rangle\, \delta(\boldsymbol{r} - \boldsymbol{r}_j) \to \sum_i \frac{i\langle c_j c_i\rangle}{2\pi\epsilon} e^{-\frac{|\boldsymbol{r}-\boldsymbol{r}_j|^2}{2\epsilon}}\,, \tag{6.50}$$

where ϵ is taken to be of similar magnitude as to the lattice spacing so that the Gaussians of neighbouring sites overlap. Fig. 6.5 illustrates this substitution. This continuous approximation reduces the discrete lattice effects and allows the stretching and squeezing of the correlations predicted by (6.49) to be measured.

From the continuous spacial profile of the correlations the set of points is numerically identified where $i\langle c_0 c(\boldsymbol{r})\rangle \approx 10^{-3}$ for some reference site 0. This 'boundary' line is drawn for the correlations at the isotropic point of the model in Fig. 6.5(b). At the isotropic point the boundary is approximately circular. When J_z is increased above the isotropic point $J_z > 1$ the boundary should be stretched in the x direction and vice versa when decreased to $J_z < 1$. It is worth noticing that as the two point correlations are local they are strongly influenced

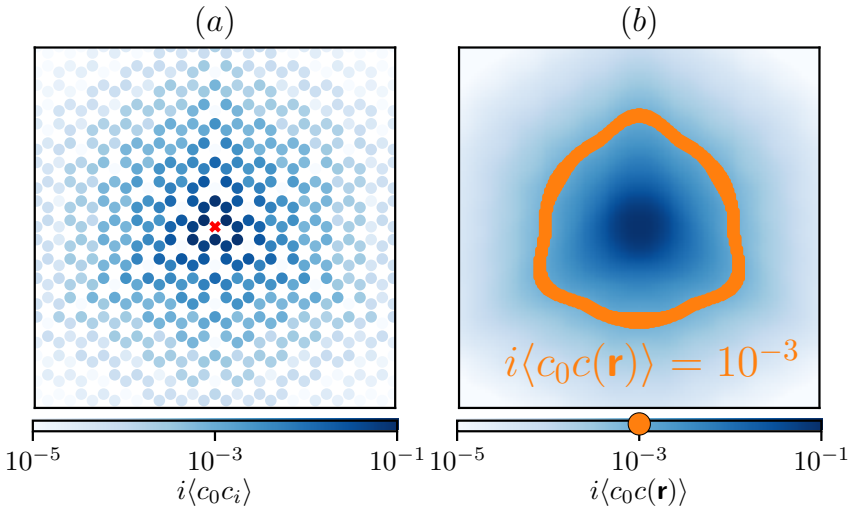

Figure 6.5: The two-point correlations and their continuous profile. (a) The two-point correlations $i\langle c_0 c_i\rangle$ between each site i and a central reference site 0, marked with a red cross. (b) A continuous approximation $i\langle c_0 c(\boldsymbol{r})\rangle$ of the two-point correlations is constructed using two dimensional Gaussians centred on each lattice site, as described by (6.50). The size and shape of the correlations are characterised by finding the set of points where $i\langle c_0 c(\boldsymbol{r})\rangle \approx 10^{-3}$, as illustrated. Notice that even for large system sizes the hexagonal geometry of the lattice influences the spatial distribution of the correlations. The model parameters used here are $J_x = J_y = J_z = 1$, system size 36×36, $K = 0.1$ and $\epsilon = 1$.

by the lattice structure of the system. Hence, even though the correlations in the continuum limit at the isotropic point are expected to be rotationally invariant, the honeycomb lattice structure is still evident in the continuous approximation, even for large system sizes. Fig. 6.6 demonstrates how the correlation length and the rotational invariance of the continuous profile of the correlations both decrease with increasing K.

To compare the changing shape of the boundary to the distortion predicted by the metric (6.41) the ratio between the height and width of the boundary w_y/w_x is compared to the ratio of the principle axes of the ellipse d_x/d_y, given in (6.49). At the isotropic point the width and height of the boundary are approximately circular, with $w_y/w_x \approx 1$. Fig. 6.7 plots the comparison of w_y/w_x

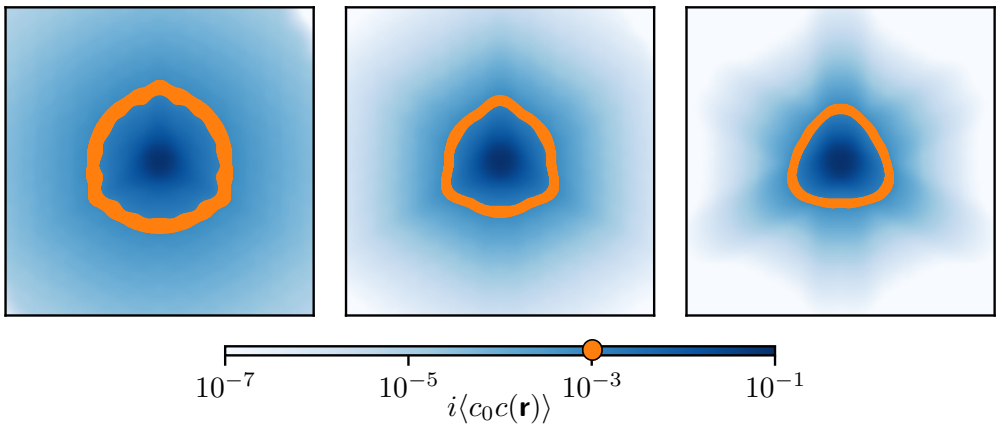

Figure 6.6: The rotational invariance of the boundary and the correlation length decrease, while the impact of discrete lattice effects on the continuous profile $i\langle c_0 c(\boldsymbol{r})\rangle$ become more significant with increasing $K = 0.05, 0.1, 0.15$ (Left, Middle, Right).

to d_x/d_y for different values of J_z. An increase (decrease) in J_z corresponds to a decrease (increase) in the effective distance d_y between lattice sites along the y axis, resulting in stronger (weaker) correlations along that axis. This results in an apparent stretching (squeezed) of the correlations in that direction, i.e. an increase (decrease) in w_y/w_x. The ratio w_y/w_x converges to d_x/d_y with decreasing K.

Figs. 6.6 and 6.7 both demonstrate a closer agreement between the microscopic model and the Riemann-Cartan geometric description with decreasing K. This is due to an increase in the correlation length, seen in Fig. 6.6. When the correlation length becomes large compared to the lattice spacing discrete lattice effects become negligible and the correlations approximate the behaviour of those in a continuous system.

The effective geometric description of the Kitaev honeycomb model in terms of the metric is found to be a faithful representation of the distortion experienced by the correlations of the system. As the metric is used to define many other geometric quantities, such as the curvature, these are expected to be faithfully reproduced as well. This is an interesting area of investigation for future work.

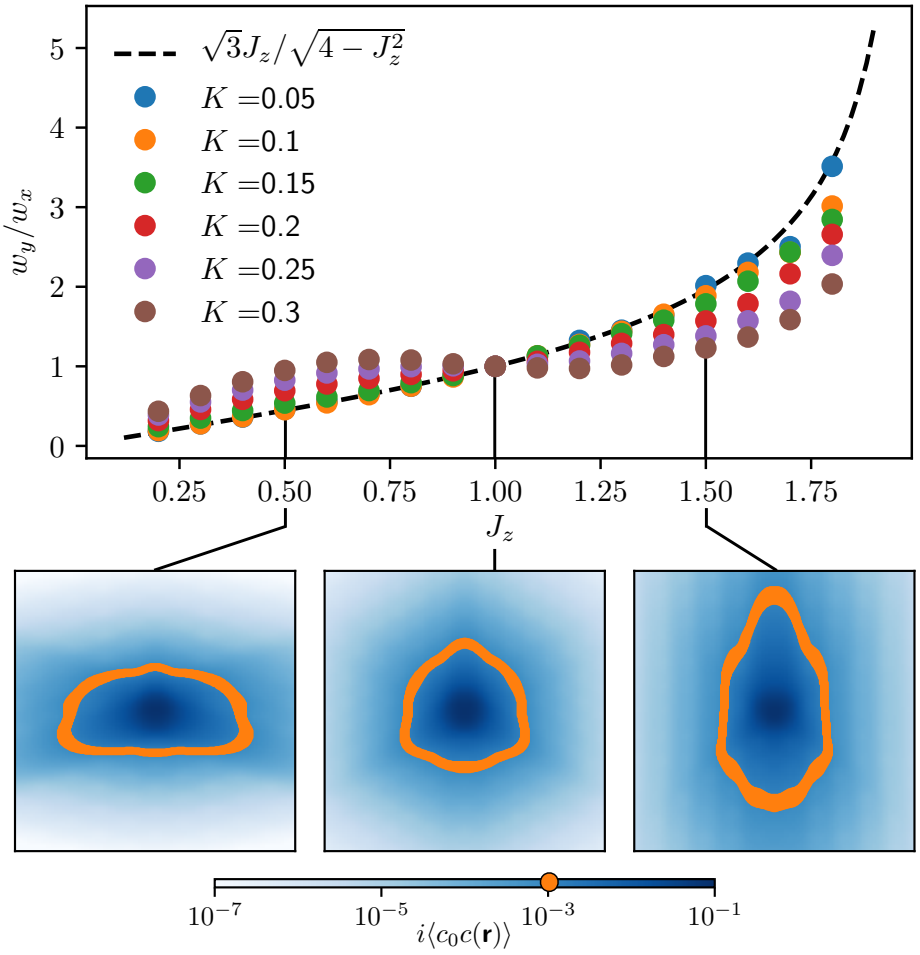

Figure 6.7: Verifying the metric from the continuous approximation of the correlations. The dots in the main panel plot the ratio between the height and width of the 'boundary' w_y/w_x for $J_x = J_y = 1$, $\epsilon = 1$, system size 36×36 and a range of K. Also plotted with a dashed line is the theoretically predicted ratio $d_x/d_y = \sqrt{3}J_z/\sqrt{4-J_z^2}$ from Eq. (6.49). The numerical data converges to the theoretical line as K decreases. Below are illustrative examples of the boundaries at various J_z and $K = 0.1$. At the isotropic point, $J_z = 1$, the ratio is $w_y/w_x = 1$. As J_z deviates from the isotropic point the ratio w_y/w_x can become larger or smaller than one.

6.3 Conclusions

This chapter has expanded upon the known result that the low energy limit, or continuum limit, of the Kitaev honeycomb lattice model is described by massless Majorana fermions obeying the Dirac Hamiltonian embedded in a Minkowski spacetime. By investigating the model in a variety of coupling regimes it was found that the continuum limit could produce a non-trivial Riemann-Cartan geometry with curvature and torsion defined by the non-trivial dreibein $e_a{}^\mu$ and spacetime connection $\Gamma^\rho{}_{\mu\nu} = \tilde{\Gamma}^\rho{}_{\mu\nu} + K^\rho{}_{\mu\nu}$. These quantities are in turn completely determined by the coupling parameters of the Kitaev honeycomb model. The dreibein define a metric, which describes a non-trivial stretching of space. This stretching was numerically verified by studying the response of two point Majorana correlations to variations of the metric. The couplings of the model are upgraded to space-dependent parameters which vary slowly compared to the overall magnitude of the couplings. This results in a more general Riemann-Cartan continuum limit than would otherwise be obtained with contributions to curvature from both the nearest neighbour $\{J_i\}$ and next to nearest neighbour $\{K_i\}$ couplings.

It was shown theoretically that the single-particle Hamiltonian of a massless Majorana field in a Riemann-Cartan spacetime h_{RC}, (5.90), can be identified with the continuum limit Hamiltonian of the Kitaev honeycomb lattice model h_{KHLM}, (6.32), with general space dependent $\{J_i\}$ and $\{K_i\}$ couplings, where the later are anisotropically modified to depend on the former as in (6.28). The nearest neighbour terms of the microscopic Hamiltonian become kinetic terms in h_{KHLM} while the next to nearest neighbour terms generate an energy gap at the Fermi points. Via direct comparison of h_{KHLM} and h_{RC} the kinetic terms are identified with the non-trivial dreibein while the gap producing terms are identified with a non-trivial torsion $T^\rho{}_{\mu\nu}$ or contorsion $K^\rho{}_{\mu\nu}$ in the Riemann-Cartan theory. From this the metric $g_{\mu\nu} = e^a{}_\mu e^b{}_\nu \eta_{ab}$ is fully determined in terms of $\{J_i\}$. The Levi-Civita connection and contorsion tensor of the total connection $\Gamma^\rho{}_{\mu\nu} = \tilde{\Gamma}^\rho{}_{\mu\nu} + K^\rho{}_{\mu\nu}$ are determined by $\{J_i\}$ and $\{K_i\}$, respectively. These relations are sufficient to determine the curvature $R^\rho{}_{\mu\nu\sigma}$ of the Riemann-Cartan theory in terms of the couplings of the microscopic model.

Even for the simple case of homogeneous isotropic couplings, where $J_x = J_y = J_z = J$, the continuum limit has trivial dreibein, but a non-trivial torsion yielding a non-trivial spacetime connection and curvature which depend on the parameter K. If the coupling parameters are take to be inhomogeneous the dreibein become non-trivial and the spacetime connection and curvature now also have a dependence on J. Although this case has been well studied previously the superconducting gap term was never identified with torsion in Minkowski spacetime Kitaev (2006); Pachos (2012). When the torsion is dominant the system is a topological superconductor in class D Chiu *et al.* (2016). It was also demonstrated that the Majorana spinors can be given a non-zero mass by introducing a Kekulé distortion to the model. When the mass term is dominant over the torsion the system is in class BDI. This topological phase transition was studied numerically and found to take the form predicted by the geometric description of the model.

The metric (6.41) of the specific anisotropic coupling configuration, where $J_x = J_y = 1$ and $0 \leq J_z \leq 2$, describes a non-trivial distortion of space. This stretching of space is shown numerically in Fig. 6.7 to accurately describe the response of the spacial profile of two point Majorana correlations to varying J_z. The accuracy of the geometric description clearly improves with increasing correlation length. This can also be seen from Fig. 6.6. As expected, in the limit of large correlation length discrete lattice effects become negligible and the model strongly resembles its continuous description.

This work verifies that Majorana spinors obeying the Dirac equation embedded in a Riemann-Cartan spacetime can faithfully describe the microscopic Kitaev honeycomb lattice model. Thus demonstrating the power such field theoretic descriptions have in predicting the behaviour of these microscopic models.

Chapter 7

Conclusions

This thesis has studied multiple equivalent representations of different topological systems focusing on their individual uses and benefits in terms of solvability and ability to provide accurate descriptions of the behaviour of physical observables. This chapter concludes the thesis by reviewing the original results of Chapters 3, 4 and 6. Possible future areas of research are then discussed.

In order to quantify the role of interactions in topological states of matter Chapter 3 calculated the interaction distance $D_{\mathcal{F}}$ of the entanglement spectra of a wide range of Abelian and non-Abelian $(2+1)-$dimensional string-nets and $(3+1)-$dimensional Walker-Wang models. Specifically, partitions of all eigenstates of $\mathbb{Z}_N$ Abelian string-nets and Walker-Wang models are studied. It was shown that the interaction distance of these Abelian models depends not only on the group $\mathbb{Z}_N$, but also on the size of the partition boundary $|\partial A|$. Abelian string-nets and Walker-Wang models with the same N and $|\partial A|$ are found to have equivalent $D_{\mathcal{F}}$ for all eigenstates regardless of the geometry and topology of the partition.

One focus of this investigation was identifying states with $D_{\mathcal{F}} = 0$ that have free fermion representations. The class of $\mathbb{Z}_{2^n}$ models, where $n \in \mathbb{N}$, were identified as having $D_{\mathcal{F}} = 0$ for all $|\partial A|$. Therefore, the states of these models are representable in terms of free fermions. These findings were used in Chapter 4 when discussing the signatures of the $\mathbb{Z}_2$ surface and toric codes, equivalent to the $\mathbb{Z}_2$ string-net, which suggest they have representations in terms of free

fermions. By studying the distribution of interaction distance $P(D_{\mathcal{F}})$ for a variety of partition sizes $|\partial A|$ it was demonstrated that not only do all partitions of $\mathbb{Z}_N$ string-nets and Walker-Wang models, with $N \neq 2^n$, have $D_{\mathcal{F}} \neq 0$, but they also maximise $D_{\mathcal{F}}$ for a large fraction of partitions.

It was shown that for non-Abelian Walker-Wang models the topology of the boundary becomes relevant to the calculation of $D_{\mathcal{F}}$. This is due to the entanglement spectrum encoding information about the non-trivial braiding of non-Abelian anyonic charges. All boundaries in $2+1$ dimensions are topologically trivial, so this has no effect on string-nets. The interaction distance was found numerically to be $D_{\mathcal{F}} \neq 0$ for the non-Abelian $SU(2)_k$ string-nets and Walker-Wang models for levels $2 \leq k \leq 20$, boundary size $|\partial A| = 3$ and any boundary topology. This seems to suggest that interactions are necessary for the emergence of excitations with non-Abelian anyonic statistics.

Chapter 4 presents unitary transformations $\mathcal{U}_S$ and $\mathcal{U}_T$ from the $\mathbb{Z}_2$ surface and toric code, respectively to equivalent fermion models. Analysis of the interaction distance of the eigenstates of the $\mathbb{Z}_2$ string-net in Chapter 3 along with the thermal interaction distance $D_{\mathcal{F}}^{\text{th}}$ of their energy spectra, discussed in Chapter 4, shows that the individual states and energy spectra are free. However, an investigation of the stabilizer groups structure of the models showed that the fermionic representation of the toric code must also include two interacting fermionic parity operator to ensure that the group structure is preserved and excitations are created in pairs.

The transformations $\mathcal{U}_S$ and $\mathcal{U}_T$ were presented explicitly for any system size. It was demonstrated that the e and m anyonic excitations of the codes, created at black and white plaquettes, respectively, map to excitations of distinct black and white dynamical local modes of the fermionic models. In the case of the toric code, excitations of a particular black and white plaquette are mapped to excitations of the two parity operators with support on all black and white fermion modes, respectively. This is necessary in order to give rise to the non-trivial topological order Yao & Qi (2010). The logical operators of the codes were mapped to fermionic zero mode operators. It was also demonstrated that although all states and the energy spectra are free, some non-local interactions

acting on both the dynamic and zero modes were still necessary to encode the anyonic statistics of the excitations.

These mappings provide an intuitive and unique understanding of the origins of the exotic statistics of these topological models. Extending the family of mappings $\mathcal{U}$ to other topological models, such as $\mathbb{Z}_{2^n}$ string-nets and Walker-Wang models, could provide valuable insight into the emergence of exotic statistics in these systems. This would require a larger and more complete investigation of the interaction distance, including thermal interaction distance and an analysis of the group structure Hung & Wan (2012); Walker & Wang (2012) of a wide range of topological phases of matter. This could prove useful in identifying models with possible fermionic representations, which may be employed to solve these quantum Hamiltonians.

Chapter 6 showed analytically that the low energy limit, or continuum limit, Hamiltonian of the microscopic Kitaev honeycomb lattice model h_{KHLM} can be identified with the single-particle Hamiltonian of a massless Majorana field in a non-trivial Riemann-Cartan spacetime h_{RC} with curvature and torsion. The curvature and torsion, defined by the non-trivial dreibein ${e_a}^{\mu}$ and spacetime connection ${\Gamma^{\rho}}_{\mu\nu} = {\tilde{\Gamma}^{\rho}}_{\mu\nu} + {K^{\rho}}_{\mu\nu}$ are associated to the general space-dependent nearest neighbour $\{J_i\}$ and next to nearest neighbour $\{K_i\}$ couplings of the Kitaev honeycomb model, which vary slowly compared to their overall magnitude. The $\{K_i\}$ couplings are modified from the usual next to nearest neighbour terms to depend on the $\{J_i\}$ couplings.

The nearest neighbour $\{J_i\}$ terms are shown, by direct comparison of h_{KHLM} and h_{RC}, identified with kinetic terms defining the dreibein and a metric, which describes a non-trivial distortion of space. This stretching of space was numerically verified for the specific anisotropic coupling configuration, where $J_x = J_y = 1$ and $0 \leq J_z \leq 2$, by studying the response of two point Majorana correlations to variations of the metric. The accuracy of the geometric description was shown to improve with decreasing K, or equivalently increasing correlation length. It was demonstrated that in the limit of large correlation length the discrete lattice effects become negligible and the model strongly resembles the continuous geometric description. The next to nearest neighbour $\{K_i\}$ terms are shown to generate an energy gap at the Fermi points of the continuous description h_{KHLM}.

This equates to a non-trivial torsion $T^{\rho}_{\ \mu\nu}$ or contorsion $K^{\rho}_{\ \mu\nu}$ in h_{RC}. The curvature of the Riemann-Cartan theory then depends on both the $\{J_i\}$ and $\{K_i\}$ couplings of the microscopic model. It was also demonstrated that introducing a Kekulé distortion produces a gap in h_{RC} due to a non-zero mass term. The phase transition between the torsion dominated class D Chiu *et al.* (2016) phase and the mass dominated class BDI phase was shown numerically to agree with the form predicted by the geometric description of the model.

This field theoretic description could be used to investigate a variety of properties of the microscopic model. Energy-momentum currents and momentum densities due to effective curvature in the geometric description of a lattice model of superconducting complex fermions were studied analytically in Golan & Stern (2018). These quantities could be investigated numerically in the Kitaev honeycomb model in terms of specific coupling configurations corresponding to non-trivial curvature. The geometric description of superconductors used to obtain the thermal transport coefficients from response theory as employed in Luttinger (1964) can also be realised in the Kitaev honeycomb model with a perturbation of the couplings around the isotropic and homogeneous configuration.

Another direction of investigation is the study of chiral gauge fields such as those considered in graphene in Jackiw & Pi (2007). In fact fluctuations of the Kitaev model's $\mathbb{Z}_2$ gauge field as well as the addition of twists Petrova *et al.* (2013, 2014); Willans *et al.* (2011) have been shown in Horner *et al.* (2020) to produce chiral gauge fields and hence provide a more complete quantum field theory description of the model. Fluctuations of these chiral gauge fields in the continuum limit are shown to produce Majorana zero modes in the discrete model.

The Kitaev honeycomb model with a time-dependent Hamiltonian Kaib *et al.* (2019) could also be probed using the formalism developed here by upgrading the static spacetime (5.83) to a dynamical spacetime. Alternatively, the response of the model to time-dependent geometric perturbations including quenches Liu *et al.* (2018) could be considered.

The methods and ideas presented here are not restricted to the Kitaev honeycomb model. Geometric descriptions of other topologically ordered systems are already being investigated de Juan *et al.* (2013); Golan & Stern (2018); Jackiw &

Pi (2007); Wagner *et al.* (2019). These types of geometric representations can potentially provide accurate descriptions of the behaviour of physical observables. It will be interesting to see where these approximations break down and how much they can tell us about the properties of these complex microscopic models.

Experiments have found that some but not all features of the Kitaev honeycomb model are recognised in experimentally realisable materials, such as complex iridium oxides Chaloupka *et al.* (2010); Choi *et al.* (2012); Jackeli & Khaliullin (2009) or ruthenium chloride Banerjee *et al.* (2016). Fully realising topologically ordered materials experimentally is an open problem and would be a huge step towards achieving topological quantum computation. It will be exciting to see how topological materials may be utilised in the development of quantum technologies in the near and distant future.

References

Abanov, A.G. & Gromov, A. (2014). Electromagnetic and gravitational responses of two-dimensional noninteracting electrons in a background magnetic field. *Phys. Rev. B*, **90**, 014435. 5

Anderson, P.W. (1987). The resonating valence bond state in la2cuo4 and superconductivity. *Science*, **235**, 1196–1198. 2

Arute, F., Arya, K. & Martinis, J.M. (2019). Quantum supremacy using a programmable superconducting processor. *Nature*, **574**, 505–510. 1

Avron, J.E., Seiler, R. & Zograf, P.G. (1995). Viscosity of quantum hall fluids. *Phys. Rev. Lett.*, **75**, 697–700. 5

Balents, L. (2010). Spin liquids in frustrated magnets. *Nature*, **464**, 199–208. 76

Banerjee, A., Bridges, C., Yan, J.Q., Aczel, A., Li, L., Stone, B., Granroth, G., Lumsden, M., Yiu, Y., Knolle, J., Bhattacharjee, S., Kovrizhin, D., Moessner, R., Tennant, D., Mandrus, D. & Nagler, S. (2016). Proximate kitaev quantum spin liquid behaviour in a honeycomb magnet. *Nature Materials*, **15**, 733–740. 5, 118

Bombin, H. & Martin-Delgado, M.A. (2007). Optimal resources for topological 2d stabilizer codes: Comparative study. *Phys. Rev. A 76, 012305*. 3, 14, 36, 45

Bonderson, P. (2007). *Non-Abelian Anyons and Interferometry*. Ph.D. thesis, California Institute of Technology. 8, 9, 33, 76

Bradlyn, B. & Read, N. (1992). Quantum symmetries in discrete gauge theories. *Phys. Lett. B 280 (1992) 63-70*. 21

Bradlyn, B. & Read, N. (2015). Low-energy effective theory in the bulk for transport in a topological phase. *Phys. Rev. B*, **91**, 125303. 5

Bravyi, S. (2004). Lagrangian representation for fermionic linear optics. *arXiv:quant-ph/0404180*. 42

Bravyi, S., Englbrecht, M., Konig, R. & Peard, N. (2017). Correcting coherent errors with surface codes. *arXiv:1710.02270 [quant-ph]*. 3, 14, 36, 42, 45, 60

Brown, B.J., Son, W., Kraus, C.V., Fazio, R. & Vedral, V. (2011). Generating topological order from a two-dimensional cluster state using a duality mapping. *New J. Phys. 13 065010*. 4

Brown, B.J., Loss, D., Pachos, J.K., Self, C.N. & Wootton, J.R. (2016). Quantum memories at finite temperature. *Rev. Mod. Phys. 88, 045005*. 3, 21

Brown, B.J., Laubscher, K., Kesselring, M.S. & Wootton, J.R. (2017). Poking holes and cutting corners to achieve clifford gates with the surface code. *Phys. Rev. X 7, 021029*. 3

Browne, D. (2014). Lectures on topological codes and quantum computation. 3, 14, 15, 21, 24, 102

Bullivant, A. & Pachos, J.K. (2016). Entropic manifestations of topological order in three dimensions. *Phys. Rev. B*, **93**, 125111. 12, 14, 27, 28, 38

Can, T., Laskin, M. & Wiegmann, P. (2014). Fractional quantum hall effect in a curved space: Gravitational anomaly and electromagnetic response. *Phys. Rev. Lett.*, **113**, 046803. 5

Carroll, S. (2003). *Spacetime and Geometry: An Introduction to General Relativity*. Pearson, 1st edn. 5, 6, 61, 78

Castro Neto, A.H., Guinea, F., Peres, N.M.R., Novoselov, K.S. & Geim, A.K. (2009). The electronic properties of graphene. *Rev. Mod. Phys.*, **81**, 109–162. 68

Chaloupka, J., Jackeli, G. & Khaliullin, G. (2010). Kitaev-heisenberg model on a honeycomb lattice: Possible exotic phases in iridium oxides A_2iro_3. *Phys. Rev. Lett.*, **105**, 027204. 5, 118

Chiu, C.K., Teo, J.C.Y., Schnyder, A.P. & Ryu, S. (2016). Classification of topological quantum matter with symmetries. *Rev. Mod. Phys.*, **88**, 035005. 76, 96, 113, 117

Choi, S.K., Coldea, R., Kolmogorov, A.N., Lancaster, T., Mazin, I.I., Blundell, S.J., Radaelli, P.G., Singh, Y., Gegenwart, P., Choi, K.R., Cheong, S.W., Baker, P.J., Stock, C. & Taylor, J. (2012). Spin waves and revised crystal structure of honeycomb iridate na_2iro_3. *Phys. Rev. Lett.*, **108**, 127204. 5, 118

de Juan, F., Cortijo, A. & Vozmediano, M. (2010). Dislocations and torsion in graphene and related systems. *Nucl. Phys. B*, **828**, 625. 5

de Juan, F., Mañes, J.L. & Vozmediano, M.A.H. (2013). Gauge fields from strain in graphene. *Phys. Rev. B*, **87**, 165131. 5, 117

Dennis, E., Kitaev, A., Landahl, A. & Preskill, J. (2002). Topological quantum memory. *Journal of Mathematical Physics*, **43**, 4452–4505. 1

DiVincenzo, D.P. & Mele, E.J. (1984). Self-consistent effective-mass theory for intralayer screening in graphite intercalation compounds. *Phys. Rev. B*, **29**, 1685–1694. 68

Dusuel, S., Schmidt, K.P. & Vidal, J. (2008). Creation and manipulation of anyons in the kitaev model. *Physical Review Letters*, **100**. 76

Fan, Z. & de Garis, H. (2010). Braid matrices and quantum gates for ising anyons topologicalquantum computation. *Eur. Phys. J. B 74, 419 (2010)*. 8

Farjami, A. (2020). Free fermion representation of the topological surface code. *Eur. Phys. J. B*, **93**. 3, 4

Farjami, A., Horner, M.D., Self, C.N., Papić, Z. & Pachos, J.K. (2020). Geometric description of the kitaev honeycomb lattice model. *Phys. Rev. B*, **101**, 245116. 3, 6

Fowler, A.G., Mariantoni, M., Martinis, J.M. & Cleland, A.N. (2012). Surface codes: Towards practical large-scale quantum computation. *Phys. Rev. A 86, 032324*. 3

Gladchenko, S., Olaya, D., Dupont-Ferrier, E., Doucot, B., Ioffe, L.B. & Gershenson, M.E. (2009). Superconducting nanocircuits for topologically protected qubits. *Nature Physics 5, 48-53*. 3

Golan, O. & Stern, A. (2018). Probing topological superconductors with emergent gravity. *Phys. Rev. B*, **98**, 064503. 5, 89, 94, 117

Gromov, A. & Abanov, A.G. (2014). Density-curvature response and gravitational anomaly. *Phys. Rev. Lett.*, **113**, 266802. 5

Gromov, A. & Son, D.T. (2017). Bimetric theory of fractional quantum hall states. *Phys. Rev. X*, **7**, 041032. 5

Gromov, A., Cho, G.Y., You, Y., Abanov, A.G. & Fradkin, E. (2015). Framing anomaly in the effective theory of the fractional quantum hall effect. *Phys. Rev. Lett.*, **114**, 016805. 5

Haldane, F.D.M. (2009). "Hall viscosity" and intrinsic metric of incompressible fractional Hall fluids. *ArXiv e-prints*. 5

Haldane, F.D.M. (2011). Geometrical description of the fractional quantum hall effect. *Phys. Rev. Lett.*, **107**, 116801. 5

Hamma, A., Cincio, L., Santra, S., Zanardi, P. & Amico, L. (2013). Local response of topological order to an external perturbation. *PhysRevLett.110.210602*. 3

Hehl, F. & Datta, B. (1971). Nonlinear spinor equation and asymmetric connection in general relativity. *Journal of Mathematical Physics*, **12**, 1334. 5

Horner, M.D., Farjami, A. & Pachos, J.K. (2020). Equivalence between vortices, twists and chiral gauge fields in kitaev's honeycomb lattice model. 117

Hou, C.Y., Chamon, C. & Mudry, C. (2007). Electron fractionalization in two-dimensional graphenelike structures. *Phys. Rev. Lett.*, **98**, 186809. 95

Hughes, T.L., Leigh, R.G. & Fradkin, E. (2011). Torsional response and dissipationless viscosity in topological insulators. *Phys. Rev. Lett.*, **107**, 075502. 5

Hung, L.Y. & Wan, Y. (2012). String-net models with Z_N fusion algebra. *Phys. Rev. B*, **86**, 235132. 116

Ivanov, D.A. (2001). Non-abelian statistics of half-quantum vortices in p-wave superconductors. *Phys. Rev. Lett.*, **86**, 268–271. 2, 5

Jackeli, G. & Khaliullin, G. (2009). Mott insulators in the strong spin-orbit coupling limit: From heisenberg to a quantum compass and kitaev models. *Phys. Rev. Lett.*, **102**, 017205. 5, 118

Jackiw, R. & Pi, S.Y. (2007). Chiral gauge theory for graphene. *Phys. Rev. Lett.*, **98**, 266402. 117

Jackiw, R. & Rossi, P. (1981). Zero modes of the vortex-fermion system. *Nuclear Physics B*, **190**, 681 – 691. 96

Jamadagni, A., Weimer, H. & Bhattacharyya, A. (2018). Robustness of topological order in the toric code with open boundaries. *Phys. Rev. B 98, 235147*. 4

Jentschura, U.D. (2012). Dirac hamiltonian with imaginary mass and induced helicity-dependence by indefinite metric. *J.Mod.Phys.*, **3**, 887–894. 96

Kaib, D.A.S., Winter, S.M. & Valenti, R. (2019). Kitaev honeycomb models in magnetic fields: Dynamical response and hidden symmetries. *Phys. Rev. B*, **100**, 144445. 117

Katanaev, M. & Volovich, I. (1992). Theory of defects in solids and three-dimensional gravity. *Annals of Physics*, **216**, 1 – 28. 5

Kitaev, A. (2003). Fault-tolerant quantum computation by anyons. *Annals of Physics*, **303**, 2 – 30. 3, 14, 15, 36, 45, 76, 102

Kitaev, A. (2006). Anyons in an exactly solved model and beyond. *Annals of Physics*, **321**, 2 – 111, january Special Issue. 2, 4, 5, 36, 61, 62, 63, 75, 76, 102, 107, 113

Kitaev, A. & Laumann, C. (2009). Topological phases and quantum computation. *arXiv:0904.2771 [cond-mat.mes-hall]*. 3

Kitaev, A.Y. (2001). Unpaired majorana fermions in quantum wires. *Physics-Uspekhi*, **44**, 131. 102

Klevtsov, S. & Wiegmann, P. (2015). Geometric adiabatic transport in quantum hall states. *Phys. Rev. Lett.*, **115**, 086801. 5

Knolle, J. & Moessner, R. (2019). A field guide to spin liquids. *Annual Review of Condensed Matter Physics*, **10**, 451–472. 76

Lahtinen, V. & Pachos, J.K. (2009a). Non-abelian statistics as a berry phase in exactly solvable models. *New Journal of Physics*, **11**, 093027. 39

Lahtinen, V. & Pachos, J.K. (2009b). Non-abelian statistics as a berry phase in exactly solvable models. *New J. Phys.*, **11**, 093027. 75, 76

Lahtinen, V. & Pachos, J.K. (2010). Topological phase transitions driven by gauge fields in an exactly solvable model. *Phys. Rev. B*, **81**, 245132. 5, 75

Lahtinen, V., Kells, G., Carollo, A., Stitt, T., Vala, J. & Pachos, J.K. (2008). Spectrum of the non-abelian phase in kitaev's honeycomb lattice model. *Annals of Physics*, **323**, 2286. 5

Lahtinen, V., Ludwig, A.W.W., Pachos, J.K. & Trebst, S. (2012). Topological liquid nucleation induced by vortex-vortex interactions in kitaev's honeycomb model. *Phys. Rev. B*, **86**, 075115. 5, 75

Leinaas, J.M. & Myrheim, J. (1977). On the theory of identical particles. *Il Nuovo Cimento B (1971-1996)*, **37**, 1–23. 2

Levin, M. & Wen, X.G. (2003). Fermions, strings, and gauge fields in lattice spin models. *Phys. Rev. B 67, 245316*. 4

Levin, M.A. & Wen, X.G. (2005). String-net condensation: A physical mechanism for topological phases. *Phys. Rev. B*, **71**, 045110. 3, 24, 26, 32

Li, H. & Haldane, F.D.M. (2008). Entanglement spectrum as a generalization of entanglement entropy: Identification of topological order in non-abelian fractional quantum hall effect states. *Phys. Rev. Lett.*, **101**, 010504. 27, 30

Lieb, E.H. (1994). Flux phase of the half-filled band. *Phys. Rev. Lett.*, **73**, 2158–2161. 68

Lieb, E.H., Schultz, T. & Mattis, D. (1961). Two soluble models of an antiferromagnetic chain. *Annals of Physics*, **16**, 407–466. 29

Liu, Z., Gromov, A. & Papić, Z. (2018). Geometric quench and nonequilibrium dynamics of fractional quantum hall states. *Phys. Rev. B*, **98**, 155140. 117

Luttinger, J.M. (1964). Theory of thermal transport coefficients. *Phys. Rev.*, **135**, A1505–A1514. 117

Meichanetzidis, K., Turner, C.J., Farjami, A., Papić, Z. & Pachos, J.K. (2018). Free-fermion descriptions of parafermion chains and string-net models. *Phys. Rev. B*, **97**, 125104. 3, 28, 30, 35, 41, 43, 60, 108

Mong, R.S.K., Clarke, D.J., Alicea, J., Lindner, N.H., Fendley, P., Nayak, C., Oreg, Y., Stern, A., Berg, E., Shtengel, K. & Fisher, M.P.A. (2014). Universal topological quantum computation from a

superconductor-abelian quantum hall heterostructure. *Phys. Rev. X*, **4**, 011036. 1, 8, 14

Nakahara, M. (2003). *Geometry, Topology and Physics*. Taylor & Francis Group, 2nd edn. 5, 6, 61, 78, 83

Nasu, J. & Motome, Y. (2015). Thermodynamics of chiral spin liquids with abelian and non-abelian anyons. *Phys. Rev. Lett.*, **115**, 087203. 5

Nasu, J., Udagawa, M. & Motome, Y. (2014). Vaporization of kitaev spin liquids. *Phys. Rev. Lett.*, **113**, 197205. 5

Nasu, J., Udagawa, M. & Motome, Y. (2015). Thermal fractionalization of quantum spins in a kitaev model: Temperature-linear specific heat and coherent transport of majorana fermions. *Phys. Rev. B*, **92**, 115122. 5

Nielsen, M. (2005). The fermionic canonical commutation relations and the jordan-wigner transform. 46, 55

Nielsen, M.A. & Chuang, I.L. (2011). *Quantum Computation and Quantum Information: 10th Anniversary Edition*. Cambridge University Press, New York, NY, USA, 10th edn. 2

Nussinov, Z. & Ortiz, G. (2009). A symmetry principle for topological quantum order. *Ann. Phys. 324, 977*. 4

Otten, D., Roy, A. & Hassler, F. (2019). Dynamical structure factor in the non-abelian phase of the kitaev honeycomb model in the presence of quenched disorder. *Phys. Rev. B*, **99**, 035137. 76

Pachos, J.K. (2012). *Introduction to Topological Quantum Computation*. Cambridge University Press. 9, 13, 37, 61, 63, 113

Pachos, J.K. & Papić, Z. (2018). Quantifying the effect of interactions in quantum many-body systems. 30, 32, 43

Pachos, J.K., Wieczorek, W., Schmid, C., Kiesel, N., Pohlner, R. & Weinfurter, H. (2009). Revealing anyonic features in a toric code quantum. *New J. Phys*, **11, 083010**. 3

Peschel, I. & Chung, M.C. (2011). On the relation between entanglement and subsystem hamiltonians. *EPL (Europhysics Letters)*, **96**, 50006. 27, 30

Peschel, I. & Eisler, V. (2009). Reduced density matrices and entanglement entropy in free lattice models. *Journal of Physics A: Mathematical and Theoretical*, **42**, 504003. 27, 30

Petrova, O., Mellado, P. & Tchernyshyov, O. (2013). Unpaired majorana modes in the gapped phase of kitaev's honeycomb model. *Phys. Rev. B*, **88**, 140405. 117

Petrova, O., Mellado, P. & Tchernyshyov, O. (2014). Unpaired majorana modes on dislocations and string defects in kitaev's honeycomb model. *Phys. Rev. B*, **90**, 134404. 117

Preskill, J. (2018). Quantum Computing in the nisq era and beyond. *Quantum*, **2**, 79. 1

Read, N. (2009). Non-abelian adiabatic statistics and hall viscosity in quantum hall states and $p_x + ip_y$ paired superfluids. *Phys. Rev. B*, **79**, 045308. 5

Read, N. & Green, D. (2000). Paired states of fermions in two dimensions with breaking of parity and time-reversal symmetries and the fractional quantum hall effect. *Phys. Rev. B*, **61**, 10267–10297. 2, 5

Reall, H.R. (2017). Lectures on general relativity. 61, 78

Resende, M.F.A.d. (2017). A pedagogical overview about the 2d and 3d toric codes and the origin of their topological orders. *arXiv:1712.01258 [quant-ph]*. 3, 14, 102

Savary, L. & Balents, L. (2017). Quantum spin liquids: a review. *Reports on Progress in Physics*, **80**, 016502. 76

Schmidt, K.P., Dusuel, S. & Vidal, J. (2008). Emergent fermions and anyons in the kitaev model. *Physical Review Letters*, **100**. 76

Schutz, B. (2009). *A First Course in General Relativity*. Cambridge University Press, 2nd edn. 61, 78, 85

Self, C.N., Pachos, J.K., Wootton, J.R. & Iblisdir, S. (2017). Conformal energy currents on the edge of a topological superconductor. *Phys. Rev. B*, **95**, 115141. 5

Self, C.N., Knolle, J., Iblisdir, S. & Pachos, J.K. (2019). Thermally induced metallic phase in a gapped quantum spin liquid: Monte carlo study of the kitaev model with parity projection. *Phys. Rev. B*, **99**, 045142. 5

Semenoff, G.W. (1984). Condensed-matter simulation of a three-dimensional anomaly. *Phys. Rev. Lett.*, **53**, 2449–2452. 68

Tagliacozzo, L. & Vidal, G. (2011). Entanglement renormalization and gauge symmetry. *Phys.Rev.B83:115127*. 4

Terhal, B.M., Hassler, F. & DiVincenzo, D.P. (2012). From majorana fermions to topological order. *Phys. Rev. Lett. 108, 260504*. 3

Trebst, S., Troyer, M., Wang, Z. & Ludwig, A.W.W. (2008). A short introduction to fibonacci anyon models. *Progress of Theoretical Physics Supplement*, **176**, 384. 37

Tsui, D.C., Stormer, H.L. & Gossard, A.C. (1982). Two-dimensional magnetotransport in the extreme quantum limit. *Phys. Rev. Lett.*, **48**, 1559–1562. 2

Turner, C.J., Meichanetzidis, K., Papic, Z. & Pachos, J.K. (2017). Optimal free descriptions of many-body theories. *Nat. Commun.*, **8**, 14926. 3, 7, 28, 30, 32, 35, 41, 43

von Keyserlingk, C.W. & Burnell, F.J. (2015). Walker-wang models and axion electrodynamics. *Phys. Rev. B*, **91**, 045134. 38

von Keyserlingk, C.W., Burnell, F.J. & Simon, S.H. (2013). Three-dimensional topological lattice models with surface anyons. *Phys. Rev. B*, **87**, 045107. 38

Wagner, G., de Juan, F. & Nguyen, D.X. (2019). Quantum hall effect in curved space realized in strained graphene. 5, 118

Wald, R.M. (1984). *General relativity*. Chicago Univ. Press, Chicago, IL. 61, 78, 85

Walker, K. & Wang, Z. (2012). (3+1)-tqfts and topological insulators. *Frontiers of Physics*, **7**, 150–159. 3, 24, 26, 32, 38, 116

Wen, X.G. (1990). Topological orders in rigid states. *International Journal of Modern Physics B*, **04**, 239–271. 2

Wen, X.G. & Zee, A. (1992). Shift and spin vector: New topological quantum numbers for the hall fluids. *Phys. Rev. Lett.*, **69**, 953–956. 5

Wiegmann, P. (2018). Inner nonlinear waves and inelastic light scattering of fractional quantum hall states as evidence of the gravitational anomaly. *Phys. Rev. Lett.*, **120**, 086601. 5

Wilczek, F. (1982). Quantum mechanics of fractional-spin particles. *Phys. Rev. Lett.*, **49**, 957–959. 2

Willans, A.J., Chalker, J.T. & Moessner, R. (2011). Site dilution in the kitaev honeycomb model. *Phys. Rev. B*, **84**, 115146. 117

Wootton, J.R. (2017). Demonstrating non-abelian braiding of surface code defects in a five qubit experiment. *Quantum Science and Technology, Volume 2, Number 1*. 3

Wootton, J.R. & Pachos, J.K. (2011). Bringing order through disorder: Localisation of errors in topological quantum. *Phys. Rev. Lett. 107, 030503*. 3

Yang, Z.C., Iadecola, T., Chamon, C. & Mudry, C. (2019). Hierarchical majoranas in a programmable nanowire network. *Phys. Rev. B*, **99**, 155138. 91, 95, 96

Yao, H. & Qi, X.L. (2010). Entanglement entropy and entanglement spectrum of the kitaev model. *Phys. Rev. Lett.*, **105**, 080501. 42, 115

You, Y.Z., Qi, X.L. & Xu, C. (2016). Entanglement holographic mapping of many-body localized system by spectrum bifurcation renormalization group. *Phys. Rev. B 93, 104205*. 41, 46